

ULTRASONIC SIMULATION AND MEASUREMENTS WITH CUT-OFF FREQUENCY EXTRACTIONS

by

Kazeem Adeogun

A Thesis submitted to the Faculty of Graduate Studies of

The University of Manitoba

in partial fulfilment of the requirement for the degree of

Master of Science

Department of Mechanical and Manufacturing Engineering

University of Manitoba

Winnipeg

Copyright © 2012 by Kazeem Adeogun

Abstract

The removal of the effect of imperfect dynamic properties of ultrasonic transducers and associated electronics, as well as the couplant to a structure, from experimental data is presented. The investigation reveals that it is unnecessary for the instrumentation to have an ideal frequency response function for a transducer because imperfect measurement behaviour can be removed with post processing. A computer simulation of a homogeneous, isotropic pipe's radial displacement is shown to agree closely with a corresponding measurement if a reasonably accurate frequency response function of the measurement chain is incorporated.

A procedure to extract the cut-off frequencies of an unblemished pipe and the singularity frequencies of a notched pipe is developed. Frequency differences between the cut-off frequencies and the nearest frequencies of singularities introduced by a circumferential notch are investigated. It is confirmed experimentally that singularities are introduced by a notch and differences are measurable at a 95% confidence level.

Acknowledgements

This thesis is dedicated to my daughter, Masouda Adeogun. Her arrival inspired and encouraged me to take this challenging opportunity.

I wish to express my profound gratitude to my research advisors, Professors Neil Popplewell and Hao Bai (Lakehead University), for suggesting the research topic and providing invaluable expert guidance, constant encouragement during the research work and the accomplishment of this thesis. My deep appreciation goes to Professor Neil Popplewell and Darryl Stoyko for their readiness to help and their fruitful discussions. The contributions of Patrick Flemings, Peter Lacoursiere are graciously appreciated. I would also like to express my grateful thanks to Professor Ahmed Shalaby for serving on the advisory committee. A word of thanks is extended to my friends and Mr Hakeem Adeyemi (United States Navy) for their support and friendly help.

I am also indebted for the financial support from the Natural Science and Engineering Research Canada (NSERC) of Professors Neil Popplewell and Hao Bai, the Teaching assistantship from the Department of Mechanical Engineering is also appreciated.

Finally and grateful, I thank my parents, Mr and Mrs Adeogun, and my wife, Mrs Idowu Adeogun, for their special thoughtfulness, encouragement, understanding, and support throughout the difficulties of my graduate program.

Kazeem Adeogun
November, 2012

TABLE OF CONTENTS

	Page
Abstract	ii
Acknowledgements	iii
List of Tables	viii
List of Figures	x
List of Nomenclature	xiii
1 INTRODUCTION	1
1.1 Preamble	1
1.2 Background, scope and objectives of the thesis.....	2
1.3 Non-destructive testing (NDT)	4
1.3.1 Ultrasonic Testing.....	6
1.4 Literature Review.....	7
1.4.1 Wave propagation in cylinders	9
1.4.2 Wave scattering in cylinders	11
1.5 Overview of the thesis	12
1.6 Structure of thesis	13
2 WAVES IN INFINITE CYLINDERS	14
2.1 Overview of wave functions	14
2.2 Problem statement.....	15
2.3 Governing equations of motion	16
2.4 Governing equations based on Semi Analytical Finite Elements.....	17
2.4.1 Approximate governing equations.....	17
2.5 Solution procedure for steady-state loading	19
2.6 Green's displacement functions.....	20
2.7 Input force.....	25
2.7.1 Excitation	25
2.8 Mechanical properties of the cylinder.....	26
2.9 Dispersion curves and phase speed.....	27
2.10 Overview of computer simulation	30
2.11 Illustrative example.....	31
2.12 Data from experiments and comparison with a computer simulation	32
2.12.1 Preamble	32
2.12.2 Experimental set-up	32
2.13 Computer simulation and initial experimental comparison	36

3	SIGNAL PROCESSING OF ULTRASONIC MEASUREMENTS	39
3.1	Preamble	39
3.2	Ultrasonic transducer’s characterization.....	40
3.2.1	Experimental material and criteria.....	40
3.3	Frequency response of the instrumentation chain and transducer coupling ..	41
3.3.1	Experimental set-up and data processing.....	41
3.3.2	Preliminary experiment and results	42
3.4	Experiment with beeswax uncontrolled coupling.....	45
3.5	Experiment with beeswax controlled coupling.....	47
3.6	Data collection and analysis.....	49
3.7	Determining transducer’s Frequency Response Function	49
3.8	Simulating the output response of a transducer	50
3.9	Preliminary tests of computer software	52
3.10	Comparison of generic response time histories computed directly in time and indirectly from frequency domain.....	54
4	ELIMINATING THE EXTRANEOUS BEHAVIOUR OF A TYPICAL ULTRASONIC TRANSDUCER	57
4.1	Preamble	57
4.2	Overview of inverse procedure for steel pipe.....	58
4.3	Predicting the temporal response of an idealized cylinder by using SAFE	59
4.4	Including the measurement chain, $H_m(\omega)$, in idealized cylinder’s frequency response function, $H_c(\omega)$, to simulate the measured frequency response, $O_{cm}(\omega)$	60
4.5	Inverse procedure to remove the effect of output measurement chain, $H_m(\omega)$, from measured cylinder’s time response, $o_{cm}(t)$	62
4.6	Updating idealized cylinder’s response to incorporate the effect of measurement chain by including an exponential window to eliminate data leakage	64
4.7	Application of exponential window to alleviate leakage.....	64
4.8	Reconstructing time histories by applying an exponential temporal window.....	67
4.9	Autocorrelation of the predicted response from SAFE and its “cross correlation” with itself.	69
4.10	Cross correlation coefficient and time domain correspondence.....	69
4.10.1	Theoretical derivation of cross correlation coefficients.....	69
5	EXTRACTING CUT-OFF FREQUENCIES OF AN UNBLEMISHED PIPE’S RADIAL DISPLACEMENT HISTORY	74
5.1	Preamble	74
5.2	Method of choosing an appropriate cut-off frequency from a measured time history	75
5.2.1	Basic procedure for the extraction of cut-off frequencies by curve fitting.....	77

5.2.2	Residual and Etta max (η_{\max})	81
5.3.	Estimating cut-off frequencies by using a cross correlation approach	82
5.4	Discussion of results	89
6	EXPERIMENTAL DETECTION OF A NOTCH USING THE FREQUENCY OF A SINGULARITY	91
6.1	Preamble	91
6.2	Definition of non-dimensional parameters	92
6.3	Relationship between the frequency of singularity and cut-off frequency of an unblemished pipe	92
6.4	Investigating frequency differences for open, rectangular notches having various circumferential extent.....	94
6.4.1	First stage test (Phase I).....	94
6.4.2	Second stage test (Phase II)	99
6.5	Statistical analysis of estimated frequency differences	105
6.5.1	Illustrative example.....	106
6.5.1.1	Case A: Frequencies of the singularities for the free end of pipe	106
6.5.1.2	Case B: Frequencies of singularities after introducing a notch with an 80% circumferential extent	108
6.6	Discussion of results and statistical justification	111
7	CONCLUSIONS AND RECOMMENDATIONS	112
7.1	Conclusions.....	112
7.2	Recommendations.....	114
	References	115
	Appendices	122
	Appendix A Approximate equation of motion using SAFE	122
	Appendix B Error Analysis.....	127
	Appendix C Time history and corresponding spectral density for higher flexural modes	129
	Appendix D MATLAB M-FILE for plotting frequency response function of the instrumentation chain using beeswax for repeatability.....	130
	Appendix E MATLAB M-FILE for plotting the histogram for the cut-off frequencies	133
	Appendix F MATLAB M-FILE for eliminating the extraneous behaviours of transducer chain	136

Appendix G MATLAB M-FILE for extracting the cut-off frequency using curve fit procedure.....	141
Appendix H Flow chart diagram illustrating the inverse procedure.....	143

List of Tables

Table 2.1.	Properties assigned to the unblemished pipe [3]	27
Table 3.1.	Ambient air conditions for the measured frequency response functions of instrumentation chain	42
Table 4.1.	Effect of damping on the exponential window.	66
Table 4.2.	Comparison of cut-off frequencies of predicted response from SAFE and those obtained from the inverse procedure	72
Table 5.1.	Comparisons of the cut-off frequencies produced by curve fitting, simulated annealing and a pattern search	77
Table 5.2.	Showing the selected cut-off frequencies with corresponding values of the cross correlation coefficient, r_{xy} , and Etta max, η_{\max}	85
Table 5.3	Convictional and ultrasonic measurements with their and averaged values for an actual steel pipe.....	86
Table 5.4.	F(10,1) through F(12,1) cut-off frequencies obtained from a time history involving a single mode	87
Table 5.5	Cut-off frequencies obtained from a time history which simultaneously involved several modes	87
Table 5.6	Cut-off frequency and uncertainties calculated from experimental data ..	89
Table 6.1.	Showing differences along the pipe of predominant frequencies	94
Table 6.2.	Measured dimensions of the second steel pipe	100
Table 6.3.	Showing frequency difference, Δf , for open notches having different percentage circumferential extents	101
Table 6.4(a)	Measured frequency difference, Δf , shifts for different, higher order flexural modes measured at the free end of the steel pipe.....	104
Table 6.4(b)	The Δf , for the higher order flexural modes F(10,1), F(11,1) and F(12,1) measured for a notch having an 80% circumferential extent.....	104
Table 6.5(a)	Uncertainty analysis of frequency differences, Δf , for free end reflection relative to F(10,1), F(11,1) and F(12,1) cut-off frequencies	109

Table 6.5(b) Uncertainty analysis of frequency differences, Δf , for 80% circumferential notch relative to F(10,1), F(11,1) and F(12,1) cut-off frequencies.....	110
---	-----

List of Figures

Figure 1.1.	Schematic of a typical Ultrasonic Testing apparatus [9].....	7
Figure 2.1.	Schematic representation of pipe and general transducer locations [9]	16
Figure 2.2.	Gaussian modulated sine function in (a) time (b) its spectral density [9]..	26
Figure 2.3.	Group velocity dispersion curves for a 3 in diameter, steel pipe [18,19] ..	29
Figure 2.4.	(a) Schematic [3] and (b) photograph of the experimental set-up.....	34
Figure 2.5.	Agilent Technologies 33210 arbitrary waveform generator	35
Figure 2.6.	Agilent Technologies function arbitrary waveform generator DS06014A digital storage oscilloscope	35
Figure 2.7.	DWCPA2040GA preamplifier	35
Figure 2.8.	Showing transmitting (red band) and receiving (blue band) (DWC B225 ultrasonic transducers) location.....	35
Figure 2.9.	Complete experimental set-up and data acquisition unit	36
Figure 2.10.	Giving (a) the computed time history of the radial displacement on the pipe's outer surface at $\theta = 0$, $z^* = z/H = 5.1$ and (b) the corresponding spectral density with a 500Hz frequency resolution	37
Figure 2.11.	Giving (a) the experimental time history of the radial displacement on the pipe's outer surface at $\theta = 0$, $z^* = z/H = 5.1$ with end reflection time gating out and (b) the corresponding spectral density having a frequency resolution of 500 Hz	38
Figure 3.1.	Experimental set up for the Frequency Response Function of transducer and associated couplant.	42
Figure 3.2.	Comparison of receiving chains (a) frequency response function and (b) corresponding phase using different couplants.....	44
Figure 3.3.	Comparison of (a) amplitude and (b) phase of nominally identical frequency response functions of receiving transducer chain with an uncontrolled beeswax coupling.....	46
Figure 3.4.	Comparison of better controlled experimental frequency response functions of receiving transducer chain showing (a) amplitude (b) phase.	48

Figure 3.5.	Relative frequency response of transducer chain in (a) amplitude and (b) phase.....	50
Figure 3.6.	Block diagram illustrating the procedure to predict the response given in Figure 3.7.....	51
Figure 3.7.	Time history of transducer's measured and predicted response.....	52
Figure 3.8.	Figure 3.8. Block diagram pertinent to Figure 3.9	53
Figure 3.9.	Comparison of Gaussian input with the convolution of inverse FRF of measurement chain.....	54
Figure 3.10.	Block diagram illustrating a generic convolution in time	55
Figure 3.11.	Convolution of the product of the Gaussian input (in time) and the system's impulse response function.....	55
Figure 3.12.	Comparison of generic response time histories computed directly in time and indirectly from frequency domain.....	56
Figure 4.1.	Block diagram illustrating prediction of temporal response of idealized cylinder without measurement chain.....	59
Figure 4.2.	Idealized time history (a) predicted at $\theta = 0$, and $z = 5.1H$ without the effect of measurement chain and (b) the corresponding spectral density ..	60
Figure 4.3.	Block diagram illustrating the procedure to incorporate the measurements chain's effect	61
Figure 4.4.	Showing (a) simulated time history predicted at $\theta=0^0$ and $z = 5.1H$, and (b) corresponding experimental history which incorporates the effect of measurement chain.....	62
Figure 4.5.	Block diagram illustrating the way of ameliorating the effect of the measurement chain	62
Figure 4.6.	Showing (a) the idealized time history predicted at $\theta=0^0$ and axial offset, $z = 5.1H$ and (b) corresponding history after eliminating the effect of imperfect measurement chain.....	63
Figure 4.7.	Exponential window applied at various effective dampings to the input signal and output response	66
Figure 4.8.	Block diagram illustrating the application of inverse function on the convoluted DFT and exponential window	67

Figure 4.9.	Showing (a) idealized time history predicted at $\theta=0^0$ and axial offset, $z = 5.1H$, and (b) corresponding history recovered with an exponential window having 15% damping	68
Figure 4.10.	Auto-correlation of prediction at circumferential offset, $\theta = 0$ and axial offset, $z = 5.1H$	71
Figure 4.11.	Relationship between the autocorrelation of the prediction and “cross correlation” with the predicted response involving 15% damping	71
Figure 4.12.	Histogram showing the percentage difference of various percentage dampings for the $F(10,1)$, $F(11,1)$ and $F(12,1)$ for cut-off frequencies	73
Figure 5.1.	Experimental time history showing end reflection just after 1000 μs	80
Figure 5.2.	History after timing gating out the end reflection from the above experimental data	80
Figure 5.3.	Magnitude of the reassigned pseudo Margenau-Hill time frequency distribution for the predicted radial displacement history given in Figure 5.2 [74]	82
Figure 5.4.	Time history predicted at $\theta = 0$, and $z = 5.1H$ before the curve fitting procedure.....	84
Figure 5.5.	Showing time histories at and $\theta = 0$ and $z = 5.1H$, from predicted (black legend) and curve fitting (red legend) having cross correlation of 0.998..	84
Figure 6.1.	Spectral density showing the frequency of a singularity introduced by a notch and cut-off frequency of the unblemished pipe [3].....	93
Figure 6.2.	Measurement at $z = 5.1H$ and $\theta = 0$ of the reflection coefficient from an unblemished pipe’s free end.	96
Figure 6.3.	(a) Radial displacement time history of unblemished pipe and (b) corresponding spectral density at $z = 5.1H$ and $\theta = 0$	97
Figure 6.4.	(a) Radial displacement’s time history measured near the free end and (b) the corresponding spectral density at $z = 5.1H$ and $\theta = 0$	98
Figure 6.5.	Open notch having an 80% circumferential extent at an axial separation of 5.1H between the two transducers.....	100
Figure 6.6.	(a) Radial displacement history for the 80% circumferential notch and (b) the corresponding spectral density.....	102

List of Nomenclature

Roman letters

A	Amplitude, volts (V)
a	A constant controlling the decay rate in the input, Gaussian modulated sine wave, s ⁻²
\bar{f}_c	Mean cut-off frequency of a particular mode, kHz
f_c	Cut-off frequency of a particular mode, kHz
\bar{f}_s	Mean frequency of singularity, kHz
f_s	Frequency of singularity, kHz
H	Constant thickness of cylinder, in (mm)
$H_m(\omega)$	Frequency response function of receiving transducer, amplifier and beeswax coupling
$H_c(\omega)$	Frequency response function of an idealized cylinder
$h(t)$	Impulse response of the measurement chain alone
I	Total number of data points assumed for the “free vibration” portion of a time history
$I(\omega), i(t)$	Gaussian modulated sine wave in frequency and time, respectively
l	Axial length, of a defect, in (m)
n	Circumferential wavenumber
$O(\omega), o(t)$	Output response in frequency and time domain, respectively
$O_c(\omega), o_c(t)$	Output response of the idealized cylinder in frequency and time domain, respectively

$O_{cm}(\omega)$, $o_{cm}(t)$ Idealized cylinder's response in frequency and time domains, respectively,
that incorporates the effect of measurement chain

$\bar{p}(\omega)$ Fourier transform of the function describing the temporal variation of the
input force

R_m Pipe's mean radius, in (m)

R^2 Coefficient of determination

s Time scaling factor appearing in the input Gaussian modulated sine wave

T Time duration of a record, s

t Time instant, s

w Axial displacement, in (m)

z Indicates an axial coordinate, in (m)

θ Phase angle, degrees

$w(t)$, $w(T)$ Value of exponential window at end of a time record

ω Circular frequency, rad/s

CF Curve Fitting

COF_c A cut-off frequency (COF) of the idealized cylinder, kHz

COF_{cm} A cut-off frequency which incorporates the simulated effect of
measurement chain, kHz

DFT Discrete Fourier Transform

FRF Frequency Response Function

IDFT Inverse Discrete Fourier Transform

IFT Inverse Fourier Transform

NDT Non-Destructive Testing

r_{xy}	Cross correlation
SA	Simulated Annealing
SAFE	Semi-Analytical Finite Element
TFRs	Time Frequency Representations

Greek Letters

δ	Dirac delta function
ζ, η	Dimensionless radial and axial coordinate in the local, isoparametric element's coordinate system, respectively
λ	First Lamé constant, psi (Pa)
μ	Second Lamé constant, psi (Pa)
ν	Poisson's ratio
ν	Degrees of freedom
ρ	Mass density, slug/in ³ (kg m ⁻³)
ξ	A viscous like damping coefficient
τ	Shear stress in which a subscript indicates the direction, psi (Pa)
τ	Time shifting factor in the input, Gaussian modulated sine wave, s
τ	Instant at which the “free vibration” portion of a time history is assumed to begin, s
τ	Time shift of one signal with respect to another signal, s
σ	Normal stress in which a subscript indicates the direction, psi (Pa)
σ_c	Standard deviation of cut-off frequency of a particular mode, kHz
σ_s	Standard deviation of frequency of singularity, kHz

τ, σ_0 Time constant, *s*, and decay rate, *rad/s*, of an exponential time window, respectively

Δ Indicates a change or difference in the quantity that follows

Δf_r Frequency resolution, Hz

Δf Frequency difference, Hz

Subscripts:

c, m Denotes a term referring separately to an idealized cylinder and experimental measurement chain, respectively.

cm Denotes a term referring to an idealized cylinder and a computer simulated experimental measurement chain for a receiving transducer

CHAPTER 1

INTRODUCTION

1.1 Preamble

The use of Non-Destructive Testing (NDT) techniques such as ultrasonic testing has proved to be effective in detecting defects such as cracks, delamination, voids, honeycombing, and debonding [1]. The concept of monitoring a modal cut-off frequency is examined as a means of detecting a crack [2]. A cut-off frequency of an unblemished pipe is the frequency below which a particular guided wave mode does not propagate. A previous computer simulation has shown that an open, axisymmetric notch's dimensions cannot be determined uniquely by using the reflection coefficient of solely one mode [3]. Experimental data performed are comparable to those from computer simulations which assumed invariably that all the material and geometrical parameters are known with certainty. It is unnecessary however, for the measurement instrumentation to have the ideal, flat frequency response function assumed computationally because the imperfect behaviour can be removed with the post processing of experimental data. Of particular interest in this thesis, is to further determine experimentally (by considering several higher order flexural modes e.g., F(10,1), F(11,1) and F(12,1),) the behaviour of an unblemished pipe's dominant response features near its cut-off frequencies after an open circumferential notch has been introduced artificially. These particular modes were chosen because flexural modes in waves reflected from a notch have shown to be readily detectable [3]. The procedure is introduced to obtain accurate cut-off frequencies and singularity frequencies introduced by a notch to locally assess a notch's dimensions. Such a singularity appears at a slightly different frequency to that of a nearby cut-off

frequency. However an accurate determination of the frequency difference is needed. A general perspective of this research is given briefly next.

1.2 Background, scope and objectives of the thesis

When an engineering structure like a geometrically bounded pipe of interest resembles a wave guide, ultrasonic guided waves can be generated by wave reflections from boundaries. Much research has been carried out in the use of guided waves for various NDE applications [4-6]. Such waves are important because they enable defects to be detected remotely at a distances tens of metres [3]. However repeatable measurement are needed for credible interpretations. The Frequency Response Function (FRF) of the instrumentation chain and associated couplant between transducer and pipe is a straightforward way of assessing this consistency. It was found that it is unnecessary for the FRF of the instrumentation chain to be ideal, as assumed generally in computer models, because measurement deficiencies can be overcome with further post processing. However, even such processing is unnecessary with the use of only the frequencies at which predominant peaks occur in a FRF. A procedure was developed to extract accurate frequencies of singularities from the basic information of a NDT measured time history. It is achieved by using a cross-correlation procedure. As an alternative to a tediously found reflection coefficient [3], the use of the frequency difference between the nearest cut-off frequency of an unblemished pipe and the frequency of a singularity has been proposed computationally to dimension a local notch [3]. Therefore, a reliable experimental procedure was developed that will efficiently extract the true frequencies of singularities from a measured time history. A challenge which may arise from the measurement of the time histories themselves is the “colouration” introduced by an

imperfect measurement chain. This situation may arise when comparisons are made between experimental and computer simulated data. However, if the usually imperfect measurement behaviour is repeatable, the imperfection may be removed with the post processing of a captured signal. This additional step is unnecessary, on the other hand, when extracting the clearly dominant singularity frequencies. A means of refining the frequency resolution of a DFT is needed because the history is not long enough for a DFT alone to obtain a sufficiently fine frequency resolution. Consequently a straightforward polynomial curve fit of a particular time history is employed whose initial amplitude, frequency and phase approximation emanate from a DFT. Refinements are made that improve the cross-correlation between the original and approximate time histories. Moreover the time window, which distinguishes the comparison's period, is adjusted to further improve the cross-correlation coefficient as well as the frequency estimates. Accurate singularity frequencies have been shown previously [3]. The importance of this well refined cut-off frequency is found to constitute a more straightforward basis of dimensioning a notch than reflection coefficients of singly generated modes.

The aim and objective of this thesis is to develop an ultrasonic, NDT procedure to reliably extract frequencies corresponding to the discontinuities in the spectral densities of radial displacement-measured, time histories of homogeneous¹ and isotropic² pipe.

¹ A material is said to be **homogeneous** if the material elastic properties (E, μ, λ) are the same at all points in the body.

² An **isotropic** material is the one having the same elastic properties (E, μ, λ) in all directions at any one point of the body.

The methodology to achieve this objective involves

- Characterize the dynamic behaviour of an ultrasonic transducer chain and investigate the effects of a commonly used couplants to attach a transducer to a pipe.
- Compare the computer simulation of cylinder with analogous experimental data.
- Develop a Non-Destructive Testing procedure and effectively remove artefacts introduced in duration limited experimental data with post processing.
- Develop a general procedure that will determine reliable, accurate cut-off and singularity frequencies.
- Conduct an experiment to show that a notch introduces singularity frequencies for higher order flexural modes that are distinct from the corresponding unblemished pipe's cut-off frequencies. The frequency difference demonstrates to be statistically different at a 95% confidence level.

1.3 NON-DESTRUCTIVE TESTING (NDT)

NDT is an interdisciplinary field dealing with the non-invasive inspection of components to check their structural integrity. It plays a critical role in assuring that structural components and systems perform in a reliable and cost effective fashion. NDT methods aim to locate and characterize material conditions and flaws that might otherwise cause planes to crash, reactors to fail, trains to derail, pipelines to burst, and a variety of less visible, but equally troubling events. Such tests are performed in a manner that does not affect the future usefulness of the object or material [7]. In other words, NDT allows parts and materials to be inspected and measured without damaging them. As an inspection is permitted without interfering with a product's final use, NDT provides a pragmatic balance between quality control and cost-effectiveness. Generally speaking,

NDT applies to all kind of industrial inspections, including metallic and non-metallic structures. NDT methods are primarily used for detection, location and sizing of surface and internal defects (in welds, castings, forging, composite materials, concrete and many more). [7, 8]. Various NDT methods are applied for preventive maintenance (aircraft, bridge), for the inspection of raw materials, half-finished and finished products, for in-service-inspection and for plant life assessments. NDT is essential for the quality control of the facilities and products, and for fitness, for purpose assessment (so-called plant life assessment). NDT assesses the remaining operation life of plant components (processing lines, pipes, vessels) providing an accurate diagnosis that allows predicting extended life operation beyond design life [7, 8].

NDT life extension and life assessment services involves the following step:

- i. Equipment integrity analysis
- ii. Corrosion monitoring of structures and equipment
- iii. Corrosion damage evaluation
- iv. Fatigue and creep damage prediction
- v. Fitness-for-service evaluation

The long list of NDT methods and techniques includes: radiographic testing (RT), ultrasonic testing (UT), liquid penetrant testing (PT), magnetic particle testing (MT), eddy current testing (ET), visual testing VT as well as leak testing LT, acoustic emission AE, thermal and infrared testing, microwave testing, strain gauging, holography, acoustic microscopy, computer tomography, non-destructive analytical methods, non-destructive material characterization methods, for example.

The “major six” (or basic) NDT methods, which are largely used in routine services to

industry is:

- i. Visual inspection
- ii. Liquid penetrant testing
- iii. Magnetic particle testing
- iv. Electromagnetic or eddy current testing
- v. Radiography
- vi. Ultrasonic testing

The NDT methods and techniques are well established for metallic and concrete structures like high buildings, bridges, tunnels and flyers [7].

1.3.1 ULTRASONIC TESTING

Ultrasonic refers to oscillations having frequencies above those audible by humans. Frequencies between about 20 kHz and 100 kHz are used commonly for inspecting non-metallic materials. Furthermore, frequencies between about 0.5 MHz and 10 MHz are often used to inspect of metallic materials. Ultrasound oscillation travel in different materials at different velocities. An ultrasonic wave will continue to travel through a material at a given velocity and does not return unless it “hits” a reflector. A reflector is considered to be any boundary between two different materials, or a flaw. The ultrasound generator (transducer) emits waves and in the same position receives reflected sounds (if any). High frequency sound waves are introduced into a material and they are reflected back from surfaces or flaws. Reflected sound energy is displayed versus time, and inspector can visualize a cross section of the specimen showing the depth of features that reflect sound (Figure 1.1) [7, 8, 9].

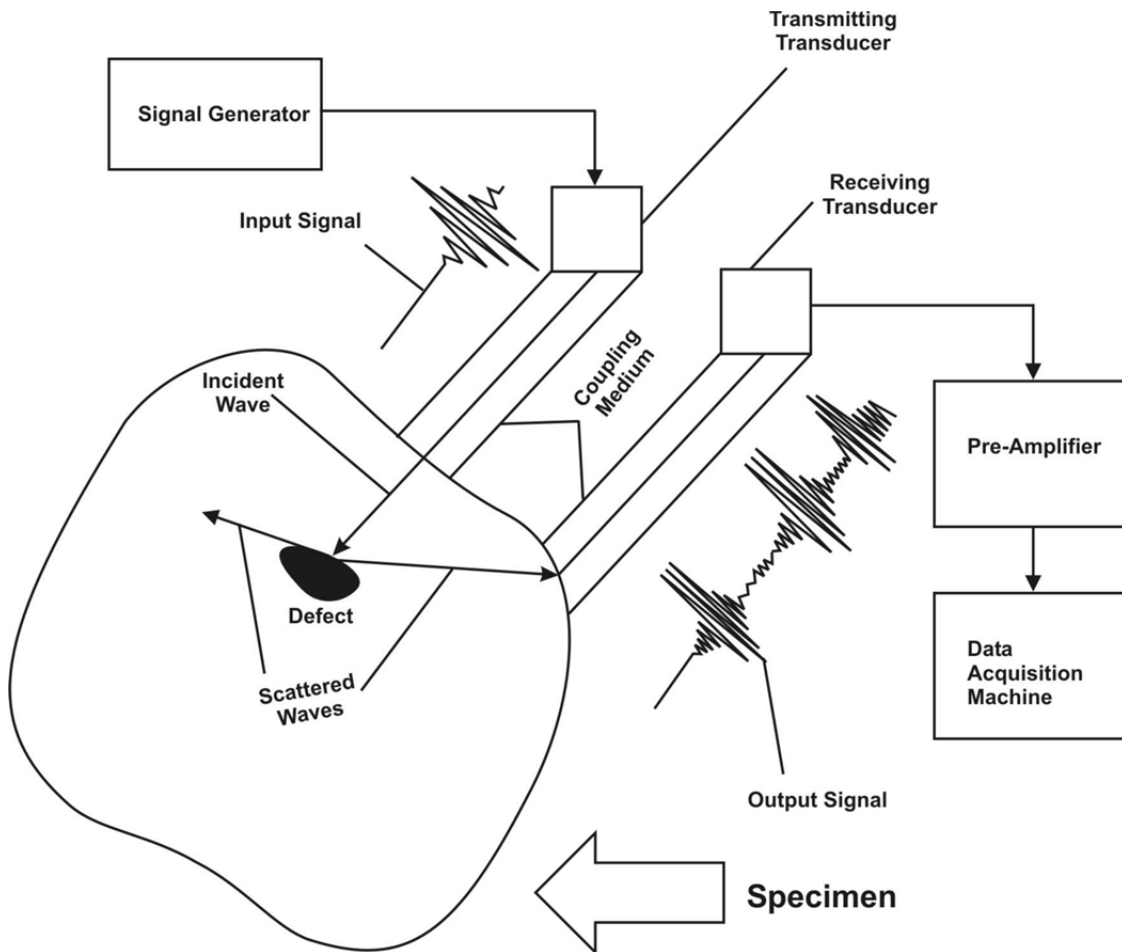


Figure 1.1. Schematic of a typical Ultrasonic Testing apparatus [9]

1.4 Literature Review

Guided waves are excited by a short burst of energy (the input signal) applied by a suitable transducer at one location on a structure. The excitation causes a packet of guided waves (the wave-packet) to propagate away from the transducer into the surrounding structure. Then either the same transducer or a second transducer is used to detect signals caused by reflections of the wave-packet from surrounding structural features or defects. The problems associated with the use guided waves for inspection purposes are well documented [10]. Multiple modes of guided wave propagation are possible in most structures and but these modes are generally dispersive (i.e. their

velocities are frequency-dependent). In order to obtain useful data from a guided wave inspection system, it is necessary to selectively excite and detect a single guided wave mode while suppressing coherent noise due to other modes of guided wave propagation. A viscous medium called a couplant is used to adhere transducers to a test specimen like a pipe in order, to permit a more efficient transmission of energy between the two. The consistency and reliability of a measurement is fundamental [11, 12]. The couplant is used to transmit the ultrasonic energy through the interface between the transducer and the material to be tested, but it has an effect on the amplitude of the signal [11, 13]. In other words, its purpose is to compensate for an imperfect contact between the transducer and test piece caused by curvature and/or surface roughness. Couplants are typically water, glycerine, or a variety of oil and water based gels. All liquid couplants have a much lower acoustical impedance than most structures. Of all the suitable liquids couplant, glycerine has the highest acoustical impedance and it is an excellent but expensive couplant. Grease and petroleum jelly can be used on vertical surfaces however they are also expensive and unpleasant to handle. The most commonly used liquid couplant is a medium-viscosity oil. On the other hand, the couplant to be used is appropriately selected according to the testing or environmental conditions. For example, water is in appropriate for the inspection of carbon steel which may corrode. Moreover viscous couplants may be required to inspect an inclined surface. However, all couplant layers reduce a transducer's sensitivity and broaden the width of the reflected pulses. In theory, if the couplant thickness is one-quarter the wavelength, multiple reflections in the couplant layer interfere, cancelling one another, and cause a loss of energy back to the piezoelectric crystal of a transducer when it is in a receiving mode [11, 12].

1.4.1 Wave propagation in cylinders

Theoretical studies of wave phenomena in cylinders can be categorized into two parts. The analysis of the dispersive wave propagation characteristics in an unblemished cylinders and the investigation of wave scattering by inhomogeneous or damaged cylinders. A comprehensive literature review given by Soldatos [14] contains many references to the general problems of dynamics of cylinders and cylindrical shells [14, 15].

Acoustical signals can be detected dozens of meters away from the generating location by applying vibrating the surface of pipes and elongated structures using ultrasonic transducers. This is possible because guided waves propagate with no outward spreading, unlike bulk waves. After the theoretical studies published [16, 17] considerable research has been performed for guided wave propagation within pipes. A number of intensive studies on guided-wave (NDE) Non-Destructive Evaluation were found [5, 18, 19] have been done following plate inspections with Lamb waves [10, 20]. However, in an ever-wider range of applications, such as the inspection of buried or meandering pipes (with or without defects and branches), various problems became apparent. Because wave propagation in a pipe is very complex, due to dispersion and its multimodal nature, various signal-processing techniques are required to quickly and correctly interpret the data. In many cases, defect resolution with guided waves is not sufficient to meet the practical demands of pipe inspection. To solve these problems, detected signals must be strictly verified against, first, with the prediction of guided wave theory. However, detected signals normally consist of a superposition of many modes having different velocity and dispersion characteristics [18, 19]. Moreover a guided wave in a pipe,

which has different displacement distributions not only in the axial and thickness directions, but also circumferentially, has more complex wave propagation behaviour than that of a Lamb wave in a plate [20]. When a wave travels along a semi-infinite cylinder and strikes its free end, an infinite number of reflected waves may be generated. These reflected waves may have real, imaginary, or complex wave numbers. The imaginary and complex modes carry no energy and their amplitudes decay exponentially with increasing distance. The non-propagating and evanescent modes, (i.e., the imaginary and complex modes, respectively), are as significant as the propagating modes at the edge of the cylinder as they are required to satisfy the traction free-end condition. Knowledge of the dispersion relation of guided waves in cylinders can be used to analyze the nature of wave phenomena in ultrasonic Non-Destructive Evaluation. There exists a substantial body of literature related to the dispersive wave propagation characteristics for waves travelling in an unblemished pipe. The pioneering studies of elastic vibration are those by Pochhammer [21] and Chree [22], they made a breakthrough towards solving the problem of vibration and waves in an infinitely long, homogeneous isotropic cylinder. The vibration and wave motion in the cylinder are governed by a dispersion equation which involves Bessel functions. This governing equation satisfies both wave equations (in cylindrical coordinates) throughout the cylinder and the traction free, boundary conditions on its lateral surfaces. Due to the complexity of this dispersion equation, complete numerical results over a wide range of frequencies with complex wavenumbers were not reported until 1960's by Once et al. [23]. These complex wave-numbers correspond to non-propagating and evanescent modes. Wave propagation in infinitely long homogeneous isotropic hollow cylinders was studied by Gazis [16, 17], Amenàkas

et al. [24-26] etc. Many researchers successfully investigated the dispersion characteristics of harmonic waves in infinite laminated isotropic rods [27 - 38]. A semi-analytical finite element (SAFE) method for wave propagation in laminated composite cylinders was developed later by Nelson et al. [39] and Huang and Dong [40]. In these pioneering studies, a finite element method is employed to solve wave propagation problems in cylinders.

1.4.2 Wave scattering in cylinders

Wave scattering occurs when travelling waves impinge on an inhomogeneity or a geometrical discontinuity in a cylinder. The free edge of a cylinder may be considered as a through-thickness crack. Oliver [41] and McNiven [42] first investigated experimentally the free end reflection of an axisymmetric wave in an elastic rod. McNiven and Shah [43] investigated the influence of the end mode on the resonant frequencies of elastic hollow cylinders. They found that hollow cylinders have a lower frequency for the end resonance than solid cylinders. Zemanck's result for the end resonant frequency, obtained by using a 9 - mode approximation, is very close to that obtained by Oliver for different Poisson's ratios [44]. There have been several other methods of solving this problem. The reflection of waves at the free edge of a laminated, anisotropic cylinder, for example, was studied by Song [45], Kim [46], Gregory and Gladwell [47], and Rattanawangcharoen et al. [48]. Laminated cylinders however are beyond the present scope.

1.5 Overview of the Thesis

Transmitting, receiving transducers and their ancillary electronic equipment are characterized in order to obtain the frequency responses. This procedure is important for ensuring that measurements are repeatable. Experimental results show that the frequency response of the available ultrasonic transducer is not a horizontal line. This transducer behaviour needs to be compensated. Therefore, a procedure was developed to take out the effect of instrumentation chain from the experiment. Furthermore, it became clear that the impression that all the experimental data were periodic was erroneous. This observation was confirmed from the non-periodicity and non-causality of the radial displacement history. Consequently efforts, which are described later, were made to correct these discrepancies. Subsequently, cut-off frequencies of an unblemished pipe were extracted from the resulting time-histories. Curve fitting remained to be the best candidate to refine these cut-off frequencies in comparison to global optimisation search techniques like pattern search and simulated annealing. A time window was selected that produced a cross correlation coefficient of 0.995 to 0.999 between a SAFE predicted displacement history and its cut-off frequencies were determined that were closest to the exact value as predicted by Semi Analytical Finite Element (SAFE) method. It was shown further through experimentations that singularities were truly introduced by a notch. The difference between the frequency of this singularity and the closest cut-off frequency of the unblemished pipe has been found to be a promising alternative to a more tediously found reflection coefficient [3]. A preliminary investigation of the correspondence between the experimental frequency differences produced by three modes and the

corresponding singularity frequency shows that the data is repeatable within the error bounds.

1.6 Structure of Thesis

This thesis is devoted to data post processing, increasing the reliability and accuracy of ultrasonic measurement procedures to extract cut-off and singularity frequencies and confirm, experimentally, that singularity are introduced by a notch. The difference between a singularity frequency and its nearest cut off frequency of an unblemished pipe has been used to dimension a notch [3]. However, an error analysis is needed still to assess the accuracy and consistency of frequency estimates.

An introduction, background, literature review and overview of this dissertation have been presented in Chapter 1. The wave equations, the steady-state elastodynamic axisymmetric Green's functions and the forward problem are presented in Chapter 2 for homogeneous, isotropic cylinder. Chapter 3 illustrates the procedure to characterize a typical commercial transducer and determine the repeatability of its associated instrumentation chain. Chapter 4 provides a procedure to ameliorate the imperfect behaviour of this instrumentation chain. The extraction of the cut-off frequencies of an unblemished pipe by using a cross-correlation procedure is presented in Chapter 5. The existence of singularities introduced by a notch is confirmed in Chapter 6. Conclusions are drawn and recommendations for future work are made in Chapter 7.

CHAPTER 2

WAVES IN INFINITE CYLINDERS

2.1 Overview of wave function

The detail of the SAFE formulation used in this thesis was developed by Zhuang [15] and modified by Darryl [9]. The SAFE formulation is used in the Green's functions derivation. With this formulation strategy, the radial dependence of a pipe's displacement is modelled by using one-dimensional, quadratic finite elements to circumvent the complexities of an arbitrary laminate profile. The corresponding axial and circumferential dependencies are treated analytically. Fourier integral transform pairs are applied to obtain governing equations in the wavenumber domain. The dispersion relation of the cylinders is formulated as a standard eigensystem. The bi-orthogonality properties of the associated left and right eigenvectors are employed to form the Green's functions by using a modal summation. For a given circumferential wavenumber, the solution of the resulting, three parameter, quadratic eigenvalue problem provides the dispersion relation for the cylinder. The response of the cylinder to a harmonic load can be described, for a given circumferential wavenumber, by a modal summation over the axial modes. A similar summation over the circumferential wavenumbers gives the steady state Green's functions. Then the (output) time response to a transient (input) point load is determined by treating each Green's function as a frequency response function and convolving it with the transient point load. An inverse Fourier transform applied to the convolved FRF gives the time response at a spatial point of interest [9, 15].

2.2 Problem Statement

An infinitely long pipe with mean radius R and thickness H is considered by adopting cylindrical coordinates (r, θ, z) with the origin fixed at the centre of a generic cross-section of the cylinder. A time variation is denoted by t . (An infinite pipe is reconciled with a practical pipe having a finite length by time gating out the latter's end reflections by using an appropriate time window) The mechanical variables of the problem are the displacement u , stress σ and strain ε [9, 15]. The cylinder is subjected to a point radial load, F . The inner and outer surfaces of the cylinder are assumed to be traction free. The right hand, cylindrical coordinate system (r, θ, z) shown in Figure 2.1. It is superimposed over a right hand, Cartesian coordinate system having typical coordinates (x, y, z) . The common origin of the two coordinate systems is located at the geometric centre of a generic cross-section of the cylinder with the z axis pointing along the longitudinal (axial) axis of the cylinder. The radial point load is applied at $y = 0$ in the plane $z = 0$. In the cylindrical coordinate system, $z = 0$ corresponds to the point of application of the point load. The cylinder is divided into N layers through the thickness as shown in Figure 2.1. Each layer corresponds to a quadratic, one dimensional finite element in the cylinder's radial direction. The thickness of, say, the k -th layer is H_k and it extends radially from r_k to r_{k+1} , as shown in Figure 2.1. [9].

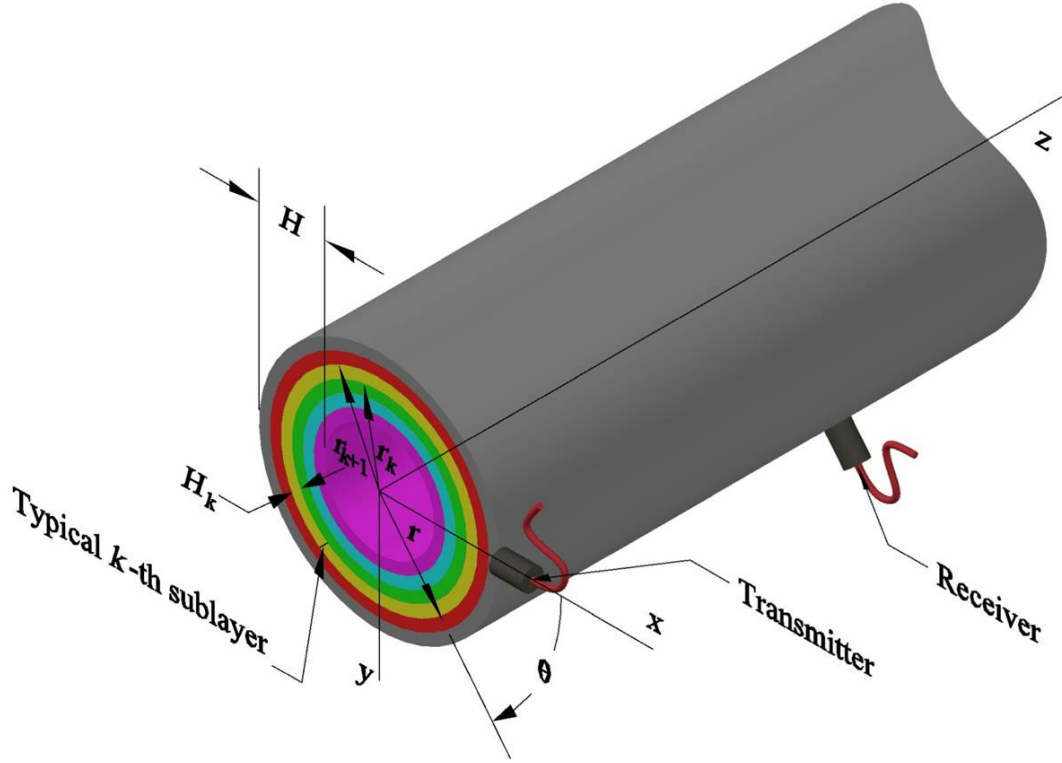


Figure 2.1. Schematic representation of pipe and general transducer locations [9].

2.3 Governing equations of motion

The wave fields of interest are the displacement, u , engineering strain, ε , and stress, σ . For a given layer in the cylindrical coordinate system shown in Figure 2.1, the time dependent quantities can be represented by the following column vectors:

$$\mathbf{u}(r, \theta, z, t) = [u, v, w] \quad (2.1)$$

$$\boldsymbol{\sigma}(r, \theta, z, t) = [\sigma_{rr}, \sigma_{\theta\theta}, \sigma_{zz}, \sigma_{\theta z}, \sigma_{rz}, \sigma_{r\theta}]^T \quad (2.2)$$

$$\boldsymbol{\varepsilon}(r, \theta, z, t) = [\varepsilon_{rr}, \varepsilon_{\theta\theta}, \varepsilon_{zz}, \gamma_{\theta z}, \gamma_{rz}, \gamma_{r\theta}]. \quad (2.3)$$

Time is represented by t , whereas u , v and w is the radial, circumferential and axial displacement component respectively. Moreover, $\varepsilon(\gamma)$ indicates an engineering normal (shear) strain, and σ indicates a stress. Subscripts r , θ , and z correspond to the radial,

circumferential, and axial directions, respectively. Superscript T indicates the transpose of a matrix.

The strain and displacement vectors are related by

$$\boldsymbol{\varepsilon} = (L_r + L_\theta + L_z)\mathbf{u} \quad (2.4)$$

The constitute relation for any layer in the laminated cylinder is

$$\boldsymbol{\sigma} = \mathbf{D}\boldsymbol{\varepsilon} \quad (2.5)$$

\mathbf{D} is a matrix of cylindrical orthotropic elastic moduli with the orthotropy axis coinciding with the z-axis (See Appendix A).

2.4 Governing equations based on Semi-Analytical Finite Elements

The Semi-analytical finite element (SAFE) method was developed by Nelson et al [39] and Huang and Dong [40] to study wave propagation problems. It is used to formulate the governing equations. The radial dependence of displacement \mathbf{u} , is treated in this approach by employing finite element modeling. Therefore, the thickness profile is therefore discretized into cylindrical lamina, and, within each lamina, quadratic interpolations over three equally spaced nodal surfaces characterize the kinematic behaviour.

2.4.1 Approximate governing equations

By using the SAFE method, each layer is discretized into several laminae. Let \mathbf{N} be the total number of the laminae through the pipe's thickness, H . Applying the finite element methodology to the discretized pipe allows the displacement field to be approximated by

$$\mathbf{u}(r, \theta, z, t) = \mathbf{N}(r)\mathbf{U}(\theta, z, t) \quad (2.6)$$

with $\mathbf{N}(r)$ as the assembled interpolations and $\mathbf{U}(\theta, z, t)$ as its corresponding system array of nodal degrees of freedom.

The governing displacement equations of motion are obtained by employing Hamilton's principle so that

$$\delta \int_{t_1}^{t_2} (T - V) dt = 0, \quad (2.7)$$

T and V are the kinetic and potential energies, respectively. They are given by

$$T = \frac{1}{2} \int_{vol} \rho \dot{\mathbf{u}}^T \dot{\mathbf{u}} dvol; \quad V = \frac{1}{2} \int_{vol} \boldsymbol{\varepsilon}^T \mathbf{D} \boldsymbol{\varepsilon} dvol + V_e. \quad (2.8)$$

Here ρ represents the mass density and V_e is the potential energy of external forces which is given by

$$V_e = -\mathbf{U}^T \mathbf{P}. \quad (2.9)$$

The \mathbf{P} represents the consistent load vector whose specific form involves the product of the applied surface traction and their corresponding interpolations. Substituting $\dot{\mathbf{u}}$ by differentiating equation (2.6) into T as well as $\boldsymbol{\varepsilon}$ of equation (2.4) into V leads to the discrete governing equations of motion.

$$\mathbf{K}_1 \mathbf{U} + \mathbf{K}_2 \mathbf{U}_{,0} + \mathbf{K}_3 \mathbf{U}_{,z} - \mathbf{K}_4 \mathbf{U}_{,00} - \mathbf{K}_5 \mathbf{U}_{,0z} - \mathbf{K}_6 \mathbf{U}_{,zz} + \mathbf{M} \ddot{\mathbf{U}} = \mathbf{F}. \quad (2.10)$$

The stiffness matrices, \mathbf{K}_i , $i=1, 2, \dots, 6$, mass \mathbf{M} and consistent load vector \mathbf{F} are defined by

$$\mathbf{M} = 2\pi \int \rho \mathbf{N}^T \mathbf{N} r dr. \quad (2.11)$$

$$\mathbf{F} = 2\pi \int \mathbf{N}^T \mathbf{P} r dr. \quad (2.12)$$

The algebraic structures of the stiffness matrices \mathbf{K}_i 's are given in Appendices A.18, A.19 and A.20. Note that \mathbf{K}_1 , \mathbf{K}_4 , \mathbf{K}_5 , and \mathbf{K}_6 are symmetric while \mathbf{K}_2 and \mathbf{K}_3 are antisymmetric.

2.5 Solution procedure for steady-state loading

The governing equation (2.10) is considered next for a time harmonic applied Force \mathbf{F} having (circular) frequency ω . The resulting steady-state displacement, \mathbf{U} , must be periodic with the same frequency ω . Let the θ -dependence of the loads and response be expressed $\bar{\mathbf{U}}_n$ by Fourier series. Hence, \mathbf{F} and \mathbf{U} can be written as:

$$\mathbf{F}(\theta, z, t) = e^{i\omega t} \mathbf{F}(\theta, z) = e^{i\omega t} \sum_{n=-\infty}^{n=+\infty} e^{in\theta} \bar{\mathbf{F}}_n(z) \quad (2.13)$$

and

$$\mathbf{U}(\theta, z, t) = e^{i\omega t} \sum_{n=-\infty}^{n=+\infty} e^{in\theta} \bar{\mathbf{U}}_n(z). \quad (2.14)$$

Substituting equation (2.14) into equation (2.10) yields a system of ordinary differential equations in z , for the Fourier coefficient functions $\bar{\mathbf{U}}_n$, The n th term of has the form

$$(\mathbf{K}_1 + in\mathbf{K}_2 + n^2\mathbf{K}_4 - \omega^2\mathbf{M})\bar{\mathbf{U}}_n + ik_n(\mathbf{K}_3 - in\mathbf{K}_5)\bar{\mathbf{U}}_{n,z} - \mathbf{K}_6\bar{\mathbf{U}}_{n,zz} = \bar{\mathbf{F}}_n. \quad (2.15)$$

The z -dependence is treated by means of a Fourier integral transform. The transform pair is defined in terms of the transform parameter, k_n , as

$$f(k_n) = \int_{-\infty}^{\infty} \bar{f}(z) e^{-ik_n z} dz; \quad \bar{f}(z) = \frac{1}{2\pi} \int_{-\infty}^{\infty} e^{ik_n z} dk_n. \quad (2.16)$$

Applying the Fourier transform to equation (2.16) gives

$$(\mathbf{K}_1 + in\mathbf{K}_2 + n^2\mathbf{K}_4 - \omega^2\mathbf{M})\mathbf{U}_n + ik_n(\mathbf{K}_3 - in\mathbf{K}_5)\mathbf{U}_{n,z} - \mathbf{K}_6\mathbf{U}_{n,zz} = \mathbf{F}_n. \quad (2.17)$$

Equation (2.17) is the governing equation for the displacement's n th circumferential harmonic in the transform domain. The first step of solving Equation (2.17) involves the consideration of the homogeneous equation. It has the form of a three-parameter algebraic eigensystem, in which either ω , n or k_n can be called upon to be the eigenvalue parameter. Here, k_n is adopted as the eigenvalue parameter and specific values are

assigned to ω and n . The quadratic eigen problem (2.17) for k_n can be recast into the first order form as [15, 9, 49].

$$[\mathbf{A}(n, \omega) - k_n \mathbf{B}(n)] \mathbf{Q}_n = \mathbf{P}_n \quad (2.18)$$

$$\mathbf{A}(n, \omega) = \begin{bmatrix} \mathbf{0} & (\mathbf{K}_1 + in\mathbf{K}_2 + n^2\mathbf{K}_4 - \omega^2\mathbf{M}) \\ (\mathbf{K}_1 + in\mathbf{K}_2 + n^2\mathbf{K}_4 - \omega^2\mathbf{M}) & i(\mathbf{K}_3 - in\mathbf{K}_5) \end{bmatrix} \quad (2.19)$$

$$\mathbf{B}(n) = \begin{bmatrix} (\mathbf{K}_1 + in\mathbf{K}_2 + n^2\mathbf{K}_4 - \omega^2\mathbf{M}) & \mathbf{0} \\ \mathbf{0} & -\mathbf{K}_6 \end{bmatrix} \quad (2.20)$$

and

$$\mathbf{Q}_n = \begin{bmatrix} \mathbf{U}_n \\ k_n \mathbf{U}_n \end{bmatrix}; \quad \mathbf{P}_n = \begin{bmatrix} \mathbf{0} \\ \mathbf{F}_n \end{bmatrix}. \quad (2.21)$$

By extracting the eigendata from the homogeneous form of equation (2.18) the displacement to the n th circumferential mode in the Fourier series representation of the applied force can be constructed by a modal summation.

2.6 Green's displacement functions

The eigendata serve as the basis for constructing a Green's function, details of which are presented in this section. The displacement field induced by a harmonic, point-like excitation is synthesized by linearly superimposing a pipe's normal modes. From the definition of the eigenvalue problem, the eigenvectors satisfy the relations [15]

$$[\mathbf{A}(n, \omega) - k_{nm} \mathbf{B}(n)] \phi_{nm}^R = 0, \quad (2.22)$$

$$[\mathbf{A}^T(n, \omega) - k_{nm} \mathbf{B}^T(n)] \phi_{nm}^L = 0, \quad (2.23)$$

$$\Phi_{nm}^{L^T} \mathbf{B} \Phi_{np}^R = \text{diag}(\mathbf{B}_{nm}), \quad (2.24)$$

and

$$\Phi_{nm}^{L^T} \mathbf{A} \Phi_{np}^R = \text{diag}(k_{nm} \mathbf{B}_{nm}). \quad (2.25)$$

The right and left eigenvectors are partitioned into the following upper and lower halves:

$$\boldsymbol{\phi}_{nm}^R = \begin{bmatrix} \boldsymbol{\phi}_{nm\mu}^R \\ \boldsymbol{\phi}_{nm\iota}^R \end{bmatrix} = \begin{bmatrix} \boldsymbol{\phi}_{nm\mu}^R \\ k_{nm} \boldsymbol{\phi}_{nm\mu}^R \end{bmatrix}, \quad (2.26)$$

$$\boldsymbol{\phi}_{nm}^L = \begin{bmatrix} \boldsymbol{\phi}_{nm\mu}^L \\ \boldsymbol{\phi}_{nm\iota}^L \end{bmatrix} = \begin{bmatrix} \boldsymbol{\phi}_{nm\mu}^L \\ k_{nm} \boldsymbol{\phi}_{nm\mu}^L \end{bmatrix} \quad (2.27)$$

and

$$\boldsymbol{\phi}_{np\mu}^{L^T} (\mathbf{K}_1 + in\mathbf{K}_2 + n^2\mathbf{K}_4 - \omega^2\mathbf{M}) \boldsymbol{\phi}_{nm\mu}^R - k_{np} k_{nm} \boldsymbol{\phi}_{nm\mu}^R = \delta_{pm} \mathbf{B}_{nm} \quad (2.28)$$

where δ_{pm} is the Kronecker delta.

$$(k_{nm} + k_{np}) \boldsymbol{\phi}_{np\mu}^{L^T} (\mathbf{K}_1 + in\mathbf{K}_2 + n^2\mathbf{K}_4 - \omega^2\mathbf{M}) \boldsymbol{\phi}_{nm\mu}^R + ik_{np} \mathbf{K}_{nm} \boldsymbol{\phi}_{np\mu}^{L^T} (\mathbf{K}_3 - in\mathbf{K}_5) \boldsymbol{\phi}_{nm\mu}^R = \delta_{pm} k_{nm} \mathbf{B}_{nm} \quad (2.29)$$

Subscripts u and l denote the upper and lower halves, respectively. Vector \mathbf{Q}_n can be represented, for a non-vanishing \mathbf{P}_n , in the transformed domain of the linear eigenvalue problem by summing the $12N+6$ right eigenvectors as

$$\mathbf{Q}_n = \sum_{m=1}^{12N+6} Q_{nm} \boldsymbol{\phi}_{nm}^R. \quad (2.30)$$

The coefficients, Q_{nm} , in the last equation can be found by substituting equation (2.30) into the linear eigenvalue problem, equation (2.18), and using the bi-orthogonality relations equations (2.26) and (2.27) to give [3, 9, 15]

$$Q_{nm} = \frac{\boldsymbol{\phi}_{mn}^{L^T} \mathbf{P}_n}{(k_{nm} - k_n)}. \quad (2.31)$$

Thus, the explicit form of \mathbf{Q}_n is given by

$$\mathbf{Q}_n = \sum_{m=1}^{12N+6} \frac{\boldsymbol{\phi}_{mn}^{L^T} \mathbf{P}_n}{(k_{nm} - k_n)} \boldsymbol{\phi}_{nm}^R. \quad (2.32)$$

The solution vector, \mathbf{U}_n , which occupies the upper half of \mathbf{Q}_n , is given by

$$\mathbf{U}_n = \sum_{m=1}^{12N+6} \frac{k_{nm} \phi_{mnu}^{L^T} \mathbf{F}_n}{(k_{nm} - k_n) \mathbf{B}_{nm}} \phi_{mnu}^R. \quad (2.33)$$

$$\mathbf{U}_n = \sum_{m=1}^{12N+6} \frac{\phi_{mnu}^{L^T} \mathbf{F}_n}{\left(1 - \frac{k_n}{k_{nm}}\right) \mathbf{B}_{nm}} \phi_{mnu}^R. \quad (2.34)$$

By using equations (2.18), (2.22), (2.23) (2.24), (2.2), finally, the inverse Fourier transform applied to equation (2.34) gives the displacement response of the cylinder to the n^{th} circumferential harmonic in the spatial domain, $\mathbf{U}_n(z)$, as [3, 9]

$$\bar{\mathbf{U}}_n(z) = \frac{1}{2\pi} \sum_{m=1}^{2N+6} \int_{-\infty}^{\infty} \frac{\phi_{mnu}^{L^T} \mathbf{F}_n}{\left(1 - k_n / k_{nm}\right) \mathbf{B}_{nm}} \phi_{mnu}^R e^{ik_n z} dk_n \quad (2.35)$$

In many problems, \mathbf{F}_n , ϕ_{mn}^L , ϕ_{mn}^R , and B_{nm} are independent of the wave number, k_n , so that the application of Cauchy residue theorem straight forwardly yields the modal response, $\bar{\mathbf{U}}_n(z)$. Moreover, the eigendata are divided equally into two groups according to whether a wave travels and decays along the $+z$ and $-z$ directions. Thus, the modal displacement, $\bar{\mathbf{U}}_n(z)$ can be expressed as two summations, each over a range of \mathbf{M} , for the opposite directions. Consequently [9].

$$\bar{\mathbf{U}}_n(z) = -i \sum_{m=1}^M \frac{k_{nm} \phi_{mnu}^{L^T} \mathbf{F}_n}{\mathbf{B}_{nm}} \phi_{mnu}^R e^{ik_{nm} z} - i \sum_{m=M+1}^M \frac{k_{nm} \phi_{mnu}^{L^T} \mathbf{F}_n}{\mathbf{B}_{nm}} \phi_{mnu}^R e^{ik_{nm} z}. \quad (2.36)$$

A radial point force which is applied at $r = r_0$, $\theta = 0$, $z = 0$ can be represented in the spatially as

$$\mathbf{F}(\theta, z) = \delta(\theta) \delta(z) \mathbf{F}_0 \quad (2.37)$$

where δ is the Dirac delta function and \mathbf{F}_0 describes the radial distribution of the force vector. (Subscript 0 denotes a quantity associated with the point load). The Dirac delta function is approximated circumferentially by a “narrow” pulse of uniform intensity $q_0 = (2r_0\theta_0)^{-1}$, which extending over a circumferential distance $2r_0\theta_0$. This approach is employed to avoid the non-convergence of the Dirac delta function [3, 9]. Then a force, which is applied at the point $r = r_0$, $\theta = 0$, $z = 0$, can be approximated spatially as

$$\mathbf{F}(\theta, z) = \begin{cases} \frac{1}{2\pi r_0} \delta(z) \mathbf{F}_0 & -\theta_0 \leq \theta \leq \theta_0 \\ 0 & \text{otherwise} \end{cases} \quad (2.38)$$

The representation of $\mathbf{F}(\theta, z)$ with the Fourier series expansion in the circumferential direction takes the form

$$\mathbf{F}(\theta, z) = \sum_{n=-\infty}^{n=+\infty} e^{in\theta} \frac{1}{2\pi r_0} \frac{\sin(n\theta_0)}{n\theta_0} \mathbf{F}_0 \delta(z) = \sum_{n=-\infty}^{n=+\infty} e^{in\theta} \mathbf{F}_n(z) \quad (2.39)$$

where

$$\bar{\mathbf{F}}_n(z) = \frac{1}{2\pi r_0} \frac{\sin(n\theta_0)}{n\theta_0} \mathbf{F}_0 \delta(z). \quad (2.40)$$

Further the Fourier transform of $\bar{\mathbf{F}}_n(z)$, $\mathbf{F}_n(z)$, is

$$\mathbf{F}_n(z) = \frac{1}{2\pi r_0} \frac{\sin(n\theta_0)}{n\theta_0} \mathbf{F}_0. \quad (2.41)$$

Substituting equation (2.41) into equation (2.36) gives

$$\bar{\mathbf{U}}_n(z) = \frac{1}{4\pi^2 r_0} \sum_{m=1}^{12+6} \int_{-\infty}^{\infty} \frac{\boldsymbol{\phi}_{mmu}^{L^T} \mathbf{F}_0}{(1 - k_n / k_{nm}) \mathbf{B}_{nm}} \frac{\sin(n\theta_0)}{n\theta_0} \times \boldsymbol{\phi}_{nm}^R e^{ik_n z} dk_n. \quad (2.42)$$

By applying the Cauchy residue theorem to equation (2.42) and considering motion only

In the +z direction yields the nth circumferential mode of the displacement Green's function as

$$\bar{\mathbf{U}}_n(z) = \begin{cases} -\frac{i}{2\pi r_0} \sum_{m=1}^{6N+3} \int_{-\infty}^{\infty} \frac{k_{nm} \boldsymbol{\phi}_{mnu}^{L^T} \mathbf{F}_0 \sin(n\theta_0)}{\mathbf{B}_{nm}} \times \boldsymbol{\phi}_{nm}^R e^{ik_{nm}z}, & z \geq 0, \\ \frac{i}{2\pi r_0} \sum_{m=6N+4}^{6N+3} \int_{-\infty}^{\infty} \frac{k_{nm} \boldsymbol{\phi}_{mnu}^{L^T} \mathbf{F}_0 \sin(n\theta_0)}{\mathbf{B}_{nm}} \times \boldsymbol{\phi}_{nm}^R e^{ik_{nm}z}, & z \leq 0. \end{cases} \quad (2.43)$$

The contour of integration, which is applied in conjunction with Cauchy's residue theorem, is selected by considering (i) waves radiate outward from the applied load, and (ii) the displacement field remains finite. Substituting equation (2.43) into equation (2.14) and using the result, in equation (2.6) gives the Green's displacement function for a harmonic load. The approximate strain and stress fields can be derived straightforwardly from this function by using equations. The displacement response to a multi-frequency, radial force can be found by merely superimposing the responses caused by each individual frequency component because linear elasticity is assumed. Hence the displacement at the radial coordinates of the finite element nodal surfaces can be written as [3, 9, 15].

$$\bar{\mathbf{U}}_n(\theta, z, t) = \frac{-i}{4\pi^2 r_0} \sum_{m=1}^{6N+3} \int_{-\infty}^{\infty} \bar{f}(\omega) e^{-i\omega t} \sum_{n=-\infty}^{n=\infty} \sin(n\theta_0) \left[\frac{\boldsymbol{\phi}_{mnu}^{L^T}(\omega) \mathbf{F}_0}{\mathbf{B}_{nm}(\omega)} \boldsymbol{\phi}_{nm}^R e^{ik_n(\omega)z} \right] e^{in\theta} d\omega \quad (2.44)$$

for $z \geq 0$, and

$$\bar{\mathbf{U}}_n(\theta, z, t) = \frac{-i}{4\pi^2 r_0} \sum_{m=6N+4}^{12N+6} \int_{-\infty}^{\infty} \bar{f}(\omega) e^{-i\omega t} \sum_{n=-\infty}^{n=\infty} \sin(n\theta_0) \left[\frac{\boldsymbol{\phi}_{mnu}^{L^T}(\omega) \mathbf{F}_0}{\mathbf{B}_{nm}(\omega)} \boldsymbol{\phi}_{nm}^R e^{ik_n(\omega)z} \right] e^{in\theta} d\omega \quad (2.45)$$

for $z \leq 0$.

The $\bar{f}(\omega)$ in the last two equations is the Fourier transform of the input force. It is employed to scale the amplitude and, also, phase shift the Green's function for each frequency component associated with the input force. The approximate displacement field throughout the entire pipe, u , can be found by invoking equation (2.6) [3].

2.7 Input force

2.7.1 Excitation

The excitation on the waveguide determines the relative amplitudes of the modes which are excited. It is subjected to a radial point load which is applied to the pipe's curved outer surface. The temporal variation of the loading pulse is a Gaussian modulated sine function wave given by [3, 9]

$$f(t) = \begin{cases} 0, & t < 0 \\ Ae^{(-a(st-\tau)^2)} \sin(s\omega_0 t), & t \geq 0 \end{cases} \quad (2.46)$$

whose Fourier transform is

$$f(\omega) = \begin{cases} \frac{-iA\sqrt{\pi}}{4s\sqrt{a}} \left[e^{\frac{(\omega+s\omega_0)(-\omega-s\omega_0+4i\tau as)}{4as^2}} - e^{\frac{(\omega-s\omega_0)(-\omega+s\omega_0+4i\tau as)}{4as^2}} \right. \\ \left. + \operatorname{erf} \left(\frac{i\omega + 2as\tau + is\omega_0}{2s\sqrt{a}} \right) e^{\frac{(\omega+s\omega_0)(-\omega-s\omega_0+4i\tau as)}{4as^2}} \right. \\ \left. - \operatorname{erf} \left(\frac{i\omega + 2as\tau + is\omega_0}{2s\sqrt{a}} \right) e^{\frac{(\omega-s\omega_0)(-\omega+s\omega_0+4i\tau as)}{4as^2}} \right] \end{cases} \quad (2.47)$$

The A , a , τ , and ω_0 are constants, t is time, in seconds, s is a time scaling factor used to set the ‘‘centre frequency,’’ and erf is the error function taking complex arguments. These constants are always taken to be: $A=1$ (Non-dimensional force), $a = 2.2959 \times 10^{10} \text{ s}^{-2}$, $\tau = 1.4 \times 10^{-5} \text{ s}$, and $\omega_0 = (5 \times 10^5) \pi \text{ rad/s}$, where the amplitude, A , has been non-dimensionalized by the cylinder's shear modulus (i.e., $A/\mu=1$). The scaling factor, s , is selected as 0.28 to give a centre frequency of 70 kHz. The resulting pulse is presented in Figure 2.2 (a) while its corresponding spectrum is shown in Figure 2.2 (b) [3, 9, 49]. It

will be seen to predominantly excite the $F(10,1)$, $F(11,1)$ and $F(12,1)$ ³ flexural modes of the 3 in diameter steel pipe considered next.

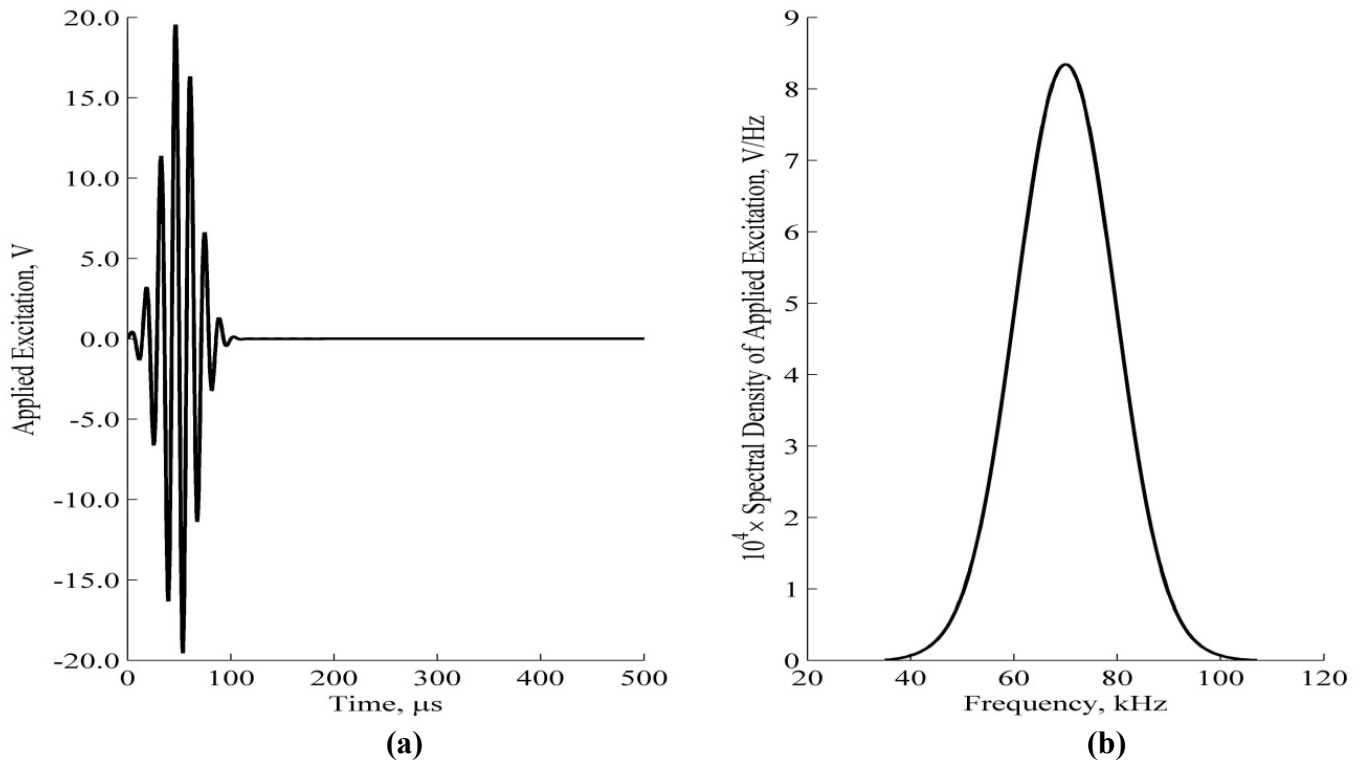


Figure 2.2. Gaussian modulated sine function in (a) time, and (b) its spectral density [9].

2.8 Mechanical Properties of the Cylinder

A 3 in Nominal Pipe Size (NPS) (80 mm Diameter Nominal [DN]), Schedule 40, seamless, carbon steel pipe cylinder is considered. At the end of 1997, for example, there was approximately 40,300 miles (64 900 km) of such pipe in industrial use as energy related pipeline in Alberta, Canada [9]. Consequently it has been studied extensively in, for example, [9, 18, 19]. Then the symmetric matrix of the elastic moduli, \mathbf{D} , can be simplified for such an isotropic material in the form given by equation (A.14) of

³ The notation of [3,9] is used here

Appendix A [9]. Geometrical and material properties of this pipe are summarized in Table 2.1.

Table 2.1. Properties assigned to the unblemished pipe [3].

Property	Assigned Value
Young's Modulus', E (GPa)	206 ± 8
Lame's Constant (Shear Modulus), μ (G) (GPa)	80 ± 5
Lame's Constant, λ (GPa)	94 ± 40
Ratio of lame's Constant, λ/μ	1.2 ± 0.2
Poisson's Ratio, ν	0.287 ± 0.05
Thickness, H (mm)	5.5 ± 0.1
Mean Radius, r_{am} (mm)	41.7 ± 0.1
Outer Diameter, D_o (mm)	88.80 ± 0.08
Thickness to Mean Radius Ratio, H/R	0.134 ± 0.002
Mass Density, ρ (kg/m^3)	7700 ± 300

Then the mean radius of the cylinder, R_m , which is related to D_o and H by:

$$R_m = \left(\frac{D_o - H}{2} \right) \quad (2.48)$$

R_m is 41.7 ± 0.1 mm. Plus and minus variations in a given value represent typical measurement error.

2.9 Dispersion curves and phase speeds

A frequency spectrum shows the relationship between the frequency and (axial) wave number (which is usually termed the dispersion relationship) for modes that can propagate for a given circumferential wave number [9]. By convention, the wave number and frequency are plotted on the abscissa and ordinate, respectively. Results are presented usually in a non-dimensional form. Then the non-dimensional wave number, k^* , is given by [9].

$$k^* = \frac{k}{k_{ref}} \quad (2.49)$$

where k is the axial wave number and k_{ref} is

$$k_{ref} = \frac{1}{H} \quad (2.50)$$

Similarly, the non-dimensional frequency, ω^* , is given by

$$\omega^* = \frac{\omega}{\omega_{ref}} \quad (2.51)$$

where

$$\omega_{ref} = \frac{1}{H} \sqrt{\frac{\mu}{\rho}} = \frac{c_2}{H} \quad (2.52)$$

and

$$c_2 = \sqrt{\frac{\mu}{\rho}} \quad (2.53)$$

is the torsional wave speed. For the cylinder under consideration

$$k_{ref} = 4.542 \text{ in}^{-1} \text{ (} 0.179 \text{ mm}^{-1}\text{)} \quad (2.54)$$

$$\omega_{ref} = 5.829 \times 10^5 \text{ rad / s} \quad (2.55)$$

and

$$c_2 = 10696 \text{ ft/s (} 3260 \text{ m / s).} \quad (2.56)$$

The (non-dimensional) phase speed, c^* , is given by [9]:

$$c^* = \frac{c}{c_2} = \frac{\lambda f}{c_2} = \frac{\omega}{kc_2} = \frac{\omega^*}{k^*} \quad (2.57)$$

where c is the dimensional phase speed and λ (f) is the wavelength (frequency) of a propagating mode. Note that

$$\lambda = \frac{2\pi}{k} \quad (2.58)$$

and the frequency, f , is

$$f = \frac{\omega}{2\pi}. \quad (2.59)$$

Equations (2.58) and (2.59) indicate that the shortest wavelength of a propagating mode is related to the largest (real) wave number. The shortest wavelength determines, in part, the axial spacing that is used later to find the radial displacement field. Define the non-dimensional wavelength, λ^* , as

$$\lambda^* = \frac{\lambda}{H} = \frac{2\pi}{k^*}. \quad (2.60)$$

Then the shortest non-dimensional wavelength that can propagate in the 35 to 107 kHz frequency range of interest is approximately 3.41 [9]. Experience suggests that it is desirable to have at least four spatial points to uniformly cover the distance corresponding to the shortest wavelength in order to reasonably compute the cylinder's displacement field. This restriction corresponds to a non-dimensional axial separation of about $z^* \approx 3.41/4 \approx 0.85$ is defined as [3, 9], where,

$$z^* = \frac{z}{H}. \quad (2.61)$$

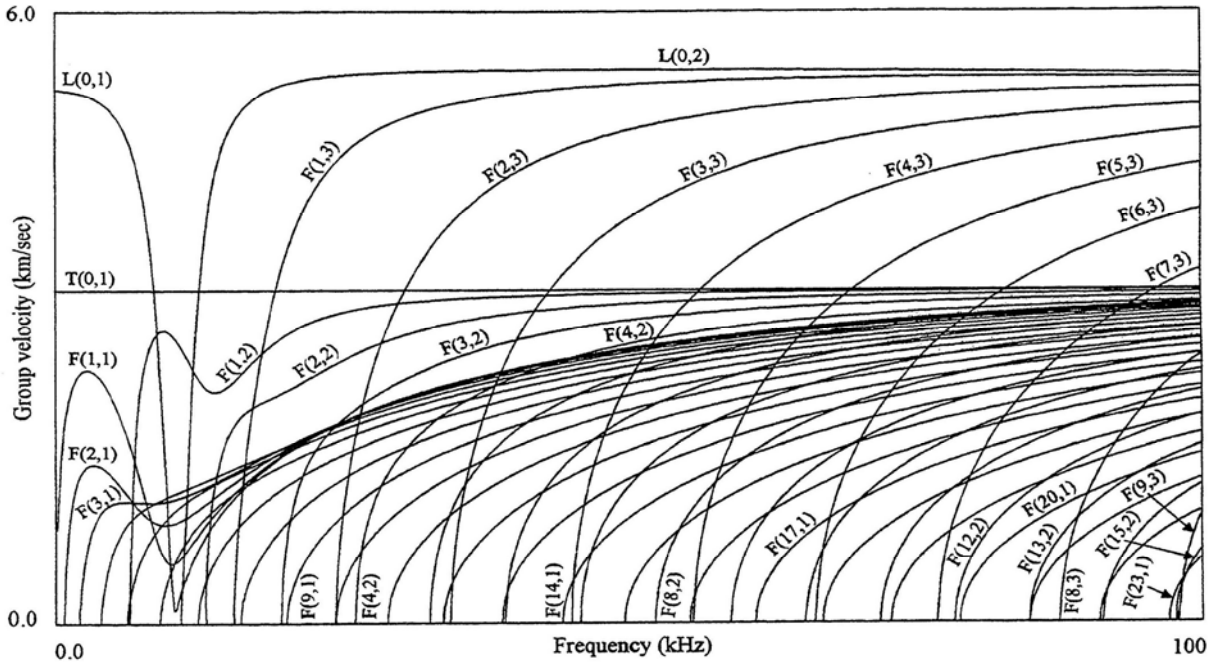


Figure 2.3. Group velocity dispersion curves for a 3 in diameter, steel pipe [18, 19].

A modified version of the scheme used by Silk and Bainton [4] is employed to consistently refer to different modes. The scheme sequentially tracks the modes by their type and circumferential order. For example, modes are labeled $L(0,m)$ for longitudinal axially symmetry, $T(0,m)$, are rotationally axial symmetric modes whose displacement is primarily circumferential and $F(n,m)$ are non-axially symmetric modes. The upper case letters refer to longitudinal, torsional, and flexural modes respectively. In addition to the type of mode, a dual index system uniquely identifies the modes. The first index, n , for instance, gives the harmonic order of the circumferential variation. Consequently all modes with n is zero are axially symmetric. All modes whose first integer is unity have one cycle of variation of the displacement and stresses around the circumference, and so on. The second index, m , is a counter variable. A unity value is associated with the fundamental modes; higher order modes are numbered consecutively. Figure 2.3 shows that the modes travel at different speeds and usually frequency dependent nature are dispersive so that the original wave packet is distorted as it travels through a pipe. Temporal distortion will be seen later to make estimation of cut-off frequencies more difficult. Much of the effort in detecting flaws in pipes has concentrated on the generation of a single, non- dispersive mode in order to make differences from the corresponding unblemished pipe more noticeable and easier to interpret [9, 50].

2.10 Overview of computer simulation

Computer programs outlined in [9, 15] were modified to calculate the approximate wave functions of a homogeneous, isotropic pipe by solving the eigenvalue problem using MATLAB (R2010). Then the eigenvalue and (left and right) eigenvectors were written to file. After storing the eigenvalues and eigenvectors, the temporal response can be

recovered at any spatial location and instant from a modal summation and inverse Fourier transform. (It is important to note that a trapezoidal integration scheme was applied along the real axis to approximately evaluate the inverse Fourier Transform [15]). Ten elements were used to discretize the cylinder's wall for the SAFE procedure. The circumferential angle $2\theta_0$, over which the spatial pulse approximates the Dirac delta function, was taken to be 0.002 (rads). Furthermore, 145 equally spaced frequency points, which correspond to 500Hz increments over 35 kHz to 107 kHz range of interest, were used to solve the eigenvalue problem. This range corresponded to non-dimensionalized frequencies range between 0.377 to 1.153 in which 55 modes, with n equalling to 0 to ± 16 inclusive, propagated. To assess the relative modal contributions to the radial displacement on the external curved surface of the pipe, the lowest three axial modes for n from 0 to ± 16 , inclusive, were inverted on a mode by mode basis [51].

2.11 Illustrative example

Computer code outlined in [9, 15, 51] was modified to (a) form the previously described pipe eigensystem, (b) solve the resulting eigenvalue problem, and (c) perform the modal summations and integrations as described previously. As an illustration, the typical 3 inch Nominal Pipe Size (NPS) [80 mm Diameter Nominal (DN)], Schedule 40, carbon steel pipe, whose assumed properties are summarized in Table 2.1, was considered. The pipe is subjected to the radial excitation described in section 2.7. This excitation is always applied radially, i.e., normal to the pipe's external surface, at $\theta = 0$ in the plane $z = 0$. Moreover, the (body force) amplitude is taken invariably as $A = \mu/H$ which corresponds to a non-dimensionalized unit amplitude. The pipe's displacement is represented by the

radial⁴ component on its outer surface at $\theta = 0$ and $z^* = z/H = 5.1$. This location corresponds to a simple axial offset from the force's application point.

2.12 Data from experiments and comparison with a computer simulation

2.12.1 Preamble

The procedure described in section 2.10 is used to simulate a physical pipe specimen. The specimen was a commercial 3 in NPS (80 mm DN), Schedule 40, seamless, carbon steel pipe, about 114 inches (3.0 m) long. It resembled closely, but not exactly, the one used in the computer simulation. The cut-off frequencies of the F(10,1), F(11,1) and F(12,1) modes (i.e., the same three guided wave modes used in the simulation) were measured [59]. These particular modes were chosen because flexural modes in reflected waves from defects are known to be detectable [18, 19].

2.12.2 Experimental test setup

A series of laboratory experiments was performed to validate the mathematical model described previously. Consistent transducer coupling was achieved and transducer's sensitivity is determined by following the procedure outlined later in section 3.5. A schematic and photograph of the experimental apparatus is shown in Figures 2.4 (a) and (b).

A digital representation of the excitation pulse was programmed into an Agilent Technologies 33120A, 15 MHz, function/arbitrary waveform generator. It was scaled to produce an output signal from the 33120A that was essentially 20 V_{peak-peak} with no Direct Current (DC) component. This voltage signal was applied to the transmitting transducer, a Digital Wave Corporation (DWC) B225, broadband (30 kHz to 300 kHz) ultrasonic transducer. The transducer was coupled carefully to the pipe by applying fairly

⁴ The radial displacement at an external pipe surface is measured most easily.

uniform layer of beeswax to ensure repeatable results. (Additional details are described in chapter 3). The transmitting transducer produced a force which was proportional to the applied voltage. The ensuing radial wave motion at the pipe's outer surface was measured by using a nominally identical transducer coupled similarly to the pipe. The output of the receiving transducer was conditioned by employing a DWC PA2040G/A, broadband (5 kHz to 4 MHz) preamplifier. The conditioned displacement history was captured with an Agilent Technologies DSO6014A, 100MHz digital storage oscilloscope, which was also used to "monitor" the output of the 33120A. Both the 33120A and DSO6014A were "supervised" by a Personal Computer (PC). All interconnections in the analogue measurement chain used shielded, coaxial cables [49].

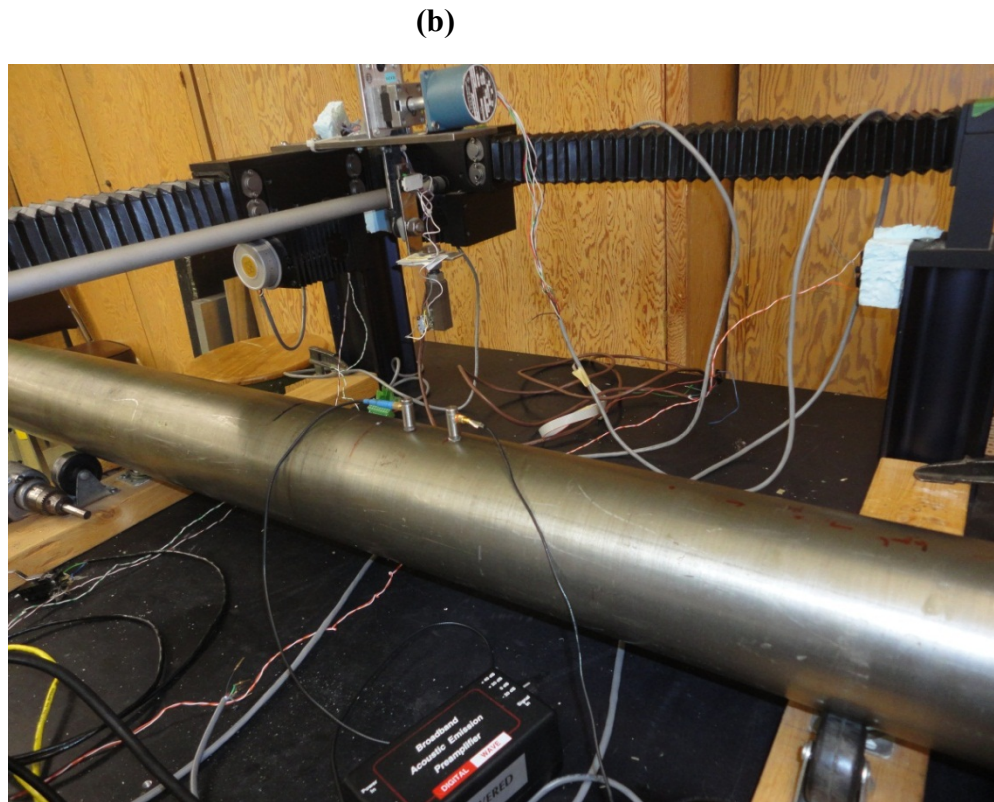
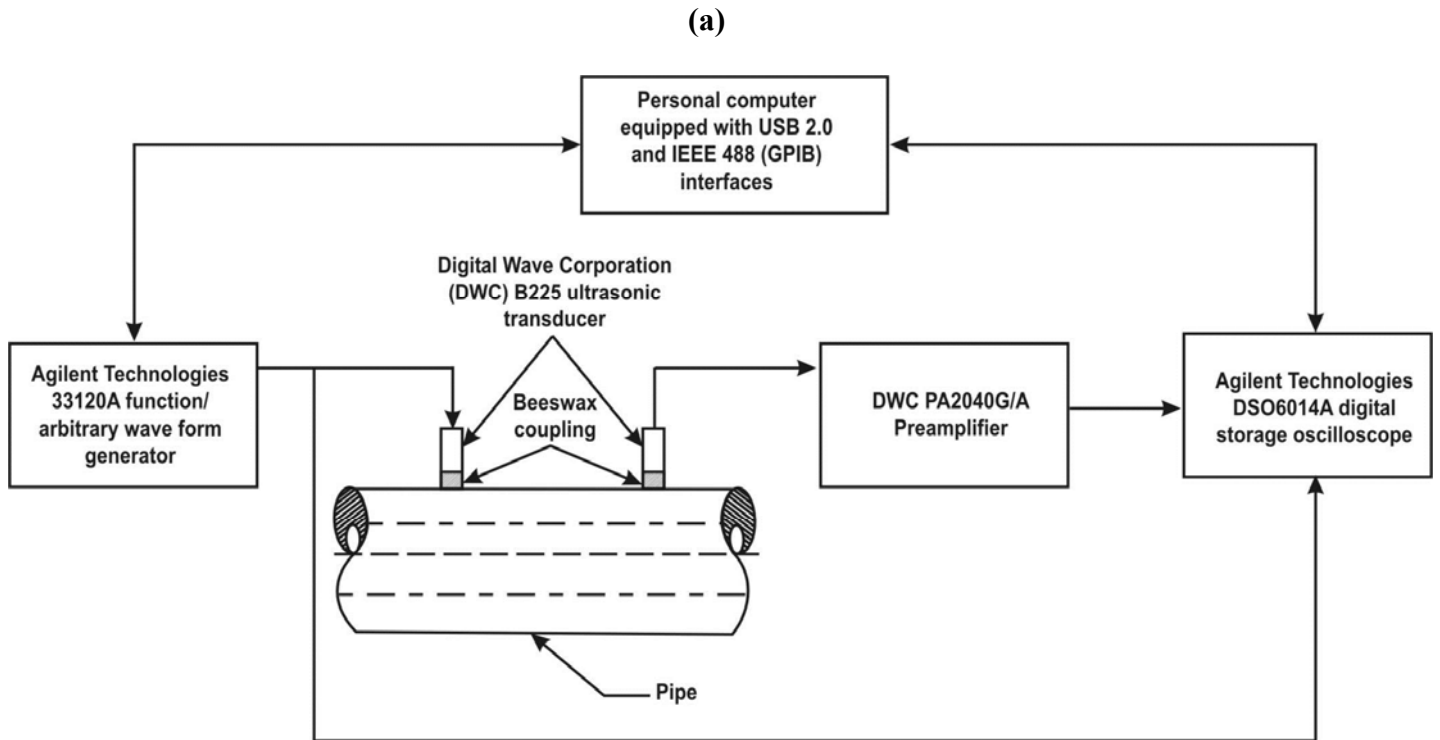


Figure 2.4. (a) Schematic [3] and (b) photograph of the experimental set up

2.14 Experimental components



Figure 2.5. Agilent Technologies 33210 arbitrary waveform generator

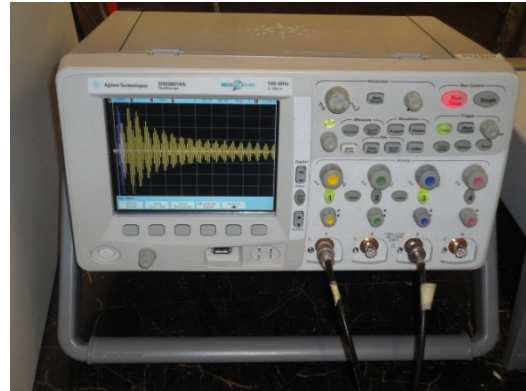


Figure 2.6. Agilent Technologies DS06014A digital storage oscilloscope



Figure 2.7. DWCPA2040GA preamplifier

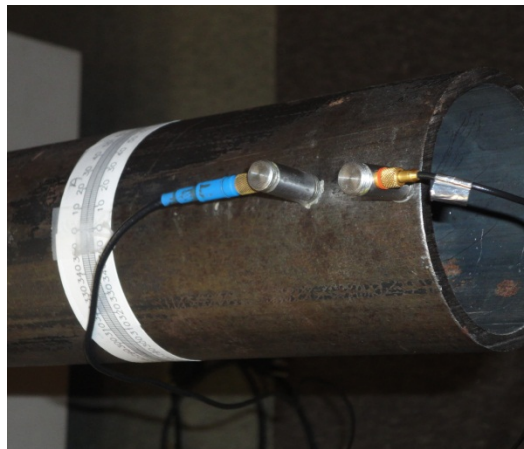


Figure 2.8. Showing transmitting (red band) and receiving (blue band) DWC B225, ultrasonic transducer locations.



Figure 2.9. Complete experimental set-up and data acquisition unit.

2.13 Computer simulation and initial experimental comparison

The differences between the computer simulation and the experimental data presented in Figure 2.10 (a) and 2.11 (a) shows clearly that the experimental time history needs to be post processed to remove artefacts created by the measurement chain. The procedure to characterize the experimental transducer chain and to ensure the repeatability of the frequency behaviour of the instrumentation chain is considered next. It is discussed fully in Chapters 3 and 4. The procedure to eliminate the effect of the instrumentation chain from the experimental data is implemented subsequently,

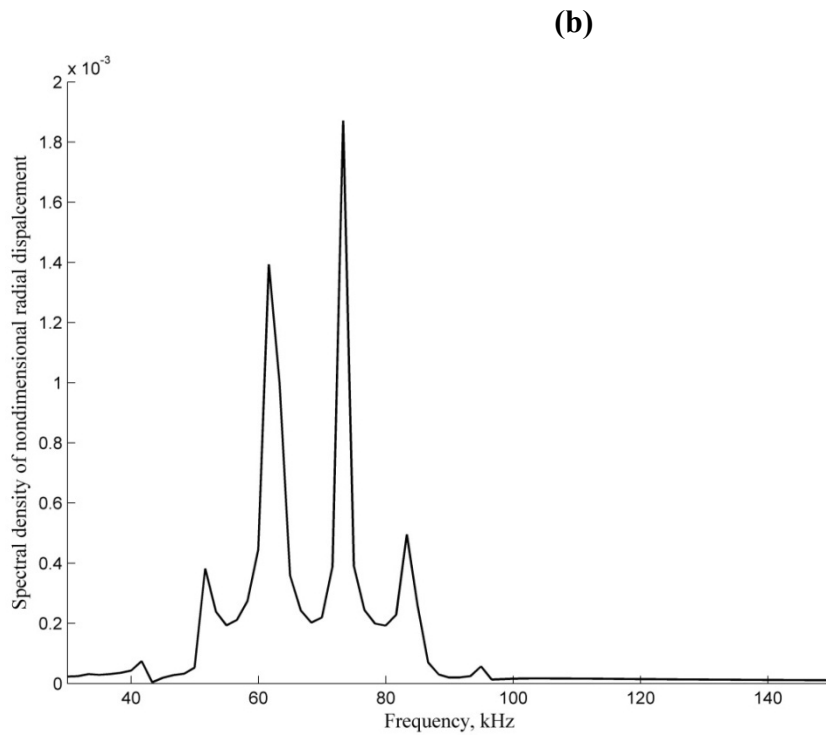
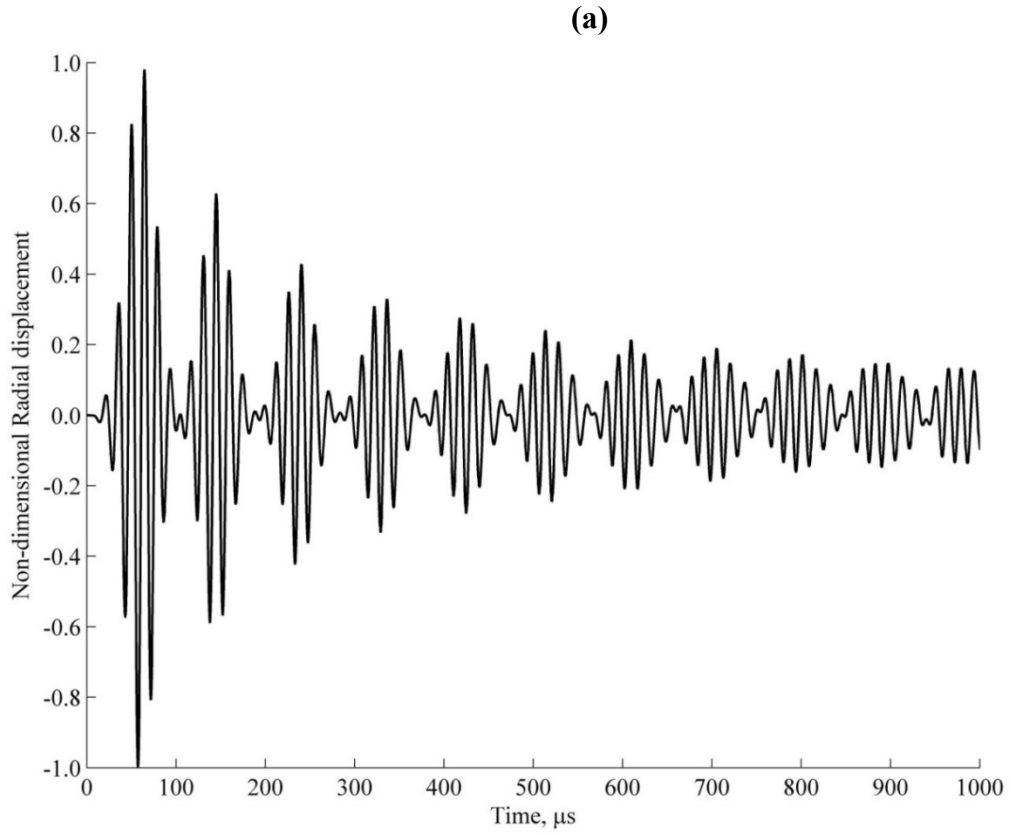


Figure 2.10. Giving (a) the computed time history of the radial displacement on the pipe's outer surface at $\theta = 0$, $z^* = z/H = 5.1$ and (b) the corresponding spectral density with a 500Hz frequency resolution.

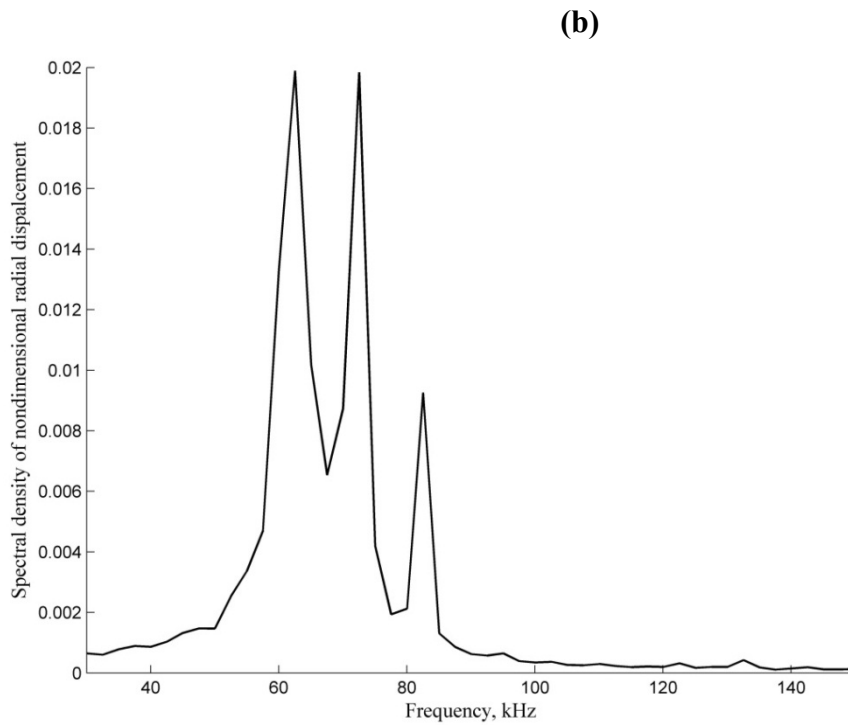
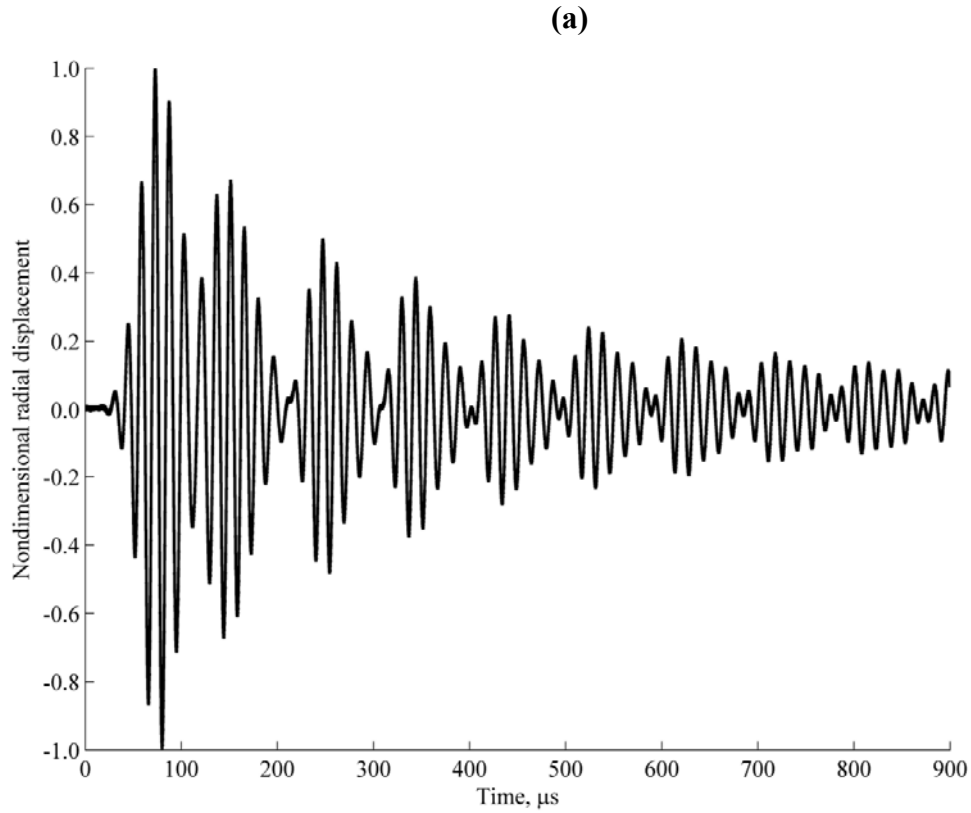


Figure 2.11. Giving (a) the experimental time history of the radial displacement on the pipe's outer surface at $\theta = 0$, $z^* = z/H = 5.1$ with the end reflection time gated out and (b) the corresponding spectral density having a frequency resolution of 500 Hz.

CHAPTER 3

SIGNAL PROCESSING OF ULTRASONIC MEASUREMENTS

3.1 Preamble

Ultrasonic waves are introduced by means of a transducer situated on the external surface of a pipe. As the waves travel through the pipe, they are attenuated by material absorption and the presence of defects [52]. A receiving transducer, which is located away from the source transducer, detects the waves and converts them into a proportional, recordable electrical signal. Therefore a series of experiments was performed to determine a given temporal measurement's repeatability. It has been shown previously [53, 54] that the ambient air temperature and transducer couplant need to remain virtually constant. The first factor may be significant as a result of seasonal changes in the field but it is relatively unimportant under controlled laboratory conditions. Therefore, only the transducer coupling is considered here.

Computer simulation and experimental data processing play an important role in analyzing results and demonstrating a consistent performance. However, a comprehensive understanding of the processes taking place in an actual test specimen is a result of fully acquiring knowledge of the test instrumentation and experimental process. It includes an analysis of the characteristics of the instrumentation being used. This aspect will be discussed later in this chapter. In addition digital signal processing techniques will be described to assure that predicted and computed data are truly analogous. A procedure is described that follows the idea promulgated by Lacoursiere [54] to ensure a consistent beeswax couplant. In essence, a more systematic procedure is followed by forming beeswax from a mould rather than a sheet. The mould controls the

shape of the beeswax before it is cut and used experimentally. Furthermore, it is necessary in modern ultrasonic Non-Destructive Testing (NDT) system to capture received signals so that they can be processed and evaluated quantitatively. This is done through an analogue to digital conversion process in an available digital oscilloscope. Once data is digitized, it can be transferred to a computer for further analysis [52, 55].

3.2 Ultrasonic transducer's characterization

A series of experiment was conducted by Lacoursiere [54] to find a reliable transducer couplant. The repeatability of the frequency response of a given transducer system and steel pipe was investigated for different couplants. Couplants such as super glue and paraffin wax were discouraged at the beginning of this exercise even though the literature [56, 57] suggests that super glue is a good couplant. It suffers, however, from the major drawback that its removal was difficult and the transducer was at the risk of being damaged. Furthermore, paraffin wax was disqualified similarly as it had to be melted by using a fair amount of localized heat [56].

3.2.1 The experimental material and criteria

Having initially disqualified superglue and paraffin wax, the following materials

- 1 plasticine (used for modeling);
- 2 a polymer clay; and
- 3 beeswax.

were considered for a couplant. Parameters other than a couplant were invariably identical

The following criteria were employed to evaluate the performance of the three couplants.

- 1 The amplitude and phase of the Frequency Response Function (FRF) of the transducer should be constant over the time.
- 2 The couplant should have the ability to be curved moulded to the surface of a pipe.
- 3 The couplant should be usable over a reasonable duration.
- 4 A couplant should have the ability to produce the same results during a repeated test.
- 5 Little effort should be required to remove the transducer from the couplant and the couplant from the pipe's surface without any damage.

3.3 Frequency response of the instrumentation chain and transducer coupling

3.3.1 Experimental set-up and data processing

An extensive set of experiments was conducted to characterize a transducer's coupling. The experimental apparatus was arranged as shown schematically in Figure 3.1. The Agilent Technologies waveform generator was programmed to produce a series of separate sinusoidal signals, each having amplitude of 20 V_{peak-peak} and no DC component but with different frequencies. The transmitting transducer was coupled directly to the receiving transducer by using a layer of the different couplants. All the connections were coaxial cables whose essential function was to transmit high frequency signals with low loss and a reflectionless impedance matching without phase or amplitude distortions. The output of the receiving transducer was conditioned by employing the DWC preamplifier configured for no voltage gain. The conditioned output from the preamplifier was captured by employing the Agilent Technologies digital

storage oscilloscope. This configuration characterized not only the receiving transducer and the intermediate coupling but also that of the transmitting traducer because the captured output was compared successfully to the very stable and pure sinusoidal output from the waveform generator [3, 53, 58].

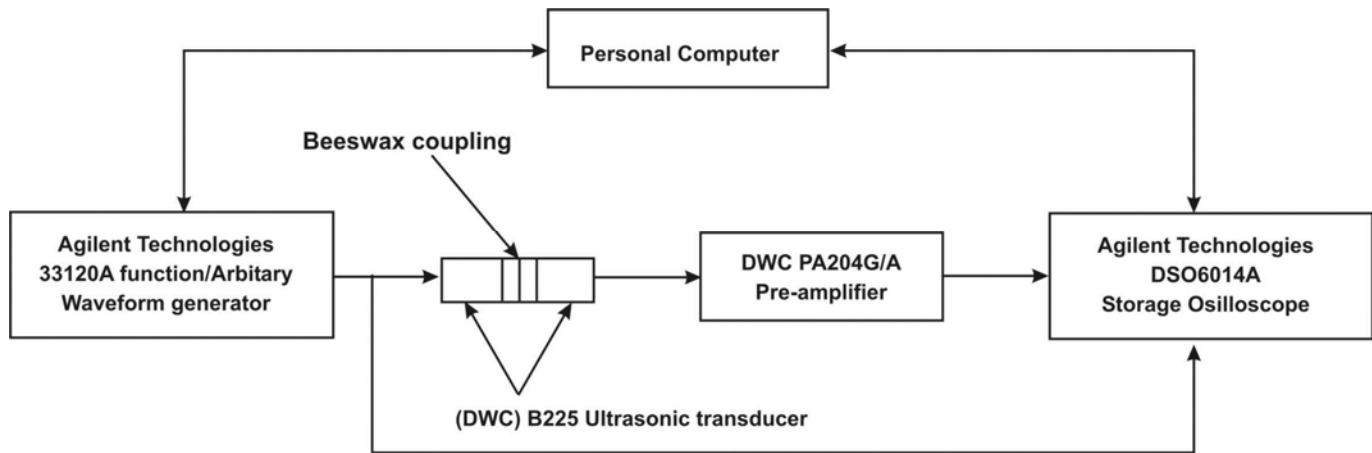


Figure 3.1 Experimental set up for the Frequency Response Function of transducer and associated couplant.

3.3.2 Preliminary experiment and results

The first stage of the experiment involved beeswax, superglue and paraffin wax coupling. A suitable control of the thickness of the couplant layer was achieved by applying a thin, 0.6mm (0.024 inch) thick of each couplant completely between the transmitting and receiving transducers with a fairly equal pressure. The somewhat controlled, ambient air conditions hardly changed as shown in Table 3.1.

Table 3.1 Ambient air conditions for the measured frequency response functions of instrumentation chain.

Temperature	22.8 ± 0.3 °C
Relative Humidity	58 ± 5 %
Atmospheric pressure	1007 ± 50 mBar

Figures 3.2 (a) and (b) show the resulting FRF. The three couplants produced similar trends for different excitation frequencies but the FRF of the plasticine had a low

sensitivity, especially around 50 to 60 Hz. On the other hand, only beeswax had a strong enough bond which is important when the transducer is below the pipe. Therefore the versatility and ease-of-use of beeswax makes it highly desirable. The main advantages of continuing with this method of transducer coupling are its economy, versatility, and simplicity [54]. The previous experiment used a thin 0.6mm (0.024 in) layer of the different couplants. Four different thicknesses of beeswax were considered subsequently. They were 0.6mm (0.024 in), 1.34mm (0.054 in) and 2.60mm (1.04 in).

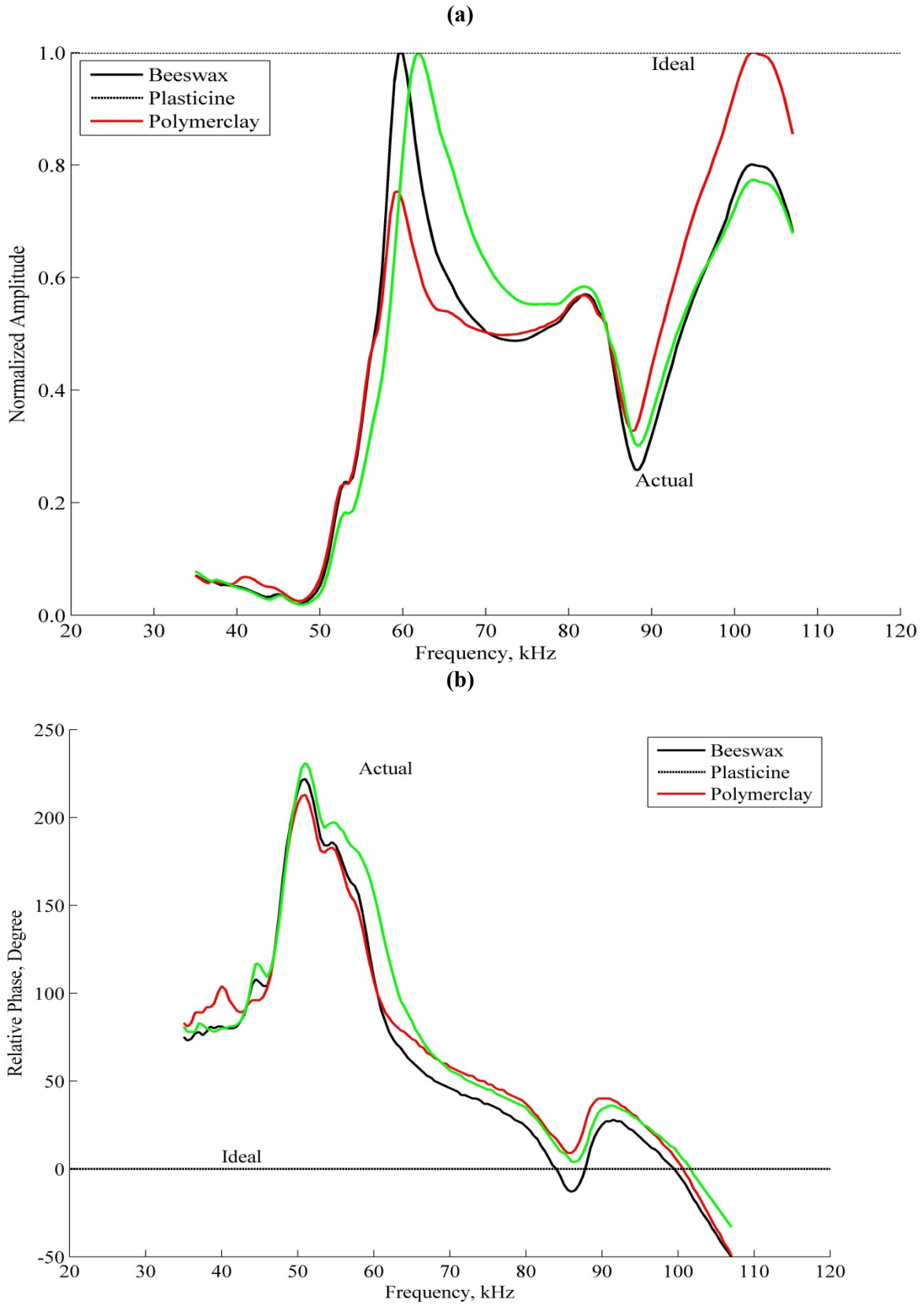


Figure 3.2. Comparison of receiving chain's (a) frequency response function and (b) corresponding phase using different couplants.

The thin layer 0.6mm (0.024 inch) thickness, is considered has a generally acceptable; two thicker layers led to too low signal. An investigation of the repeatability of results from a repeated tests proposed in [54] is presented later in section 3.5.

3.4 Experiment with beeswax uncontrolled coupling

It is important to know how the thickness of a beeswax coupling and the frequency resolution changes a given transducer's FRF. Figures 3.3 (a) and (b) presents the relationship between the amplitude and phase sensitivities obtained for different beeswax thicknesses and frequency resolutions. It is shown further in Figure 3.3 that LT R500Hz⁵ is more sensitive than HT R500Hz which shows, in principle, that the lower is the couplant's thickness, the better is the transducer's sensitivity. There is little difference between the 50Hz and 500Hz frequency resolutions except below about 60 kHz. This region has little consequences for the F(10,1), F(11,1) and F(12,1) modes considered later.

Producing beeswax layer from a mould would allow limited control over its thickness. The general procedure to ensure this repeatability is discussed further in section 3.5.

⁵ LT and HT indicate a 0.6mm and 2.60mm beeswax layer, respectively. On the other hand, R50Hz and R500Hz correspond respectively, to frequency resolutions of 50Hz and 500Hz.

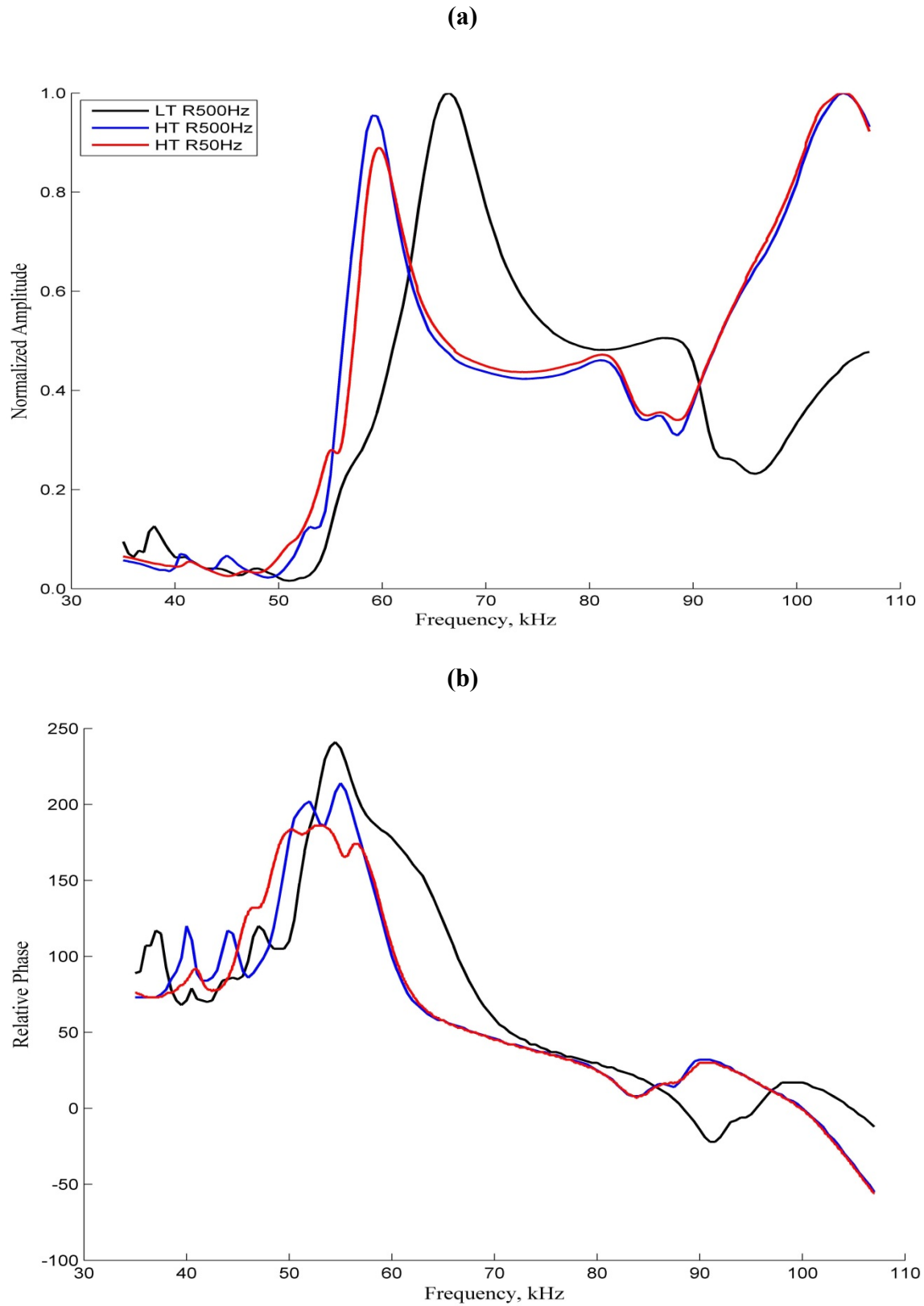


Figure 3.3. Comparison of (a) amplitude and (b) phase of nominally identical frequency response functions of receiving transducer chain with an uncontrolled beeswax coupling.

3.5 Experiment with beeswax controlled coupling

Eight separate experiments were conducted as described in section 3.3.1 to determine changes in the frequency response function of a given transducer but with nominally identical beeswax coupling having a thickness of 0.6mm (0.024 ± 0.001 in). The surface of the transducer is invariably smooth and clean for each experiment. The results given in Figure 3.4 demonstrate that the eight FRFs agree closely except around 100 kHz a value essentially outside the region of later interest. However, the formation of a beeswax slug was found to be crucial [54]. Two cases were considered to further validate the method by proposed Peter Lacoursiere [54] both were successful. A mould of diameter 9.60mm (0.377 in), which is the same as the diameter of the transducer, was made to produce beeswax. Beeswax was melted in a residential oven and poured into the prepared mold. Then the beeswax was allowed to solidify, the second approach proposed in [54] was to create a beeswax layer by melting beeswax on a flat surface in a residential oven. Then slowly and carefully cooling the beeswax at a controlled temperature. Individual cylindrical slugs were punched subsequently from the sheet so that each beeswax slug had a diameter of 0.25 in (6.35 mm) and a height of 0.028 ± 0.003 in (0.53 ± 0.08 mm) [54]. However, a mould needed to be constructed to ensure a constant thickness. The first approach worked well but a cavity was needed for the mould to ensure its stability. Therefore the mould was used throughout this thesis. Normalization of a FRF followed the same procedure as that described in section 3.3.1. The FRF of the instrumentation chain for eight different tests are presented in Figure 3.4. The results are seen in Figure 3.4 to be respectably repeatable with no frequency shift.

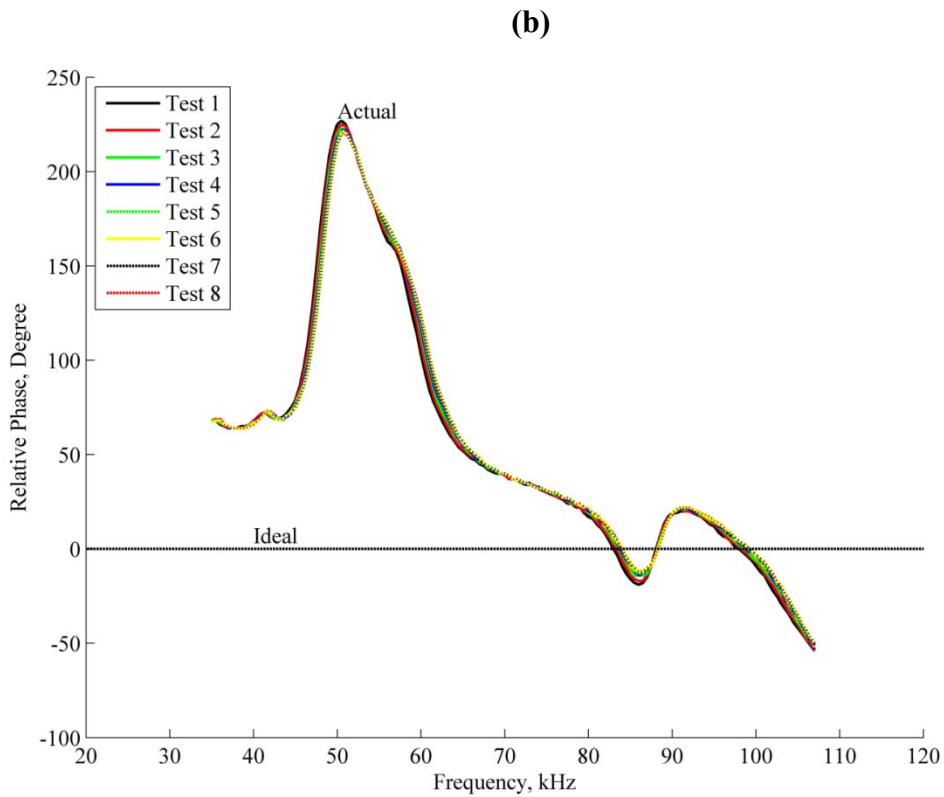
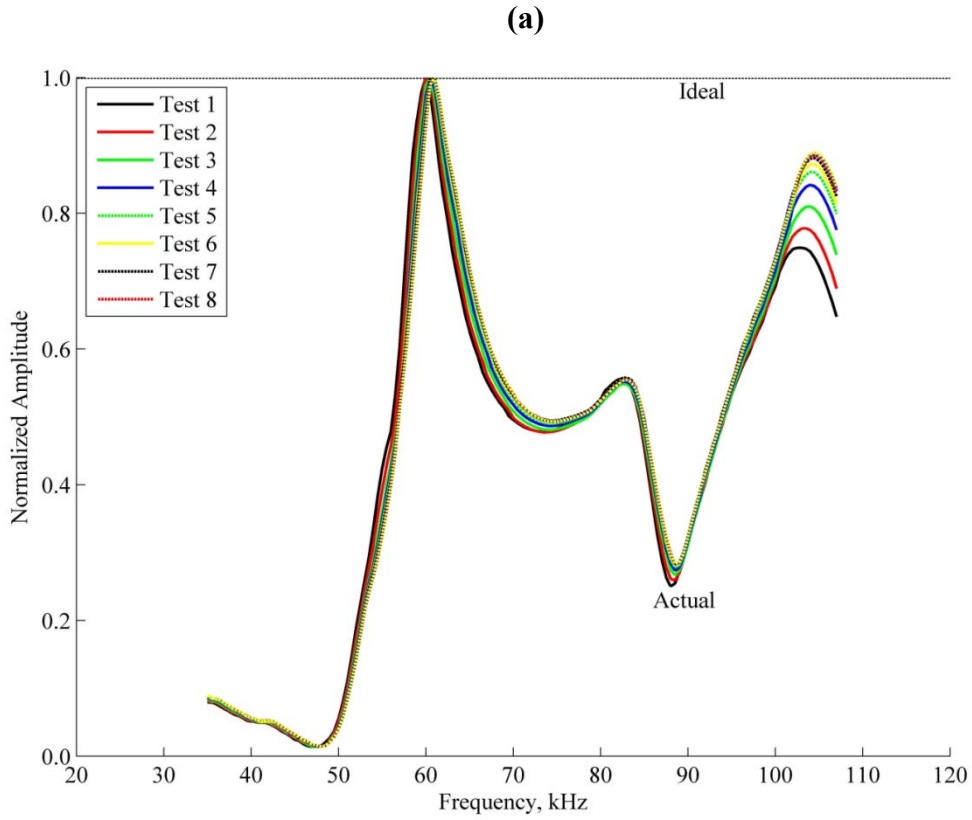


Figure 3.4. Comparison of better controlled experimental frequency response functions of receiving transducer chain showing (a) amplitude and (b) phase.

3.6 Data collection and analysis

Amplitudes and phases were obtained for different signals over a range of frequencies, ω , as described in section 3.3.1. The Gaussian input excitation and the resulting frequency response functions of the instrumentation chain were determined to simulate the transducer's time history. Then computer calculations were performed by using MATLAB 2010a software (See Appendix F). A Fourier transform was evaluated by means of the supported FFT algorithms (**fft** routine in Matlab). The correlation of the radial displacement of an idealized cylinder (obtained from SAFE) and that initially incorporating and subsequently eliminating the effect of a typical transducer chain was performed by using the auto and cross-correlation functions in Matlab.

3.7 Determining the transducer's Frequency Response Function

The experimental data i.e. amplitude in (volts) of the receiving transducer, its phase (degrees) and frequency (Hz) are obtained from the arrangement illustrated in Figure 3.1. Experimental data are processed to obtain the amplitude and phase of the receiving transducer's sensitivity. These variables are given in Figures 3.5 (a) and (b), respectively.

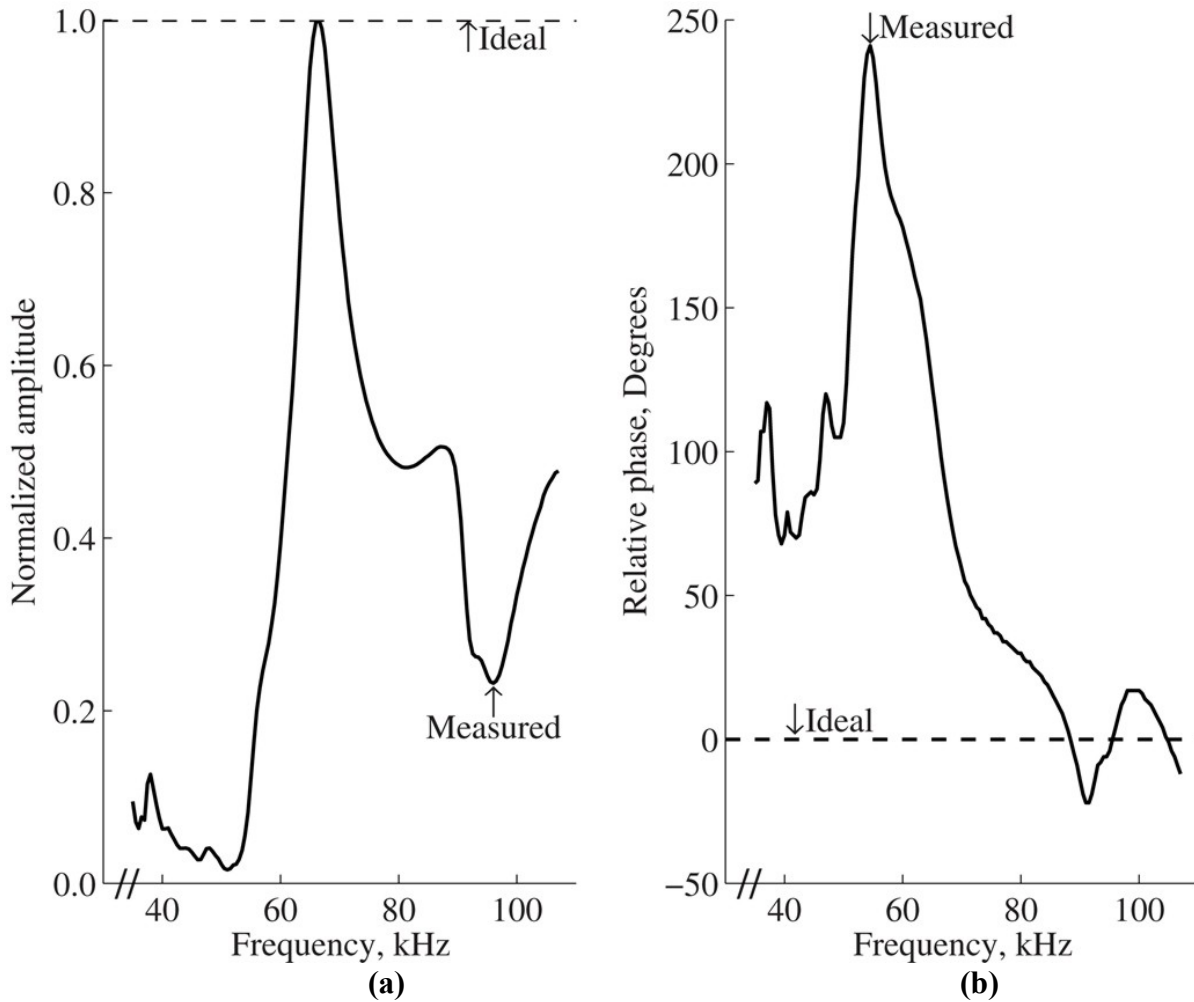


Figure 3.5. Relative frequency response of transducer chain in (a) amplitude and (b) phase
 Figures 3.5 (a) and (b) show that the receiving transducer’s sensitivity is far from an ideal, horizontal line which indicates frequency independence. Consequently the accuracy of this behaviour is assessed by comparing the predicted with a measured response time history. This comparison is provided in section 3.8.

3.8 Simulating the output response of a transducer

Consistency of the instrumentation chain FRF shown in Figure 3.5 is considered next. The dynamic behaviour of all the components of the ultrasonic measurement set up are measured and represented mathematically. The Gaussian modulated sine function shown previously in Figure 2.2, for example, can be modelled by using MATLAB 2010a script.

The resulting approximation is convolved with the frequency response function, $H_m(\omega)$, of the measurement chain, as shown in Figure 3.5. The purpose of this convoluted procedure is to obtain the predicted response. This is simply and easily performed in the frequency domain and subsequently finds the inverse Fourier Transform. The convolution is performed here by multiplying the complex FRF and the Fourier transform of the transient point force at 145 frequency points. Then the inverse Fourier transform is taken of the convolution to return to the time domain. The corresponding mathematical procedure is given in equations (3.1) and (3.2) below.

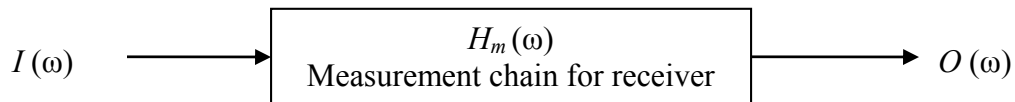


Figure 3.6. Block diagram illustrating the procedure to predict the response given in Figure 3.7.

Mathematical operations:

$$I(\omega)H(\omega)=O(\omega) \quad (3.1)$$

Taking the inverse Fourier transform of equation (3.1) gives,

$$\mathfrak{F}^{-1}\{O(\omega)\}=o(t). \quad (3.2)$$

The result of the practical implementation of equations (3.1) and (3.2) is presented in Figure 3.7. It is compared with the measured time history obtained from the storage oscilloscope. This measured time history is obtained directly from the set-up presented in Figure 3.1. The input force drives a transmitting transducer and a separate receiving transducer converts the received signal into an electrical signal which is displayed on the storage oscilloscope.

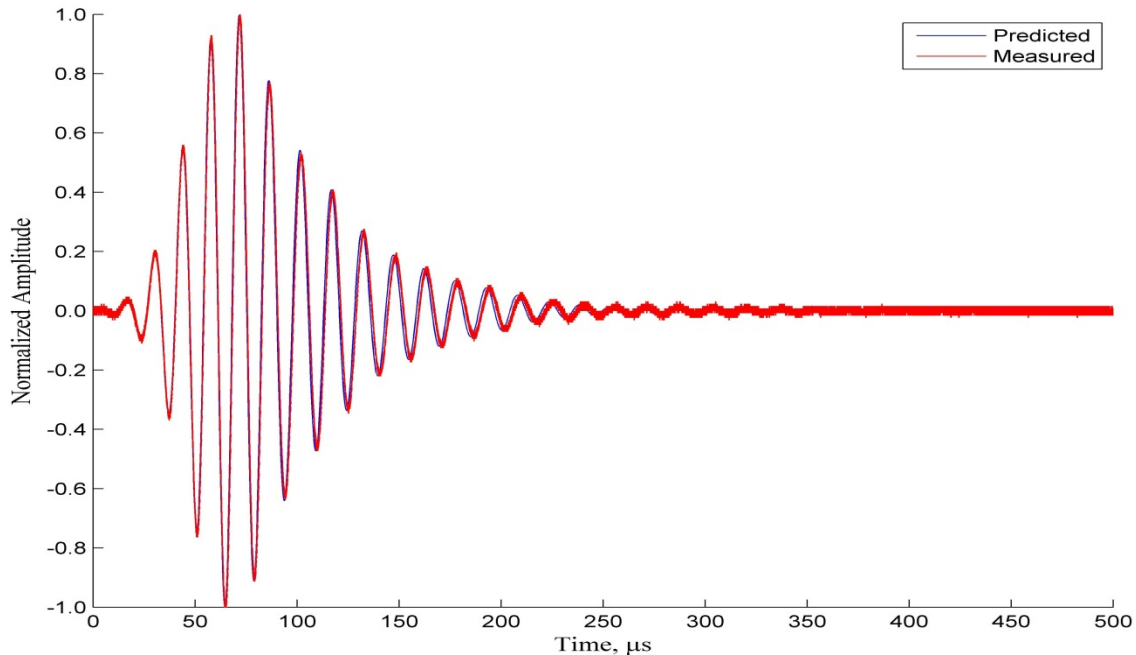


Figure 3.7. Time history of transducer's measured and predicted response.

Figure 3.7 compares the measured and the predicted time histories (obtained from equation (3.2) by incorporating the experimental amplitude, frequency and phase information of the receiving measurement chain. It can be seen from Figure 3.7 that the curves essentially overlap so there is a very good agreement between the measured and predicted responses over the frequency range of interest. The repeatability of the measurement chain's frequency response function depends especially on the phase which is critical in implementing an inverse procedure. This aspect is considered further in section 3.9.

3.9 Preliminary tests of computer software

Having determined the repeatability of the Frequency Response Function of the instrumentation chain, an inverse function to remove the effect of the instrumentation chain is developed and described further in this section. It is assumed that the system is linear and time invariant (LTI). To additionally check the accuracy and validity of the

inverse function, $H_m^{-1}(\omega)$, the convolution of the Gaussian modulated sine function in the frequency domain, $I(\omega)$, and the frequency response of the receiver's measurement chain, $H_m(\omega)$, are convolved with the inverse function, $H_m^{-1}(\omega)$ of the measurement chain. It is worth noting here that the convolution is performed by multiplying the complex FRF, the inverse function, $H_m^{-1}(\omega)$, and the Fourier transform of the input signal at 145 frequency points, i.e. with a 500Hz frequency resolution. This operation is illustrated for additional clarity in Figure 3.8. The Inverse Fourier Transforms (IFT) is taken after the multiplication to return to the time domain. Then a comparison is made in Figure 3.9 with the precisely known Gaussian input signal.

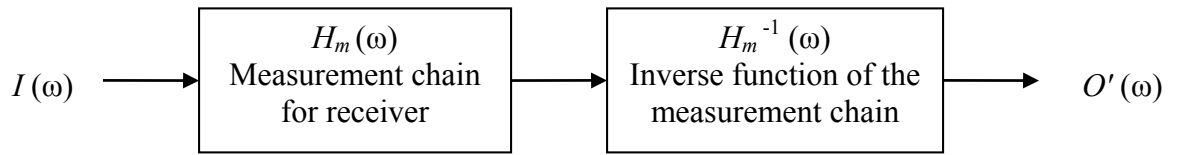


Figure 3.8. Block diagram pertinent to Figure 3.9

Mathematical operation:

$$I(\omega)H_m(\omega)H_m^{-1}(\omega) = O'(\omega) \quad (3.3)$$

Taking the inverse Fourier transform of equation (3.3), gives,

$$\mathfrak{F}^{-1}\{O'(\omega)\} = o'(t). \quad (3.4)$$

Then a comparison is made of the Gaussian input signal with the expected output response obtained from inverse procedure for which $\mathfrak{F}^{-1}\{I(\omega)\}$ should equal $\mathfrak{F}^{-1}\{O'(\omega)\}$.

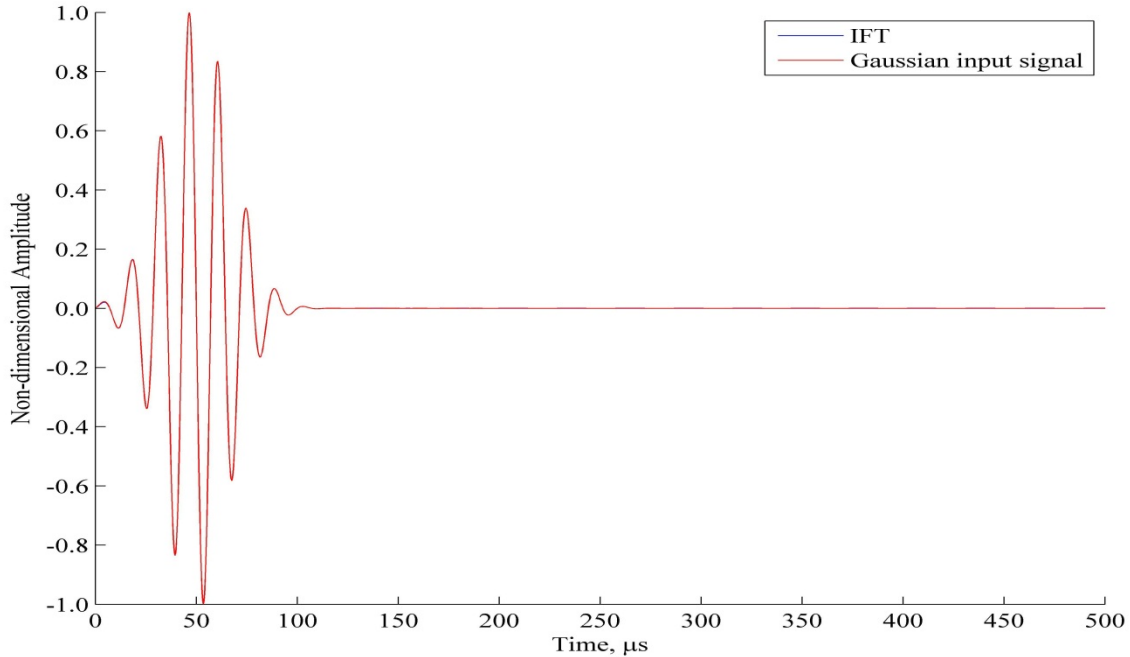


Figure 3.9. Comparison of Gaussian input with the convolution of inverse FRF of measurement chain.

This comparison, which is presented in Figure 3.9, shows overlapping curves that the agreement is excellent because the root mean square difference between $\mathfrak{T}^{-1}\{I(\omega)\}$ and $o'(t)$ does not exceed 0.02% over the complete time histories.

3.10 Comparison of generic response time histories computed directly in time and indirectly from frequency domain.

An additional, further quick check is undertaken to confirm the amplitude and phase changes over a range of frequencies. The input Gaussian modulated sine function in time, $i(t)$, is convolved with the system impulse response, $h(t)$, which produces the output response, $o(t)$. This operation is illustrated conveniently in Figure 3.10. The corresponding mathematical operation is:

$$i(t) \times h(t) = o(t) \quad (3.5)$$

where \times denotes the convolution operator.

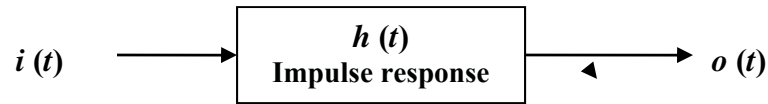


Figure 3.10. Block diagram illustrating a generic convolution in time.

The result is presented in Figure 3.11. A comparison is made with the previous predicted response given in Figure 3.7. It is presented in Figure 3.12.

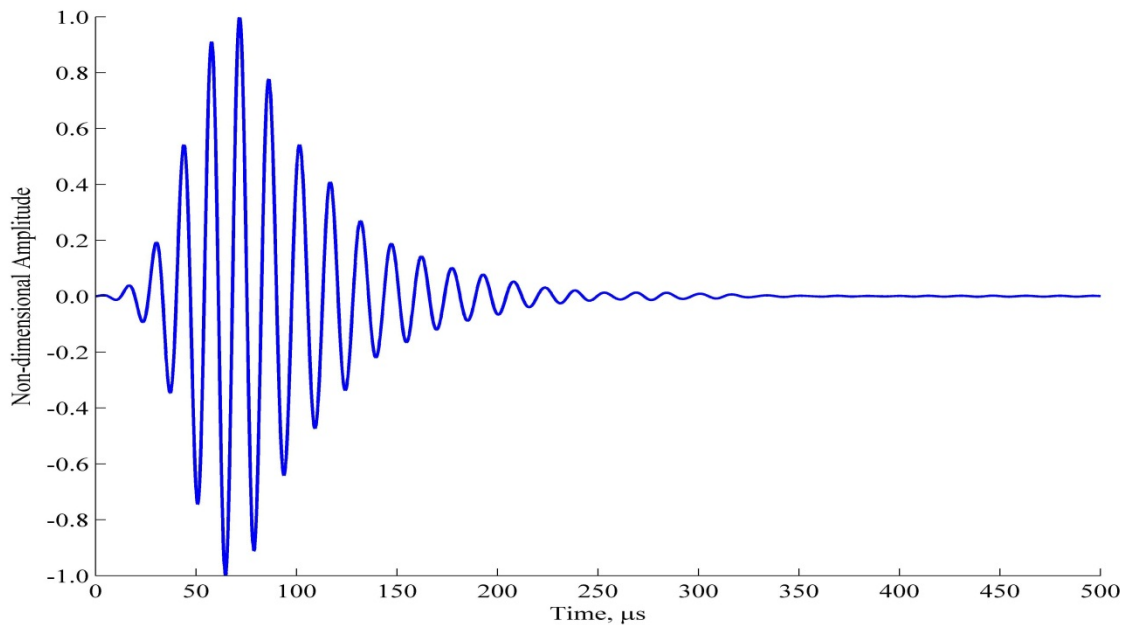


Figure 3.11. Convolution of the product of the Gaussian input (in time) and the system's impulse response function.

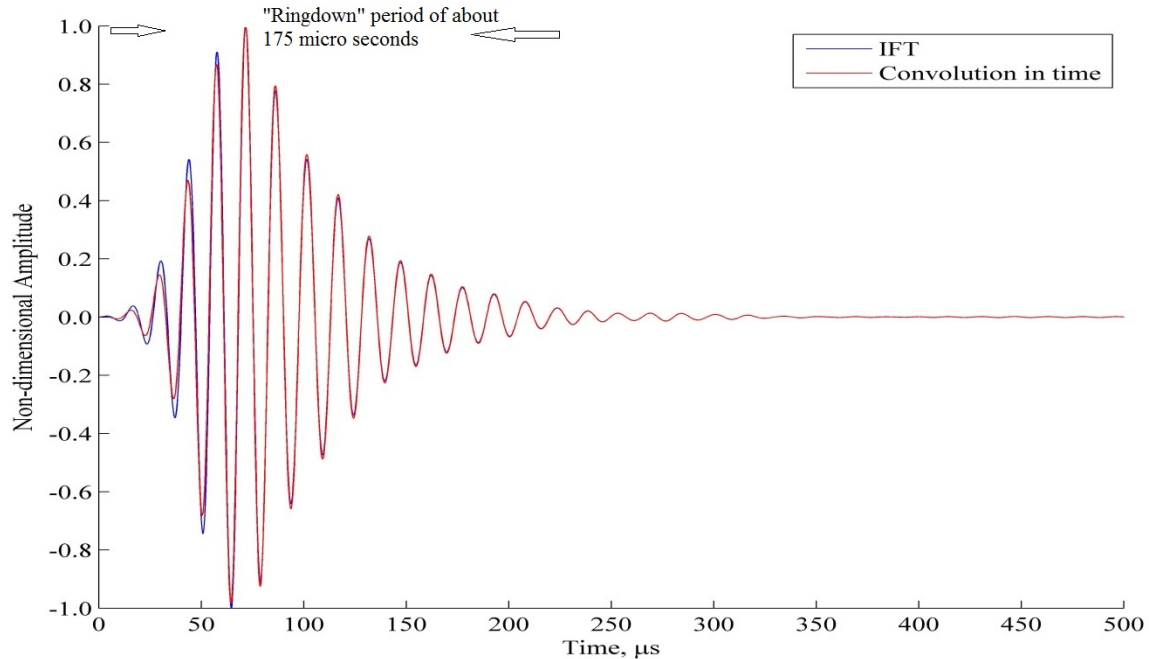


Figure 3.12. Comparison of generic response time histories computed directly in time and indirectly from the frequency domain.

A comparison of Figures 3.7 and 3.12 shows that the agreement between the convolution in time and the inverse Fourier transform of the multiplication in frequency is good. Indeed, the root mean square difference between the two sets of amplitudes does not exceed 2.3% over the complete time histories. This level of agreement suggests that the frequency varying amplitude of the output transducer chain introduces little error. Therefore, the previously inverse function, of the measurement chain, $H_m^{-1}(\omega)$, is reliable. It is used in the next chapter to eliminate the effect of the experimental transducer's imperfect receiving chain.

CHAPTER 4

ELIMINATING THE EXTRANEIOUS BEHAVIOUR OF A TYPICAL ULTRASONIC TRANSDUCER

4.1 Preamble

The computer simulation shown in Figure 2.10 (a) is compared with the corresponding experimental data at a simple axial offset of $z^* = 5.1$. This comparison necessitates the further validation of the inverse procedure of the instrumentation chain's frequency response function described in chapter 3. The purpose is to eliminate this extraneous behaviour of the measurement chain from the experimental data. The previous mathematical model, on the other hand, however, assumes that the measurements are perfect (i.e., the ideal situation of a horizontal FRF for the transducer chain). This assumption can lead to noticeable differences which can be seen even in a casual comparison of Figures 4.4 (a) and (b). The former figure shows the radial displacement created by a Gaussian modulated sine wave on a pipe's external surface with an instrumentation chain (which includes beeswax coupling) having the characteristics of Figure. 3.5. Figure 4.4 (b) on the other hand, presents the computed, ideal counterpart [53]. Further discrepancies are also introduced when periodicity is assumed, as in a DFT, to obtain frequency information corresponding to transient response history. Furthermore causality (which requires an effect to occur after the cause's start) may not necessarily be obeyed. Data leakage caused by non-periodicity or the result of non-causality can be ameliorated by using the standard approach of employing an exponential time window with an empirically found, 15% effective damping [53, 58].

Then the previously described extraneous influences shown in Figure 4.4 (b) may be reduced by taking the following steps [58].

1. Apply an exponential time window to the experimental history of Figure 4.4 (b).
2. Take the Discrete Fourier Transform (DFT) of the result of step 1 and multiply it with the inverse transform of the measurement chain's frequency behaviour given in Figure 3.5
3. Use the inverse DFT to return from the frequency to the time domain and compare the result with Figure 4.4 (a). The result is virtually indiscernible from the history given in Figure 4.4 (a).

4.2 Overview of inverse procedure for steel pipe

Chapter 2 discussed wave propagation functions used to implement an inverse procedure. Chapter 3 provided a procedure to determine the repeatability of the frequency response function of transducer's imperfect frequency behaviour. Also, the accuracy of the experimental data (i.e. amplitudes and phases extracted over a range of frequencies) has been verified in the previous chapter. Having tested the inverse procedure, the idealized cylindrical response is simulated by using a SAFE computer model. The reason for this approach is to provide an ideal situation in which everything is known (which is impossible in practice). In addition, a separate computer model which incorporates the measurement chain's actual dynamic behaviour is simulated and compared with an experiment. The agreement is very good. Subsequently, the inverse procedure is introduced to negate a measurement chain's effect. The ensuing result is compared with the computed response of an idealised cylinder from SAFE. For convenience, only one radial displacement of the pipe (which is simulated at a simple axial offset from the

transmitter) is considered. The simulated or predicted response of the idealized cylinder is considered. Its material and dimensional properties are similar to the ones given in Table 2.1. They are based on the arithmetic average of values measured conventionally and ultrasonically [3, 53].

4.3 Predicting the temporal response of an idealized cylinder by using SAFE

In order to make the experiment comparable with its ideal counterpart, firstly, the idealized pipe's radial displacement is reconsidered on its outer surface at a circumferential offsets, and axial of $\theta = 0$ and $z = 5.1H$, respectively. The overall radial displacement is simulated, on a mode by mode basis, by convolving the pipe's frequency response function, $H_c(\omega)$, with the Fourier transform of the transient Gaussian modulated sine excitation, $I(\omega)$, at known individual frequencies. The Inverse Fourier transform is taken which subsequently gives the output response, $O_c(\omega)$, corresponding to the time variation, $o_c(t)$. This procedure is illustrated in Figure 4.1 and, in turn, explained mathematically in equations (4.1) and (4.2).

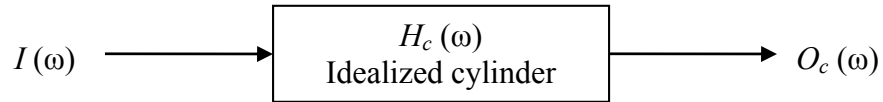


Figure 4.1. Block diagram illustrating prediction of temporal response of idealized cylinder without measurement chain.

Mathematically:

$$I(\omega)H_c(\omega) = O_c(\omega) \quad (4.1)$$

Taking the inverse Fourier transform of equation (4.1), gives,

$$\mathfrak{F}^{-1}\{O_c(\omega)\} = o_c(t). \quad (4.2)$$

The result obtained from equation (4.2) is given in Figures 4.2 (a) and (b) in time and frequency, respectively. Figure 4.2 (a) shows the radial displacement history measured on

the steel pipe's outer surface at $\theta = 0$ and $z_* = z/H = 5.1$. Initial approximations of the cut-off frequencies, their amplitudes, and phases are elicited from the DFT of this history. The magnitude of the DFT is presented in Figure 4.2 (b). These approximations are utilized in the temporal curve fitting procedure which is discussed fully in Chapter 5.

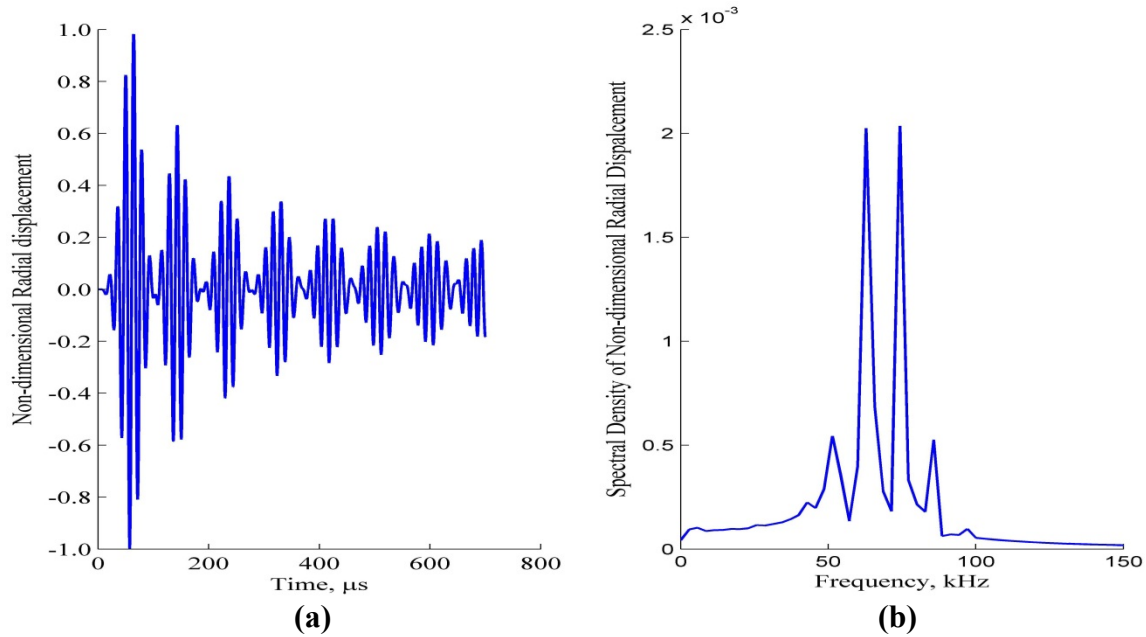


Figure 4.2. Idealized time history (a) predicted at $\theta = 0$, and $z = 5.1H$ without the effect of measurement chain and (b) the corresponding spectral density.

Experiments have shown that a measured displacement time history is imperfect due to the effect of the measurement chain, $H_m(\omega)$. The reason for predicting the displacement of an idealized cylinder is to have a “feel” of the ideal situation. A comparison with a measured response obtained from the inverse procedure to remove the effect of the measurement chain is provided later. Further details are given next.

4.4 Including the measurement chain, $H_m(\omega)$, in idealized cylinder's frequency response function, $H_c(\omega)$, to simulate the measured frequency response, $O_{cm}(\omega)$.

The response found experimentally necessarily includes the effect of the measurement chain. For comparison and to verify the faithfulness of a measurement, the frequency response function, $H_m(\omega)$, of the measurement chain (presented previously in Figure 3.5)

is convolved in the frequency domain with the frequency response of an idealised cylinder (obtained from a SAFE computer simulation) and a Gaussian modulated sine wave. The resulting convolution is transformed back to the time domain to obtain the response history of the idealized cylinder. This history is compared with experiment and reasonable agreement is found. The result is shown in Figure 4.4 (b) by applying a linear interpolation scheme between discrete data points. Finally, the inverse Fourier transform is taken to return to the time domain. This procedure is illustrated in Figure 4.3. It is explained mathematically by equations (4.3) and (4.4).

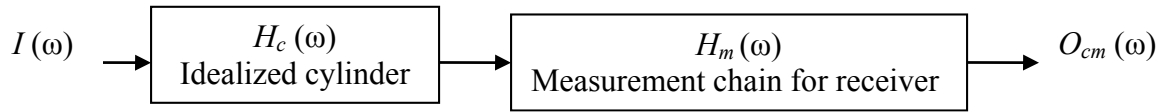


Figure 4.3. Block diagram illustrating the procedure to incorporate the measurement chain's effect.

Mathematical operation,

$$I(\omega)H_c(\omega)H_m(\omega) = O_{cm}(\omega) \quad (4.3)$$

Taking the inverse Fourier transform of equation (4.3) gives

$$\mathfrak{F}^{-1}\{O_{cm}(\omega)\} = o_{cm}(t). \quad (4.4)$$

The result of implementing equations (4.3) and (4.4) is presented in Figure 4.4 (b). Any difference between Figures 4.4 (a) and 4.4 (b) arises from the effect of the measurement chain. (This assertion can be verified by directly comparing equations (4.1) and (4.3)). Figure 4.4 compares the ideal and experimental time responses of the radial displacement of the pipe at an axial offset of 5.1H and a circumferential offset of 0°. The difference between the two histories is associated with the effect of the instrumentation chain and associated transducer couplant. The procedure is discussed next.

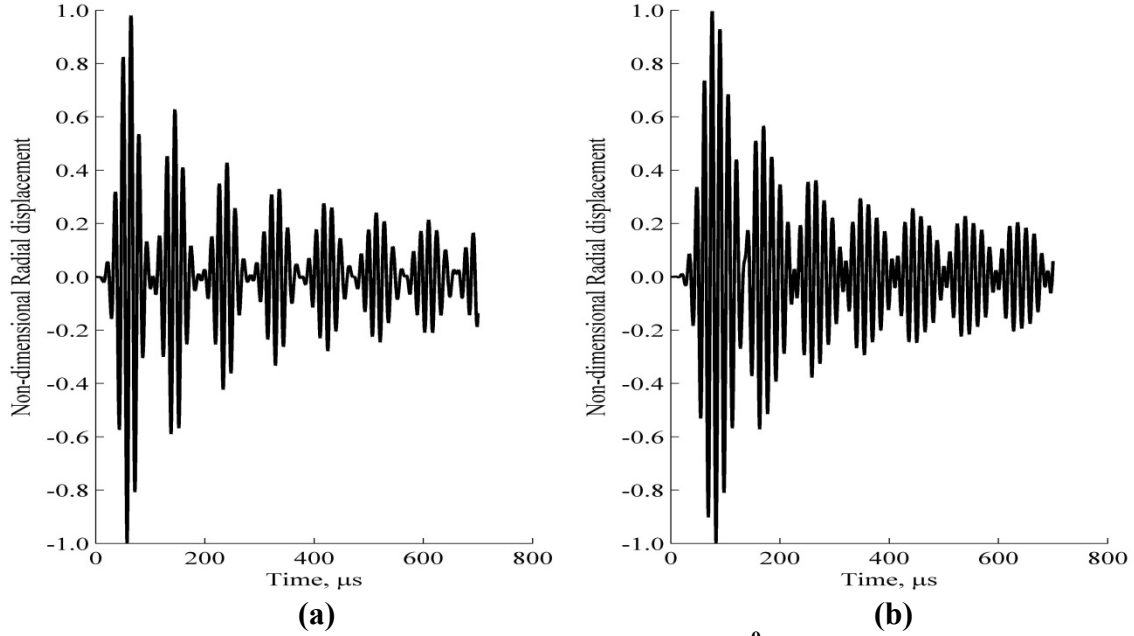


Figure 4.4. Showing (a) simulated time history at $\theta=0^0$ and $z = 5.1H$, and (b) the corresponding experimental history which includes the effect of the measurement chain.

4.5 Inverse procedure to remove the effect of output measurement chain, $H_m(\omega)$, from measured cylinder's time response, $o_{cm}(t)$

Ensuring that the frequency response function of the instrumentation chain is independent of the thickness of the beeswax coupling is very important. Therefore, the inverse procedure described in section 3.9 is implemented to ameliorate the effect of the measurement chain. To remove the transducer's effect from the (response) output's temporal history, $o_{cm}(t)$, presented in Figure 4.4 (b), a DFT is taken of the latter and multiplied by the inverse function of the measurement chain, $H_m(\omega)$, as illustrated in Figure 4.5.

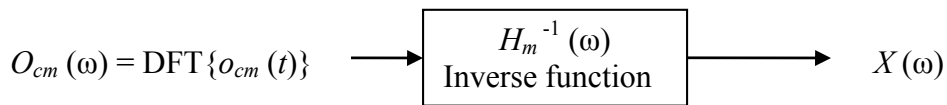


Figure 4.5. Block diagram illustrating the way of ameliorating the effect of the measurement chain.

This procedure is described mathematically as:

$$\text{DFT}\{o_{cm}(t)\}H_m^{-1}(\omega) = X(\omega). \quad (4.5)$$

Then the modified response history, $x(t)$, is obtained by taking the inverse Fourier transform of $X(\omega)$, i.e.

$$\mathfrak{F}^{-1}\{X(\omega)\} = x(t). \quad (4.6)$$

The result is presented graphically below.

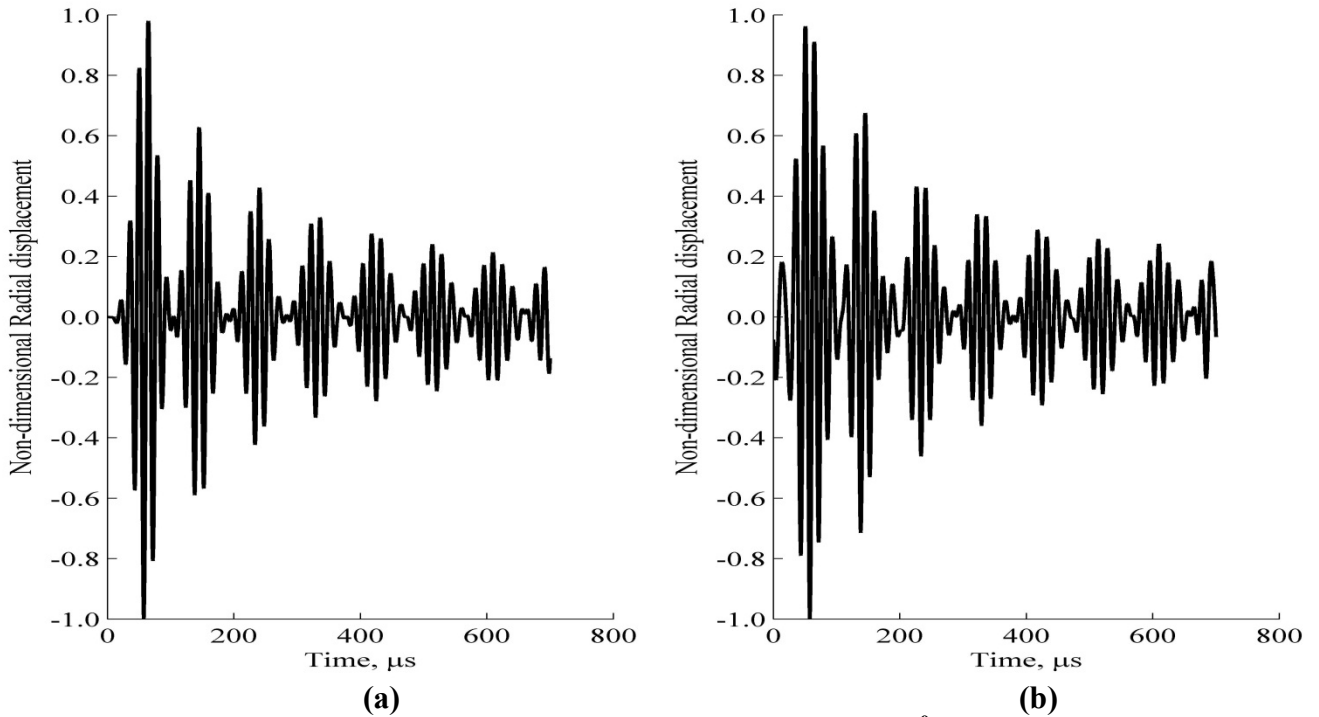


Figure 4.6. Showing (a) the idealized time history predicted at $\theta=0^0$ and axial offset, $z = 5.1H$ and (b) corresponding history after eliminating the effect of imperfect measurement chain.

A comparison of Figures 4.6 (a) and (b) reveals that data leakage is noticeable from the initial non-causality of the signal as well as the non-periodicity of the history. Therefore, time windowing is required. Non-causal responses are merely undesirable numerical artefacts.

Non-causality arising from a wave's propagation makes it impossible to accurately compute its time of flight, a duration which is frequently used to characterize or detect defects [13].

4.6 Updating idealized cylinder's response to incorporate the effect of measurement chain by including an exponential window to eliminate data leakage

Input and output histories are assumed to be periodic or time limited when utilizing the Discrete Fourier Transform (DFT). If these assumptions do not hold, a window having an exponential time decay is usually introduced for a transient history. Even so, it is well known that these windows' bias errors may influence the estimated parameters [59]. Examples of representative windows are illustrated in Figure 4.7. To eliminate the data leakage seen in Figure 4.6 (b), different windows such as the Hanning, Hamming, Boxcars and Exponential window have been tried but the exponential window is found to be more realistic [53]. However, an exponential window artificially increases the effective damping of the structure (e.g. a pipe) of interest.

4.7 Application of exponential window to alleviate leakage

A transient signal is taken to start at time zero, after which it rises to a maximum value and decays eventually to zero before the measurement time window ends. See for instance, Figure 4.6 (a). The DFT computation assumes that the transient signal is periodic in each data block so that the signal repeats over and over again [59, 60]. Data leakage results in a signal's energy being smeared over a wider frequency range in the FFT than is truly the situation. Consequently, a data processing window is applied in the time domain by multiplying the measured signal $y(t)$, by a given time varying function, $w(t)$. A commonly used window function for a transient signal is one which decays

exponentially over time. The resulting operation can be expressed mathematically as [59]:

$$y'(t) = w(t)y(t) \quad (4.7)$$

where,

$y'(t)$ = modified time history (windowed)

$w(t)$ = window

$y(t)$ = original time history

The window is described by the general form:

$$w(t) = e^{-(t/\tau)} = e^{-\sigma_0 t} \quad (4.8)$$

where τ and σ_0 is a time constant and decay rate, respectively. When the exponential window is applied to a signal, the signal's amplitude is attenuated exponentially from unity to an arbitrarily selected value such as 0.1, as shown in Figure 4.7. The end value is a function of the window's time constant, τ , and the total duration of the signal, T . In order to compute the damping, σ_0 , which is effectively added, T must be calculated from the [59].

$$\Delta f = \frac{1}{T} \quad (4.9)$$

where Δf is the frequency resolution measured in Hz. Then σ_0 can be determined from:

$$\sigma_0 = \frac{-\ln[w(T)]}{T} \quad (4.10)$$

where $w(T)$ is the value of the exponential window at the end of the signal.

Illustrative examples of the effect of different σ_0 are presented in Table 4.1. Also, the

time varying effect of various dampings is presented over a period of 700 μs in Figure 4.7.

Table 4.1 Effect of damping on the exponential window.

	Effective damping	σ_0 (rad/s)
1	0.05	4279.62
2	0.10	3289.41
3	0.15	2710.17
4	0.20	2299.20
5	0.25	1980.42

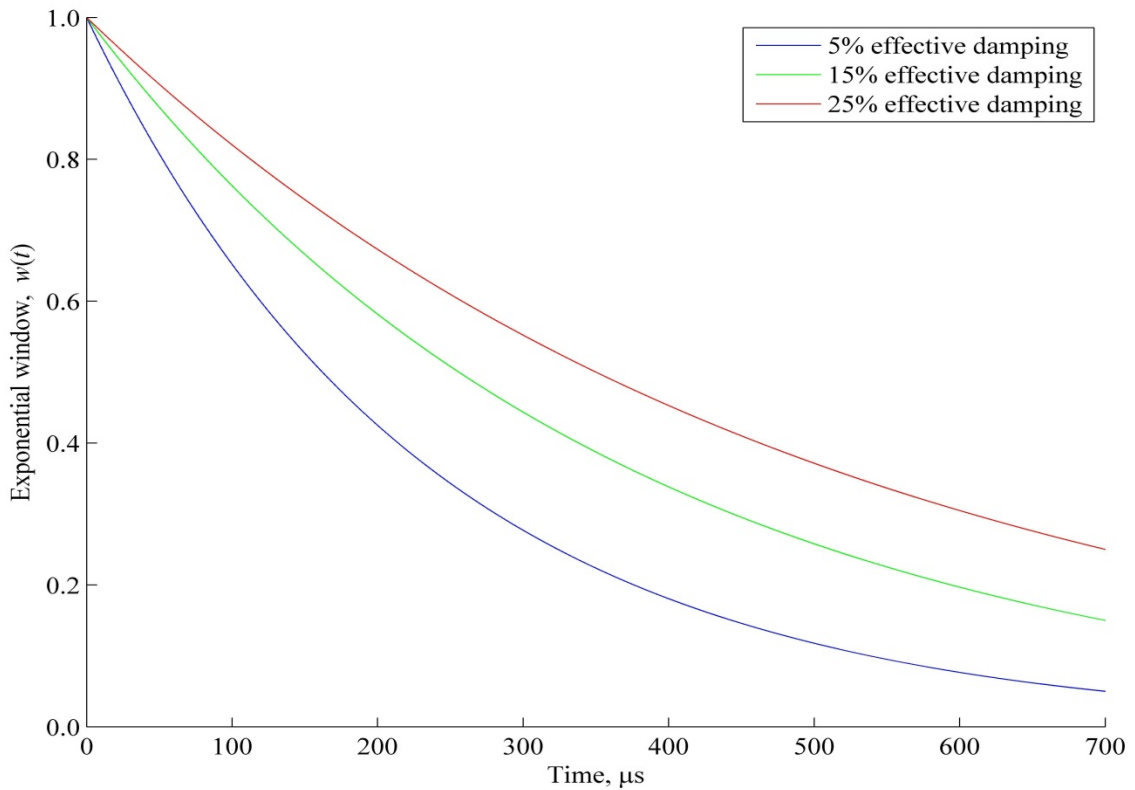


Figure 4.7. Exponential window applied with various effective dampings to the input signal and output response.

Windows work by weighting the start and end of a sample to zero whilst simultaneously increasing the amplitude of the signal at the center of these two instants in order to maintain the signal's time averaged amplitude.

4.8 Reconstructing time histories by applying an exponential window.

Having investigated the effect of data leakage and identified an appropriate time window, Figure 4.9 (b) shows the ensuing time histories. They were obtained by first multiplying the time histories of Figure 4.4 (b), which incorporate the effect of the measurement chain, with the exponential decay function presented in Figure 4.7 and subsequently taking the Discrete Fourier Transform (DFT) described in Chapter 3. The result is convolved with the inverse of the frequency response function of the measurement chain, $H_m^{-1}(\omega)$, by carrying out point-by-point corresponding point multiplication. The adopted linear interpolation scheme considers only the frequency content between 35 kHz and 107 kHz inclusively. Then the Inverse Discrete Fourier Transform (IDFT) is performed on the output to return to the time domain. The final output response is divided by the exponential decay window to compensate for the initial multiplication.

Figure 4.9 (b) presents the time histories obtained when the exponential window with $\sigma_0 = 0.05$ is applied. This procedure is illustrated in Figure 4.8. It is expressed mathematically by equations (4.11) and (4.12).

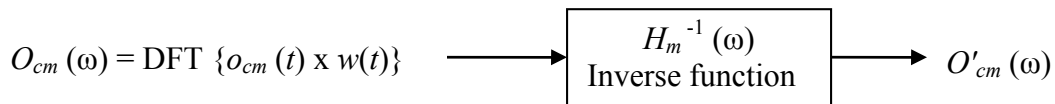


Figure 4.8. Block diagram illustrating the application of inverse function on the convoluted DFT and exponential window.

Mathematically:

$$\text{DFT} \{o_{cm}(t) \times w(t)\} H_m^{-1}(\omega) = O'_{cm}(\omega) \quad (4.11)$$

Taking the Inverse Discrete Fourier Transform and subsequently eliminating the exponential window's effect, gives,

$$IDFT\{O'_{cm}(\omega)\}/w(t) = o'_{cm}(t) \quad (4.12)$$

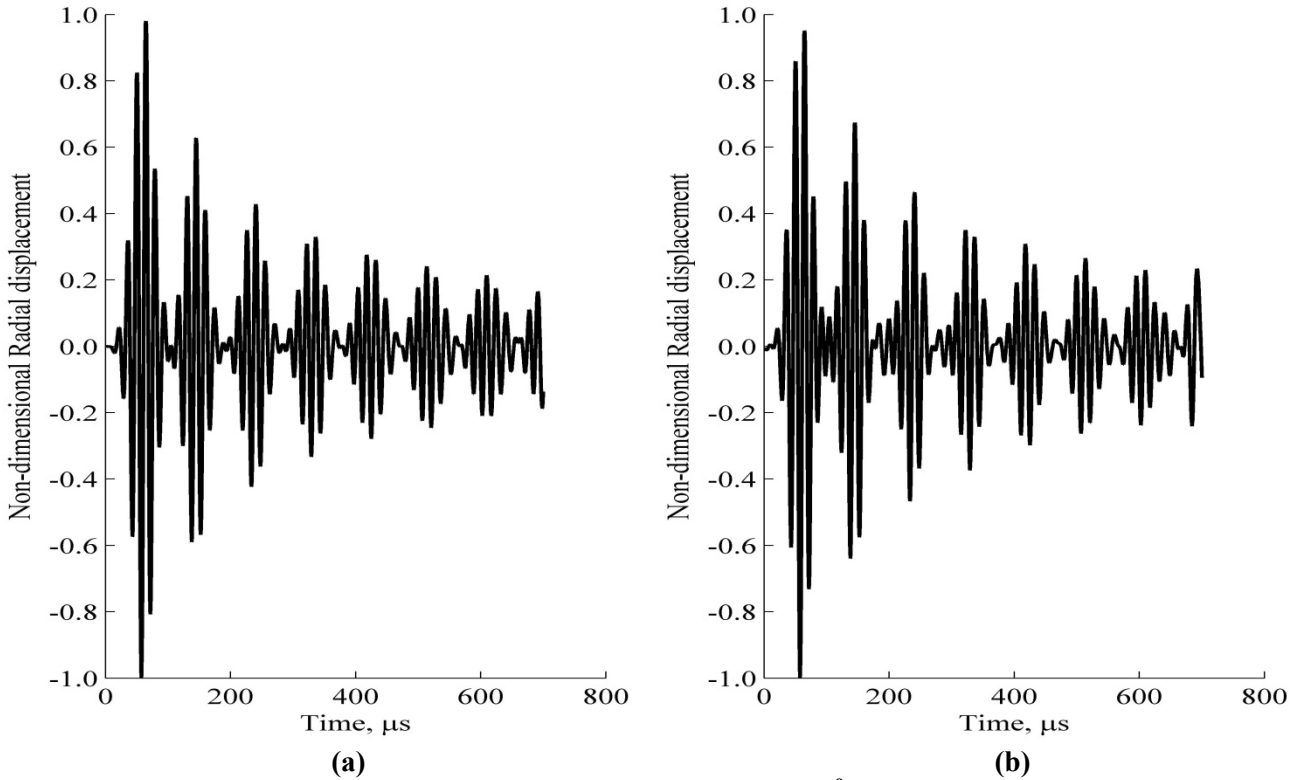


Figure 4.9. Showing (a) idealized time history predicted at $\theta=0^0$ and axial offset, $z = 5.1H$, and (b) corresponding history recovered with an exponential window having 15% damping.

The effect of applying the exponential window to ameliorate data leakage is seen by comparing of Figures 4.6 (b) and 4.9 (b). Clearly the effect of non-causality at the start of the history given in Figure 4.6(b) has been ameliorated in Figure 4.9(b). Furthermore, Figures 4.9 (a) and (b) shows that the ideal time history is comparable to the history from which data leakage has been ameliorated. The small difference observed at the start of Figure 4.9(b), however, is due to the frequency content which has not been considered when taking the DFT. The auto and cross correlations will be considered next to confirm this observation.

4.9 Autocorrelation of the predicted response from SAFE and its “cross correlation” with itself.

Cross correlation is used to further improve the accuracy of the predicted signal. This procedure is found to be useful because it shows the “closeness of fit” between two signals. Here, the reliability of the exponential window with 5% effective damping is investigated still Figure 4.9 (b) shows the measured response obtained after ameliorating the effect of the measurement chain and data leakage by employing an exponential window with 5% damping. To ascertain the most appropriate damping, a cross correlation approach is implemented. As a reference, Figure 4.10 gives the autocorrelation of the idealized cylinder predicted response at $\theta = 0$ and $z = 5.1H$ without incorporating the measurement chain’s effect. On the other hand, Figure 4.11, shows this history in comparison to its cross correlation with the predicted response incorporating and subsequently taking out the effect of the measurement chain. The effective damping of the window is varied between 5% and 25%.

4.10 Cross correlation coefficient and time domain correspondence

4.10.1 Theoretical derivation of cross correlation coefficients

A cross correlation is a well-known method of detecting periodicities which are common to two signals. The following equation is used to calculate the cross correlation coefficient (r_{xy}) of two displacement time histories, $x(t)$ and $y(t)$. Each history is discretized at N equally spaced, temporal data points [61, 62]. Hence

$$r_{xy} = \frac{c_{xy}(\tau)}{\sqrt{c_{xx}(0)c_{yy}(0)}} \quad (4.13)$$

where

$$c_{xy}(\tau) = \begin{cases} N-k \sum_{t=1}^{N-k} (x_t - \bar{x})(y_{t+k} - \bar{y}) + \sum_{t=N-k+1}^N (x_t - \bar{x})(y_{t-N+k} - \bar{y}) & \tau = 1, 2, \dots, N \\ \sum_{t=1}^N (x_t - \bar{x})(y_t - \bar{y}) & \tau = 0 \end{cases} \quad (4.14)$$

Moreover

$$c_{xx}(0) = \sum_{t=1}^N (x_t - \bar{x})^2$$

$$c_{yy}(0) = \sum_{t=1}^N (y_t - \bar{y})^2$$

The τ in Equations (4.13) and (4.14) indicates a time shift of one signal with respect to another signal. Consequently $\tau = 0$ corresponds to the case when the two signals are synchronized [62]. The normalised value of r_{xy} lies in the range, $-1 \leq r_{xy} \leq 1$. A value of, $r_{xy} = 1$ indicates a perfectly linear relationship, between the variables $x(t)$ and $y(t)$, with a positive slope (i.e., increasing $x(t)$ gives a larger in increasing $y(t)$ amplitude). Similarly, $r_{xy} = -1$ indicates a perfectly linear relationship with negative slope. On the other hand, $r_{xy} = 0$ indicates that there is no linear correlation between the variables. Even if there is no correlation, it is unlikely that r_{xy} will be exactly zero due to noise when $x(t)$ and $y(t)$ are measured [63].

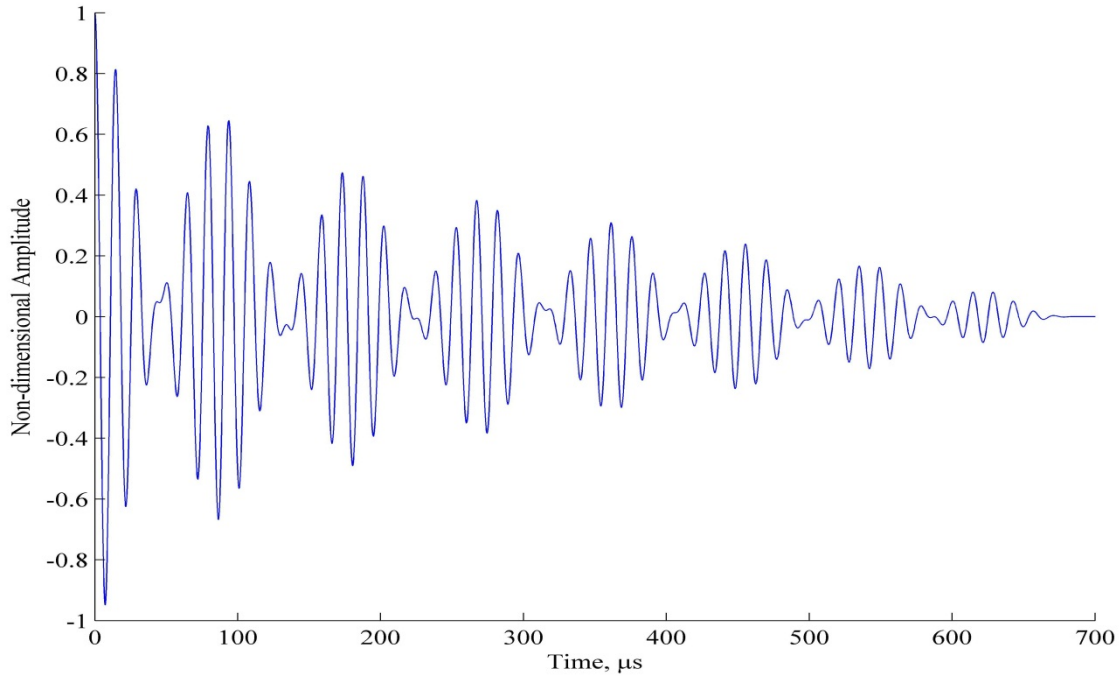


Figure 4.10. Autocorrelation of prediction at circumferential offset, $\theta=0$ and axial offset, $z = 5.1H$.

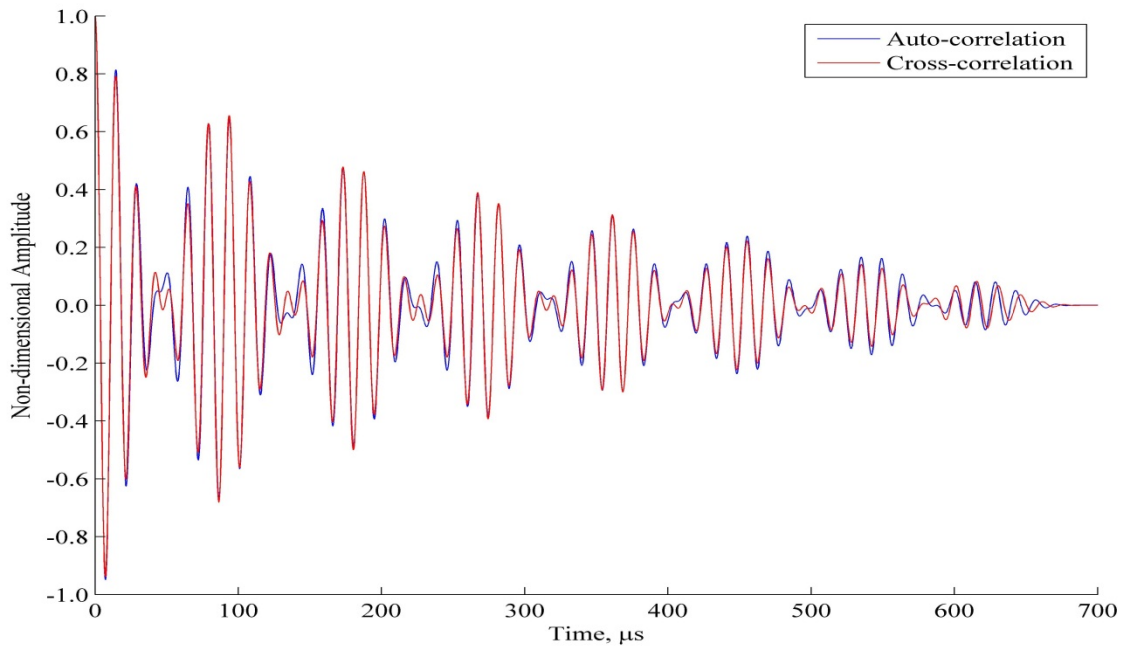


Figure 4.11. Relationship between the autocorrelation of the prediction and “cross correlation” with the predicted response involving 15% damping.

A comparison of the cross correlations given in Table 4.2 for various damping percentages indicates that the agreement between the auto and cross correlations improves marginally as the damping is increased in steps of 5% from 5% to 25%. The closest agreement is found to occur when the damping is 15%.

Table 4.2. Comparison of cut-off frequencies of predicted response from SAFE and those obtained from the inverse procedure.

Case #	Effective damping, %	Cut off frequencies, kHz			% frequency difference, Δf		
		F(10,1)	F(11,1)	F(12,1)	F(10,1)	F(11,1)	F(12,1)
1	5	62.352	72.996	84.054	0.090	0.025	0.050
2	15	62.345	72.968	84.019	0.078	0.014	0.008
3	25	62.331	72.960	83.977	0.056	0.025	0.042
	Computer prediction for idealized cylinder without measurement chain	62.273	73.049	84.085	0.037	0.097	0.087
	Exact cut-off frequencies	62.296	72.978	84.012			

$$\% \text{ frequency difference, } \Delta f = \frac{|\text{Exact frequency} - \text{Predicted frequency}|}{\text{Exact frequency}} \times 100\% \quad (4.15)$$

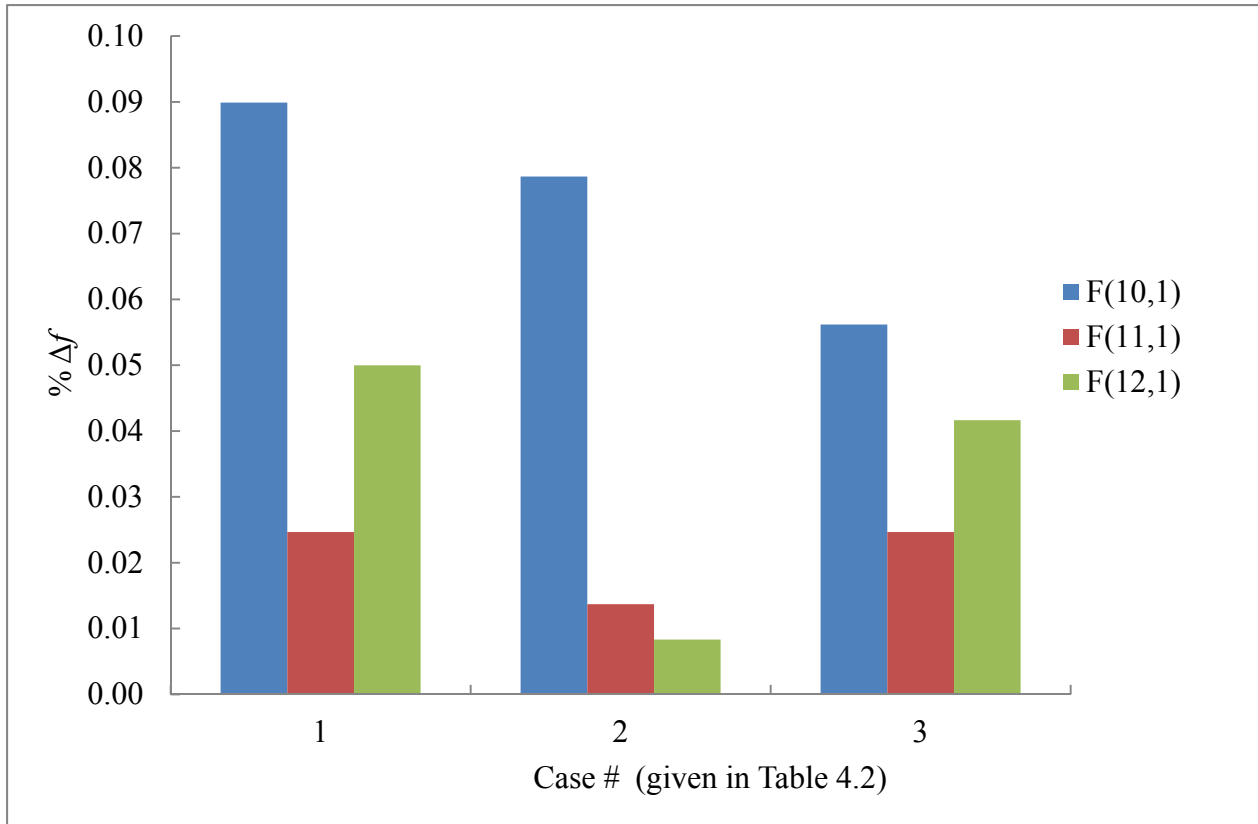


Figure 4.12. Histogram showing the percentage difference of various percentage dampings for the F(10,1), F(11,1) and F(12,1) for cut-off frequencies.

Table 4.2 (and Figure 4.12) shows that the percentage differences between the exact cut-off frequencies obtained directly from SAFE and those found from the inverse procedure of section 4.5 are acceptably low. On the other hand, Figure 4.12 shows that 15% damping is a reasonable overall compromise because the percentage differences in the cut-off frequencies are clearly smallest for all the F(10,1) mode. The procedure to refine the extracted cut-off frequencies from the DFT is discussed further in the next chapter.

CHAPTER 5

EXTRACTING ACCURATE CUT-OFF FREQUENCIES OF AN UNBLEMISHED PIPE'S RADIAL DISPLACEMENT HISTORY

5.1 Preamble

Laboratory experience from previous and the present work suggests that a measured time history may be corrupted by an imperfect measurement chain. This corruption is important when measuring at least three cut-off frequencies to find pipe material and dimensional properties [49]. The pipe is assumed to be homogeneous and isotropic. In addition, the post processing of the experimental data is required to ameliorate the chain's imperfect behaviour. The procedure to remove the varying behaviour in frequency of the instrumentation chain has been developed and implemented in Chapter 4. The result shows that it is unnecessary to have an ideal frequency behaviour of the transducer and supporting electronics equipment because this behaviour can be removed with post processing. After post processing, cut-off frequencies can be extracted by finding the DFT and a curve-fit of the processed time history. Three higher flexural modes were selected, i.e., $F(10, 1)$, $F(11,1)$ and $F(12,1)$, for the unblemished pipe. These particular modes were chosen for the investigation because flexural modes in reflected waves from defects have been found to be detectable and also they are within the neighbourhood of the currently available equipment's centre frequency around 70 kHz [50]. However, somewhat lower or higher flexural modes can be assessed by slightly changing this centre frequency. A finite duration time window is introduced to truncate a measured response history because a real pipe does not have the infinite length assumed computationally. This window is incorporated to exclude reflections from the ends of a finite lengthed pipe. The resulting time history, however, is much too short so that a conventional DFT

gives about a 1 kHz frequency resolution which is significantly broader than required [49]. One way of resolving this problem is by using a global optimization technique. It is found in this work, on the other hand, that a curve fitting procedure provides a better estimate compared with global optimisation searches like simulated annealing and a pattern search. Improved estimates from the curve fitting procedure were obtained by using the cross-correlation between the measured and fitted responses. This approach was noticeably better than one based upon Etta max.

5.2 Method of choosing an appropriate cut-off frequency from a measured time history.

The Pure Adaptive Search (PAS) algorithm [64] for global optimization yields a sequence of points, each of which is distributed uniformly in the level set corresponding to its predecessor. This algorithm has the highly desirable property of solving a large class of global optimization problems by using a number of iterations that increases linearly, at most, with the dimension of the problem. Unfortunately, PAS is mostly of theoretical interest due to the difficulty of generating, in each iteration, a point distributed uniformly in the improving feasible region [64]. Simulated Annealing (SA) is one of the most applicable metaheuristics in optimization. One of the most powerful features of SA is its ability of escaping from being trapped in local minima by accepting, especially in the earlier stages of the search up-hill, moves which are chosen through a probabilistic procedure. However, implementing SA on the continuous, constrained optimization problem is still very limited in comparison with metaheuristics like Evolutionary Algorithms (EAs). Several SA approaches have been proposed for constrained global optimization problems [65]. Stochastic methods for global optimizations include, for example, a sequential random search, pure adaptive search (PAS) and various

evolutionary methods like simulated annealing (SA) and generic algorithms (GAs) [66, 67]. They were used even though a priori knowledge is not needed. A comparison of the results from simulated annealing, pattern search and the straight forward curve-fitting procedures are given in Table 5.1. It can be seen from this table that the curve-fitting method produced the best estimates of the cut-off frequencies which are known exactly, a priori, in this case. They could be found from a purely forward numerical simulation employing known material and dimensional properties of the pipe. However, additional “improvement” is needed for this latter approach to work effectively. The initial approximation from a DFT may be required for a curve fitting approach to work effectively. The procedure for its proper implementation is discussed next.

To select a suitable time window, it is necessary to consider several factors as the “best” result from the curve fitting technique depends upon an appropriate selection of a time window. The following steps are adopted to achieve this objective.

1. The initial arrival of the signal is estimated by finding the first instant that the absolute value of the signal is larger than the noise level. It is about 50 μs .
2. The transducer’s “ring down” is found empirically to be about 175 μs . The ring down behavior is illustrated in Figure 3.12.
3. The excitation’s duration is about 100 μs .

A typical experimental time history, which has not been post-processed, is shown in Figures 5.1. It is assumed in the computations for the unblemished pipe that its length is infinite. In practice, however, a real pipe has a finite length. Therefore, for the two set of the data to be compatible, the end reflections from a finite lengthed (real) pipe need to be

time gated out of a measured response. The result of this procedure is illustrated in Figures 5.1 and 5.2.

Table 5.1 Comparisons of the cut-off frequencies produced by curve fitting, simulated annealing and a pattern search.

Mode	Exact kHz	DFT, kHz	Curve Fit, kHz	SA, kHz	PS, kHz	Δ DFT, Hz	Δ CF, Hz	Δ SA, Hz	Δ PS, Hz
F(10,1)	62.296	62.812	62.368	62.861	62.871	516.28	72.33	565.31	575.00
F(11,1)	72.978	74.233	73.086	74.264	74.275	1254.69	107.68	1286.11	1297.00
F(12,1)	84.012	85.653	84.050	85.650	85.900	1641.10	38.42	1637.55	1888.00

Note:

SA is the Simulated Annealing, PS is the Pattern Search and DFT is the Discrete Fourier Transform.

Δ DFT = absolute difference between corresponding, exact cut-off frequencies and those from a DFT

Δ SA = absolute difference between exact cut off frequencies and simulated annealing

Δ CF = absolute difference between exact cut off frequencies and curve fit

Δ PS = absolute different between exact cut off frequency and pattern search

Therefore confidence in the curve fitting procedure is increased.

5.2.1. Basic procedure for the extraction of cut-off frequencies by curve fitting

Initial experimental information basically takes the form of a measured response time history. Such a history needs to be post-processed by using a suitable time window and a standard DFT to initially approximate the cut-off frequencies. To overcome the inadequate frequency resolution, a global optimization technique is applied straightforwardly to each time history in order to refine the cut-off frequencies [3]. Based on the preliminary information given in Table 5.1, a curve fitting procedure is suitable.

Then the procedure to extract the cut-off frequencies has the following sequential steps according to [49].

1. Select an appropriate time window.
2. Perform a Discrete Fourier Transform (DFT) of the response history occurring in the selected time window to obtain initial estimates for the amplitudes, frequencies, and phase angles at the cut off frequencies.
3. Apply a least-square procedure to minimize

$$\eta(t) = \sum_{i=1}^I \left[u_i - \sum_{j=1}^J e^{-\xi_j(t-\tau_j)} A_j \cos(\omega_j t_i - \phi_j) \right]^2 \quad (5.1)$$

given

$$\eta_{\max} = \max |\eta(t)|. \quad (5.2)$$

In equation (5.1), I is the total number of data points, at a given pipe location, in the radial free response portion of the time window. J is the assumed number of modes contributing to this point's radial displacement, u_i , at the typical i th instant, t_i . For the j th mode, ξ_j represents a viscous like decay. Moreover, τ_j is the time at which the free response begins, whereas A_j , ω_j , and ϕ_j are the modal amplitude, cut-off frequency and phase, respectively [49]. Equation (5.1) essentially curve fits the response time history in order to refine the initially found estimates of A_j , ω_j , and ϕ_j from a DFT. The minimization of equation (5.1) is equivalent to computing a terminated, overall "best" fit of a Fourier series approximation in which the frequency components are related non-harmonically.

The initial estimates are provided conveniently by the DFT of a time history calculated by using MATLAB (2010a). As an initial guideline, the approximations $\xi_j = 0$ and $\tau_j = 200 \mu\text{s}$ have been found to be reasonable for a steel pipe [49].

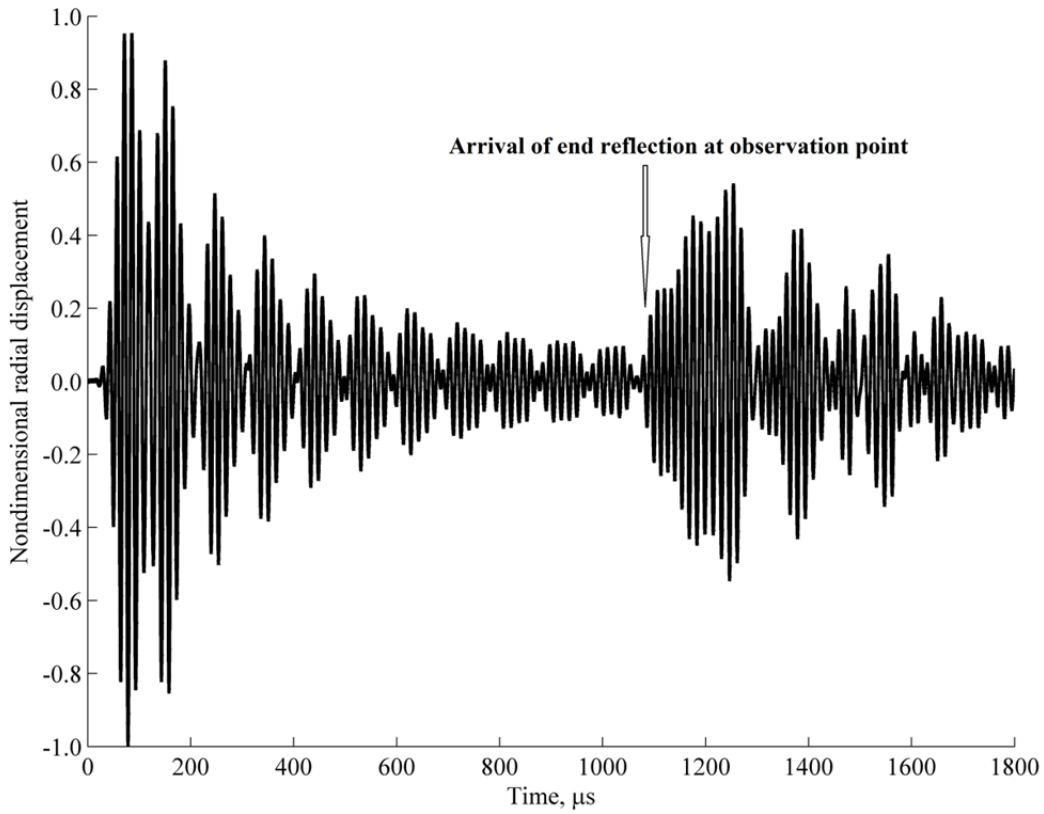


Figure 5.1. Experimental time history showing an end reflection just after 1000 μs .

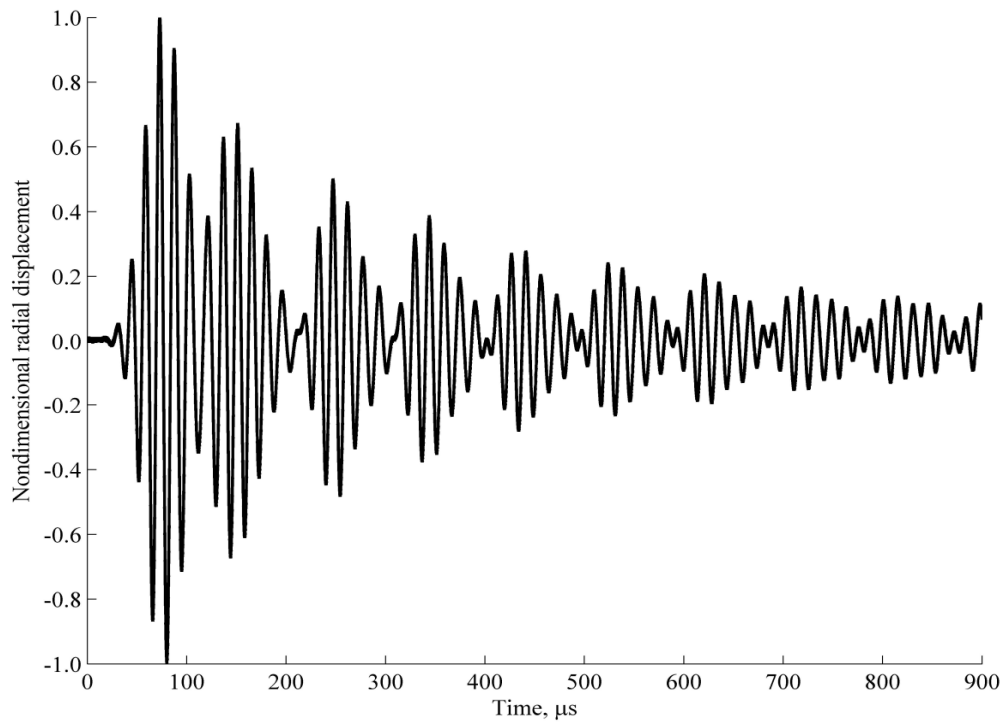


Figure 5.2. History after timing gating out the end reflection from the above experimental data.

5.2.2. Residual and Etta max (η_{\max})

A residual is an estimate of the deviation from an observed response history by the corresponding, approximately curve fitted over the duration of the time window. A temporal, curve fitted response is calculated by taking the time based inverse DFT, after all the unknown modal parameters i.e., amplitude, phase and frequency have been estimated from the frequency based, experimental DFT. Note that Etta max (η_{\max}) is the sum of the squared residuals at the sampling instants over a time window's duration. Mathematically,

$$\text{Etta max } (\eta_{\max}) = \sum(\text{residual})^2 \quad (5.3)$$

Consequently a greater sum of the squared residuals produces a larger Etta max.

Guidelines for choosing an appropriate time window have been given previously. Another approach involves the reassigned pseudo Margenau-Hill time-frequency distribution illustrated in Figure 5.3. It is essentially a wavelet based, short time (and evolving) FFT which is useful for visualizing the temporal evolution of the predominant frequencies of a signal [68]. A typical distribution taken from reference [68] is shown in Figure 5.3. However, this distribution does not emphatically reveal the “best” time window needed to determine cut-off frequencies due to the “smearing” in both time and frequency. Consequently, it is also very difficult to perform an uncertainty analysis [68]. However the challenge of choosing an appropriate time window was mitigated later by using the cross-correlation coefficient of the fitted and corresponding measured responses. This procedure is presented later in section 5.3.2.

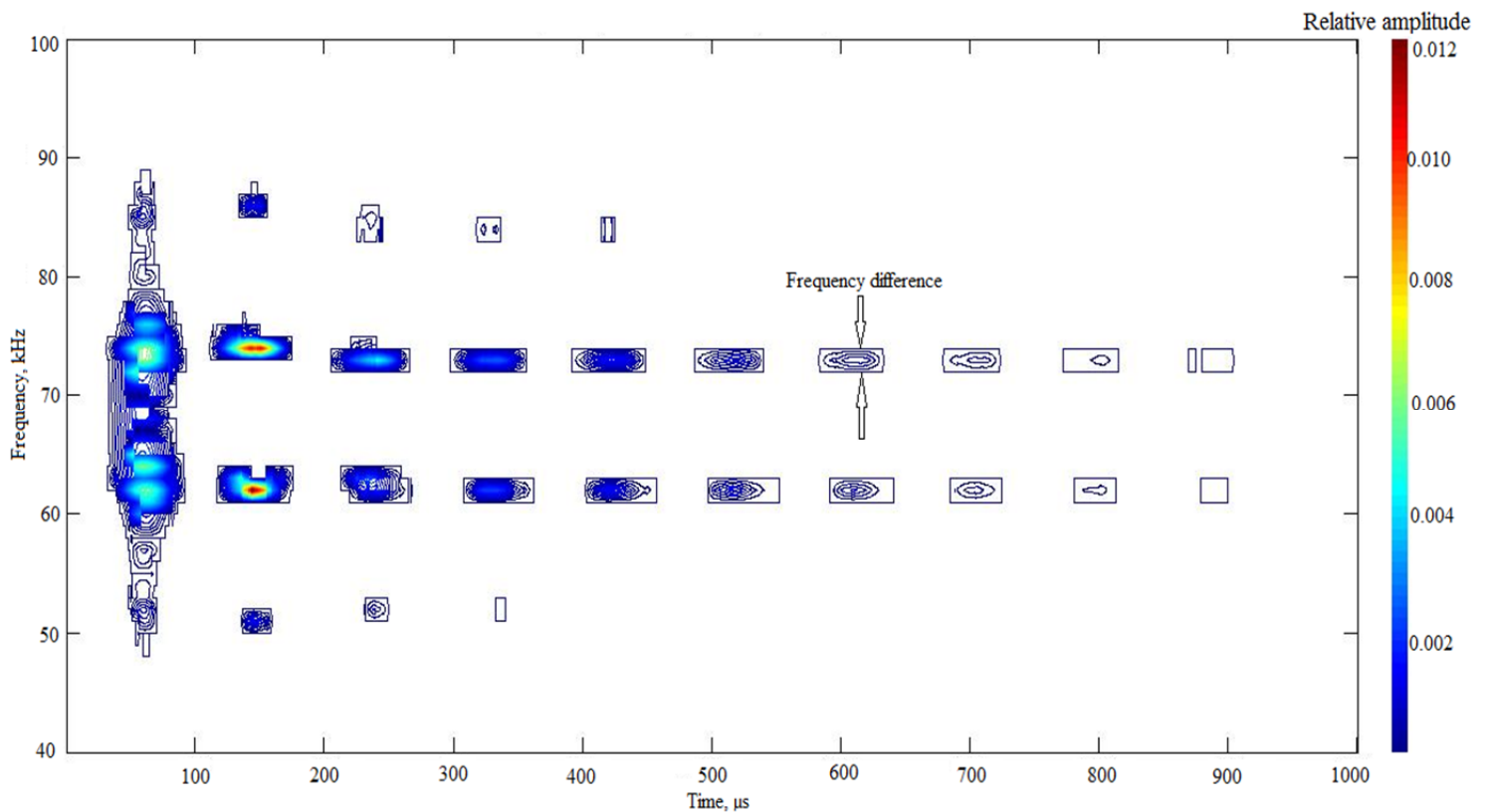


Figure 5.3. Magnitude of the reassigned pseudo Margeneau-Hill time frequency distribution for the predicted radial displacement history given in Figure 5.2. [68]

Figure 5.3 shows the magnitude of the reassigned pseudo Margeneau-Hill time-frequency distribution obtained by He [68] for the unblemished pipe’s predicted radial displacement history given in Figure 5.4. Four cut-off frequencies can be observed around 48 and 90 kHz. The two outside frequencies of 52 kHz and 88 kHz can be seen to die down most quickly as less excitation energy is input at these frequencies. See Figure 5.3 however the time and frequency smearing can be seen clearly.

5.3 Estimating cut-off frequencies by using a cross-correlation approach

A procedure to estimate higher order flexural modes’ cut-off frequencies was described in section 5.2.1. It was seen that an arbitrary time window may produce an ambiguous or unrealistic estimate of the cut-off frequencies. Moreover the use of Etta max was observed to be unreliable. This observation can be also seen from Table 5.2 in which there is no regular and consistent pattern apparent between the Etta max and the

corresponding cut-off frequencies. Consequently, a cross-correlation procedure was developed in section 4.10 [62, 69]. The procedure finds the cross-correlation coefficient between the predicted and curve fitted data, which, in turns, provides the required time window. It was found that a cross-correlation coefficient between a high 0.950 to 0.999 provided reasonable estimates of the cut-off frequencies. Not surprisingly, the illustrative example shown in Figure 5.5 has virtually identical predicted⁶ and curve fitted time histories when their cross-correlation is 0.998.

⁶ Prediction means everything is known so that it can be used to assess, for example an experimental procedure in which an unknown exists.

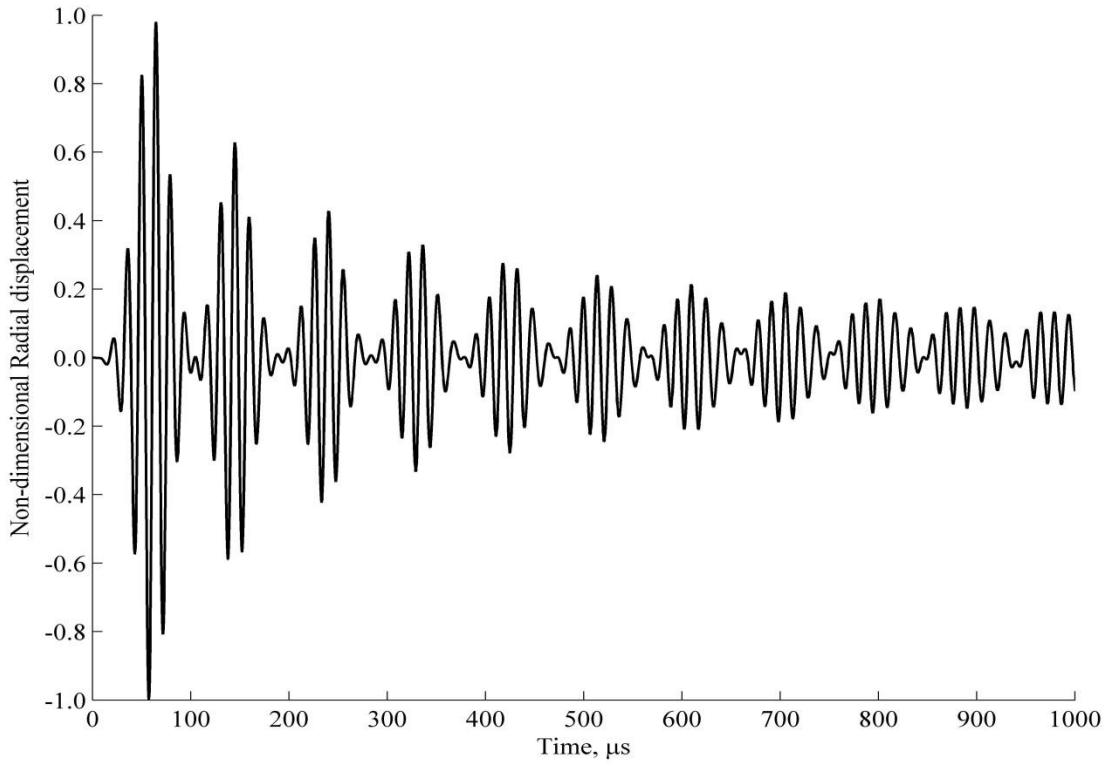


Figure 5.4. Time history predicted at $\theta = 0$, and $z = 5.1H$ before the curve fitting procedure.

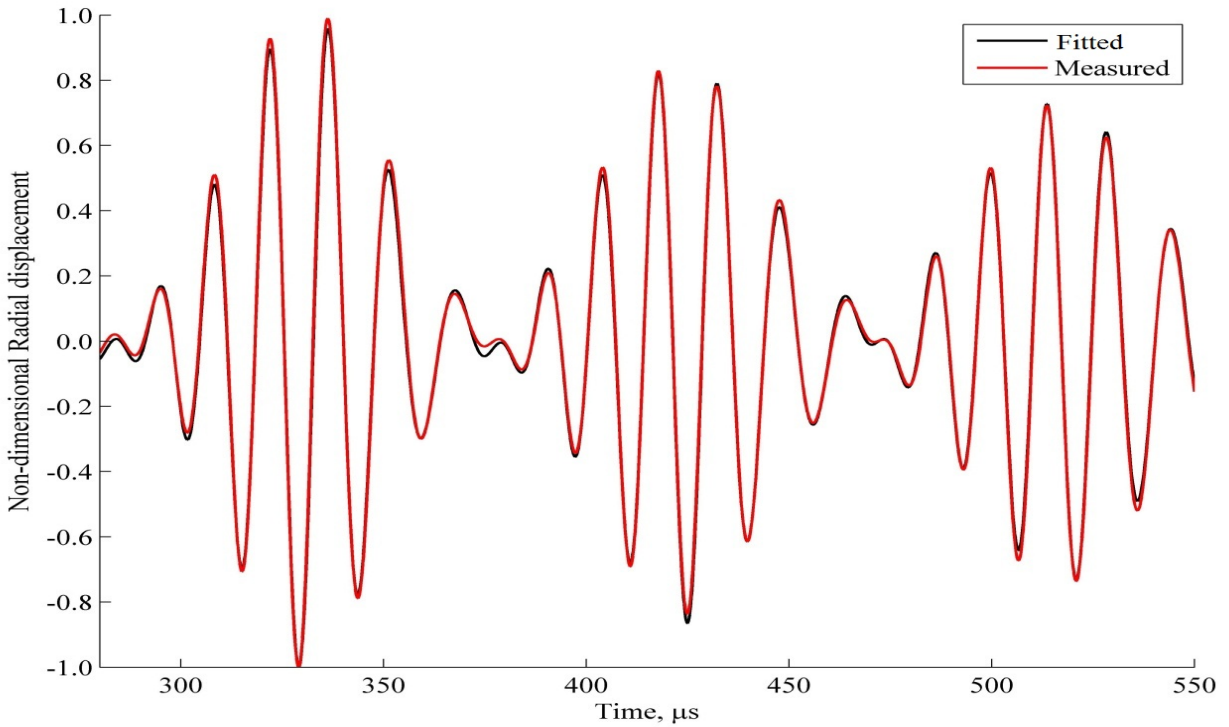


Figure 5.5. Showing the time histories at $\theta = 0$ and $z = 5.1H$, from predicted (black legend) and curve fitting (red legend) having cross-correlation of 0.998.

Table 5.2. Showing the selected cut-off frequencies with the corresponding values of the cross-correlation coefficient, r_{xy} , and Etta max, η_{\max}

Mode	F(10,1), kHz			F(11,1), kHz			F(12,1), kHz				
Case #	DFT	CF	SA	DFT	CF	SA	DFT	CF	SA	r_{xy}	η_{\max}
i	62.812	62.327	62.813	74.233	75.070	74.220	85.653	84.849	85.669	0.771	0.0028
ii	62.461	62.514	62.713	72.455	73.281	72.550	84.947	84.785	84.974	0.974	0.0004
iii	63.936	63.234	63.936	71.928	72.817	71.928	83.916	83.769	83.916	0.941	0.0005
iv	62.188	62.527	62.390	73.293	73.267	73.392	84.398	84.786	84.124	0.992	0.0002
v	63.588	63.287	63.608	72.672	72.795	72.730	84.784	83.930	84.741	0.905	0.0011
vi	63.116	63.250	63.123	73.636	73.169	73.613	84.155	84.754	84.156	0.911	0.0012
vii	60.660	61.100	60.606	74.933	74.988	74.921	85.638	84.766	85.577	0.787	0.0022
viii	63.588	63.227	63.583	72.672	73.001	72.701	84.784	84.761	84.805	0.946	0.0007
ix	62.500	63.196	62.513	72.500	72.837	72.469	85.000	84.686	84.897	0.930	0.0010
x	62.000	62.296	62.900	72.000	72.978	72.800	84.000	84.012	84.743	0.998	0.0053

Note that, in Table 5.2, r_{xy} is the cross-correlation coefficient and η_{\max} is the abbreviation of Etta max. Figure 5.5 has shown very close fit between predicted and curve fitted data. To affirm and develop further confidence in this cross-correlation procedure, each time history was considered on an individual, mode-by-mode basis and compared with the result obtained from the resulting modal superposition. The results, which are given in table 5.4 and 5.5 respectively, show that cross-correlation coefficients provide a good indication of the accuracies of extracted cut-off frequencies. Furthermore, a time window may be chosen at any point within the duration of a time history. A starting point time may be considered at any instant above a 200 μ s according to the steps of section 5.2.1. The minimum time window considered should not less than 250 μ s. This observation can be visualised from the reassigned pseudo Margenau-Hill time frequency distribution presented in Figure 5.3. The initial, broadband behaviour is followed by the “ringing” of each mode that is also indicated in Figure 5.3 by the peaks in the frequency direction narrowing after about 200 μ s [3]. The remaining challenge is to assess which individual

time window provides the “best” estimate of the cut-off frequencies. When will such a time window start and end? The current study showed that at least 250 μ s is the minimum duration of the rectangular time window which produced reasonably accurate cut-off frequencies and ensured that all the modes considered were extracted. Tables 5.4 and 5.5 give the numerical values of the F(10,1), F(11,1) and F(12,1) modes cut-off frequencies when somewhat different material properties were considered. These values are listed in Table 5.3. The conventional and ultrasonically found sets of data were averaged arithmetically and are used further for analysis [9, 49].

Table 5.3 Conventional and ultrasonic measurements with their averaged values for an actual steel pipe [9].

Property	Approach		
	Conventional	Ultrasonic	Average values
Density, ρ , (kg/m ³)	7700 \pm 200	-	-
Outer diameter, D_0 (mm)	88.80 \pm 0.09	-	-
Wall thickness, H (mm)	5.6 \pm 0.1	5.51 \pm 0.17	5.5 \pm 0.1
Mean radius, R (mm)	41.6 \pm 0.1	41.65 \pm 0.13	41.6 \pm 0.1
Thickness to mean radius ratio, (H/R)	0.134 \pm 0.003	0.132 \pm 0.004	0.133 \pm 0.003
Young’s modulus, E (GPa)	202 \pm 6	204 \pm 16	203 \pm 11
Lame’s constant (Shear modulus, μ (G) (GPa)	79 \pm 2	81 \pm 6	80 \pm 4
Lame constant, λ (GPa)	99 \pm 54	89 \pm 41	94 \pm 48
Ratio of Lame constant, (λ/μ)	1.3 \pm 0.7	1.1 \pm 0.5	1.2 \pm 0.6
Poisson ratio, ν	0.28 \pm 0.07	0.27 \pm 0.06	0.28 \pm 0.07

Various time windows were considered that had different starting instants and durations. The rectangular time windows considered were between (280 - 550 μ s), (300 - 850 μ s) and (450 - 850 μ s). These periods corresponded, respectively, to the beginning, middle and end of the predicted response time history. A starting instant and duration of an invariably rectangular time window were 280, 300, 450 μ s and 270, 550, 400 μ s,

respectively. The cross-correlation coefficient between the curve fitted and corresponding predicted response was between 0.959 to 0.999 in all the cases.

Table 5.4 F(10,1) through F(12,1) cut-off frequencies obtained from a time history involving a single mode.

CUT-OFF FREQUENCIES, kHz										
Conventional			Ultrasonic			Average value			Comments	r_{xy}
F(10,1)	F(11,1)	F(12,1)	F(10,1)	F(11,1)	F(12,1)	F(10,1)	F(11,1)	F(12,1)	Time window, μ s	
62.155	72.801	83.850	62.396	73.132	84.291	62.291	72.958	84.059	280 - 550	0.998
62.138	72.763	83.785	62.369	73.113	83.207	62.260	72.910	84.023	300 - 850	0.996
62.136	72.744	83.772	62.361	73.062	84.800	62.253	72.875	84.607	450 - 850	0.997
62.164	72.812	83.808	62.412	73.127	84.197	62.296	72.978	84.012	Exact	

Table 5.5 Cut-off frequencies obtained from a simulated time history which simultaneously involved several modes.

CUT-OFF FREQUENCIES, kHz										
Conventional			Ultrasonic			Average value			Comments	r_{xy}
F(10,1)	F(11,1)	F(12,1)	F(10,1)	F(11,1)	F(12,1)	F(10,1)	F(11,1)	F(12,1)	Time window, μ s	
62.203	72.749	83.884	62.378	73.122	84.200	62.297	73.009	84.037	280 - 550	0.998
62.151	72.758	83.776	62.281	73.044	85.968	62.289	72.903	84.008	300 - 850	0.999
62.150	72.747	82.903	62.392	73.162	84.805	62.376	72.458	84.689	450 - 850	0.999
62.164	72.812	83.808	62.412	73.127	84.197	62.296	72.978	84.012	Exact COF ⁷	

The cut-off frequencies presented in Table 5.4 and 5.5 were obtained from simulated time histories for pipes having properties which had been measured conventionally, ultrasonically and then averaged arithmetically [49]. Data are presented in Table 5.3. Confidence was developed further in the cross-correlation procedure as the extracted cut-off frequencies led invariably to cross-correlation coefficients between 0.996 and 0.999. The higher is the cross-correlation coefficient, the closer are the estimated cut-off frequencies to their “exact” SAFE predictions.

⁷ “Exact COF” are the values of the cut-off frequencies computed by using the Semi Analytical Finite Element (SAFE) method.

This observation is corroborated conveniently in Tables 5.4 and 5.5 in which comparable cross-correlation coefficients between 0.996 and 0.999 are seen. Then the procedure was applied to the experimental time history measured⁸ at a simple axial offset of 5.1H and circumferential offset of 0° from the input transducer. The resulting corresponding cut-off frequencies are shown in Table 5.6 with their uncertainties. Mathematically,

$$\bar{f}_{c_{(10,1)}} = \text{mean cut-off frequency} = \frac{\sum_{i=1}^{n=10} f_c}{n} = 61.40 \text{ kHz} \quad (5.4)$$

$$\sigma_{c_{(10,1)}} = \text{standard deviation of F(10,1) cut-off frequency} = \sqrt{\frac{\sum_{i=1}^n (f_c - \bar{f}_c)^2}{n}} = 0.001 \text{ kHz} \quad (5.5)$$

$$f_{c_{(10,1)}} = 61.40 \pm 0.001 \text{ kHz} \quad (5.6)$$

The same procedure was followed invariably for the other modes presented in Table 5.6.

⁸ What is actually required (everything is not known)

Table 5.6. Cut-off frequencies and uncertainties calculated from experimental data.

Cut-off frequencies, kHz				
Mode	F(10,1)	F(11,1)	F(12,1)	
DFT	61.702	72.340	82.979	r_{xy}
1	61.404	72.094	83.028	0.999
2	61.405	72.095	83.030	0.999
3	61.403	72.093	83.116	0.986
4	61.404	72.093	83.027	0.999
5	61.404	72.096	83.026	0.998
6	61.404	72.098	83.029	0.998
7	61.404	72.100	83.025	0.998
8	61.404	72.090	83.026	0.999
9	61.403	72.093	83.025	0.998
10	61.402	72.103	83.024	0.997
Mean, kHz	61.40	72.10	83.04	0.997
Standard deviation, kHz	0.001	0.004	0.03	0.004
Cut off frequencies, kHz	61.40±0.001	72.10±0.004	83.04±0.03	0.997±0.004

5.4 Discussion of results

Using Etta max to select a time window does not give the most accurate cut-off frequencies. However, it can be used as quick guide. The cross-correlation coefficient procedure gave a better measure of the closeness of the predicted and corresponding curve fitted data. A time window of about 600 μ s with a cross-correlation coefficient between 0.950 and 0.999 is needed to extract quite accurate cut-off frequencies. This situation occurred when single and modal superposition time histories were considered. However, there appeared to be no universally applicable rule for selecting the properties of a time window. If an appropriate time window was chosen carefully, the ensuing cut-off frequencies were close to the values predicted by SAFE. The cut-off frequencies for the F(10,1), F(11,1) and F(12,1) can be found as 61.40 ± 0.01 , 72.10 ± 0.04 and

83.04 ± 0.03 kHz, respectively. The cross-correlation coefficient has been demonstrated to be a reasonable guide. The cross-correlation coefficient procedure provides the later basis for extracting the frequencies of the singularities introduced by an open notch. This topic is discussed further in the next chapter.

CHAPTER 6

EXPERIMENTAL DETECTION OF A NOTCH USING THE FREQUENCY OF A SINGULARITY

6.1 Preamble

Detecting defects is a first step towards assessing the health of a structure. Corrosion in pipework is a major problem, particularly in the oil, gas, chemical and petrochemical industries [70]. Much of the effort in flaw detection in pipes has been concentrated on the generation of a single mode in order to reduce the difficult interpretation when many modes coexist [18, 19, 50]. It is also necessary on the other hand to use a mode which is non-dispersive so that its characteristics are independent of the distance travelled. This restriction may be relaxed, however, if a new technique to compensate for the signal spread caused by dispersion of a long-range, guided wave becomes practical [50]. Moreover, it is difficult and expensive to generate a purely single mode in practice so that a received signal generally contains more than one mode. In addition, the proportion of the different modes is modified by mode conversions at defects [18]. Consequently, a multimode approach using an effectively point force is explored further in this thesis. A Digital Wave Corporation (DWC) B225 ultrasonic transducer is used that can excite different modes within a frequency bandwidth of 35 to 107 kHz centred around 70 kHz. The higher order flexural modes $F(10,1)$, $F(11,1)$ and $F(12,1)$ of an unblemished pipe are excited predominantly in this bandwidth [71, 72, 73]. A preliminary parametric study suggested that the introduction of a notch causes frequency differences from these cut-off frequencies [3]. However, the previous study demonstrated only computationally that the magnitude of the differences depended upon a notch's dimensions. The main advantage of using frequency information may be that it depends upon the blemished pipe's global

structure. Consequently spatial separations may be less important. This aspect is also considered experimentally later. Then, the frequency differences may provide a more easily measured alternative to the reflection coefficient. Reflection coefficients are difficult to estimate because individual modes are often difficult to separate in the time domain when modes are superimposed. It is imperative to confirm, experimentally, the existence of the new singularities and to determine statistically if a frequency shift is measurable and independent of the separation between the two transducers. Therefore, reflections from a free end (when a “notch” encompasses the whole thickness of the pipe) and later, open, approximately rectangular notches having different circumferential extents are considered.

6.2 Definition of non-dimensional parameters

Standard non-dimensional properties employed previously [18, 19] are the axial extent of

the defect expressed as a percentage of a pipe’s wall thickness, $l\% = \frac{l}{H} \times 100$. Similarly,

the non- dimensional defect depth is $d\% = \frac{d}{H} \times 100$ (i.e., depth as a percentage of wall

thickness). The corresponding circumferential extent is $C\% = \frac{c}{2\pi R_m} \times 100$ where R_m is

the mean radius of the pipe. These definitions are used here.

6.3 Relationship between the frequency of a singularity⁹ and the cut-off frequency of an unblemished pipe

Figure 6.1 [3] illustrates a typical relationship between the cut-off frequency, f_c , of an unblemished pipe and the frequency of a nearby singularity, f_s , introduced in the pipe by

⁹ The term “singularity” is used to indicate a displacement response of a guided wave mode that becomes very large and physically behaves similarly to a resonant displacement of a lightly damped, single degree of freedom oscillator [3].

a notch. It can be seen from this figure that a singularity is characterized by the sudden change in amplitude close to but not at a cut-off frequency. The frequency difference between the cut-off frequency, f_c , and the frequency of the corresponding closest singularity, f_s , is expressed mathematically as:

$$\Delta f = f_s - f_c . \quad (6.1)$$

Consequently a negative, Δf , indicates a reduction from the unblemished pipe's cut-off frequency and a positive difference signifies an increase. Only negative reductions have been observed previously [3].

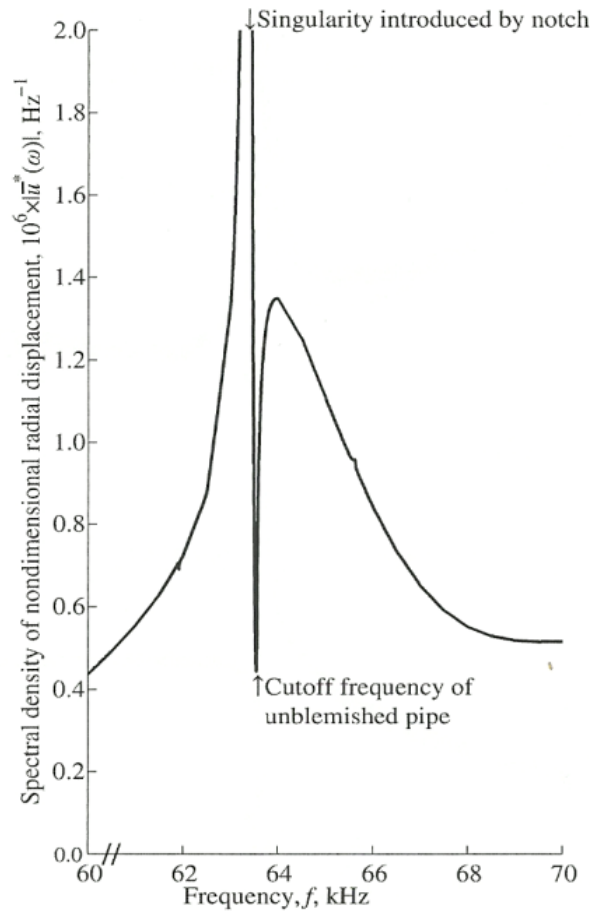


Figure 6.1. Spectral density showing the frequency of a singularity introduced by a notch and the nearest cut-off frequency of the unblemished pipe [3].

6.4 Investigating frequency differences for open, rectangular notches having various circumferential extents.

6.4.1 First stage test (Phase I)

The first stage of the experimental procedure was to confirm that new singularities are truly introduced by a notch. The procedure followed that given section 2.12.2. Preliminary experiments conveniently investigated reflections from a free pipe end and confirmed that frequency differences were observed and were measurable. These test were performed on a 3 inch Nominal Pipe Sizes (NPS) (80mm Diameter Nominal), 5.5mm wall thickness. Several measurements, corresponding to an axial separation between the two transducers of a constant 5.1H, were taken at the free end and the predominant frequencies in a spectral density were extracted by using a rectangular time window from 300 to 900 μ s. These frequencies can be seen from Table 6.1 to be near the higher order flexural, F(10,1), F(11,1) and F(12,1) modes' cut-off frequencies. The experimental set-up for this arrangement is shown in Figure 6.2. The measurement was taken from the free end and was compared with that measured at the axial centre of the pipe with the same axial separation of 5.1H for the two transducers. The radial displacements time histories and corresponding spectral densities for both the free end reflection case and the cut-off frequencies of an unblemished pipe are presented in Figures 6.3 and 6.4.

Table 6.1 Showing differences along the pipe of predominant frequencies

Mode	Singularity Frequencies				
	DFT, kHz	Free end, f_s , kHz	Cut-off frequency, f_c , kHz	Frequency difference, Δf , Hz	Time window, μ s
F(10,1)	61.667	61.772	61.552	220	300-900
F(11,1)	71.667	72.248	72.097	151	
F(12,1)	83.331	82.991	83.069	-78	

Frequency information for a peak was acquired experimentally after signal processing. This post processing involved the capturing of both the amplitude and time of the receiving transducer (from the storage oscilloscope) that was stored subsequently in a MATLAB file. A computer code was developed to visualize this MATLAB file in the time domain in order to, select an appropriate time window to ensure a cross-correlation coefficient from 0.995 to 0.999 between the original and time windowed signals. The Discrete Fourier Transform (DFT) was computed to transform the time domain signal into the frequency domain. Then the frequencies of dominant peak amplitudes were distinguished in the spectral densities. The amplitude, phase and frequencies from the DFT were used as an initial guess to obtain a cut-off frequency, f_c , measured at the middle of the pipe or the frequency of a singularity, f_s , at the free end of the pipe. A frequency closest to a particular cut-off frequency that had a predominant, sharply defined amplitude, was defined as, f_s , the frequency of the corresponding singularity. See equation (6.1). The behaviour of positive Δf is attributed to the stiffness of the pipe. The experiment is well presented in section 6.4.2 and negative Δf were obtained in all the cases considered.

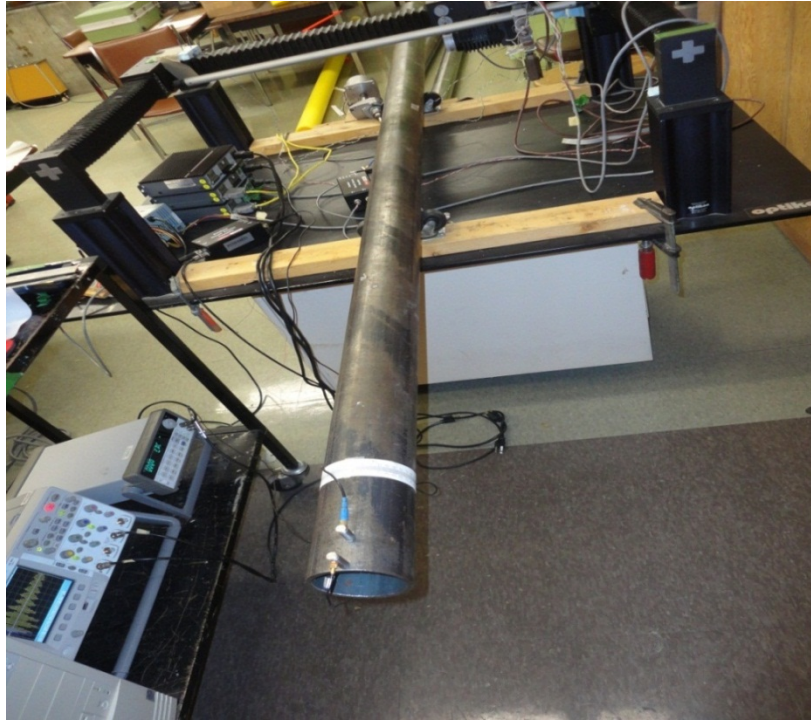


Figure 6.2. Measurement at $z = 5.1H$ and $\theta = 0$ of the reflection coefficient from an unblemished pipe's free end.

The experimental time histories and corresponding spectral densities obtained at the middle of the pipe and free end are shown in Figures 6.3 and 6.4.

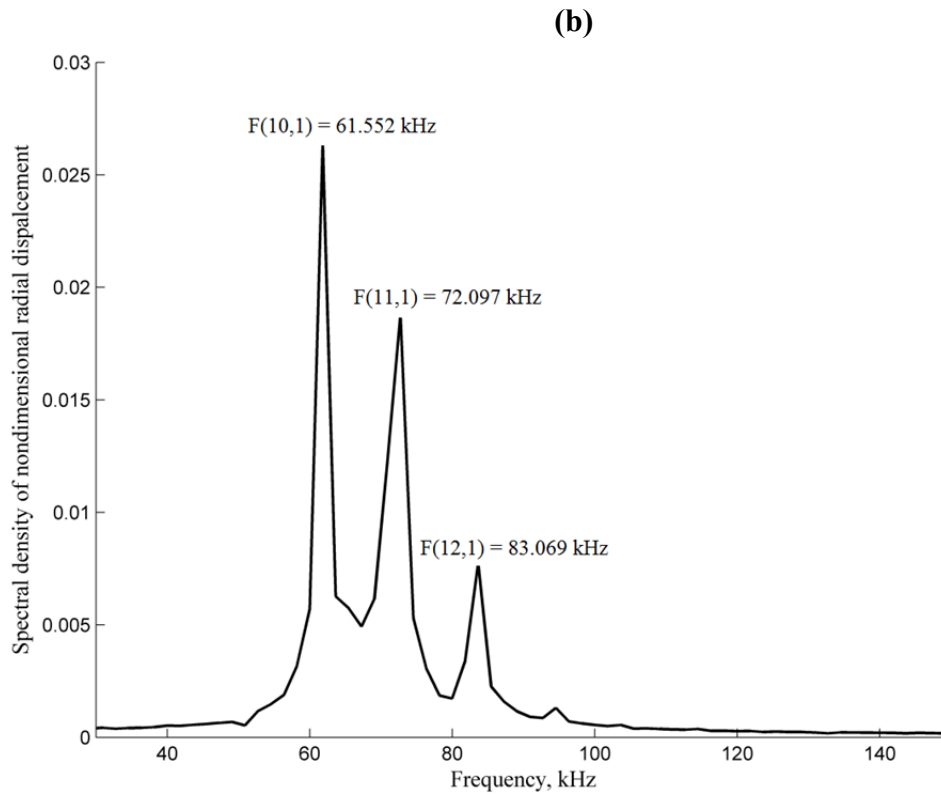
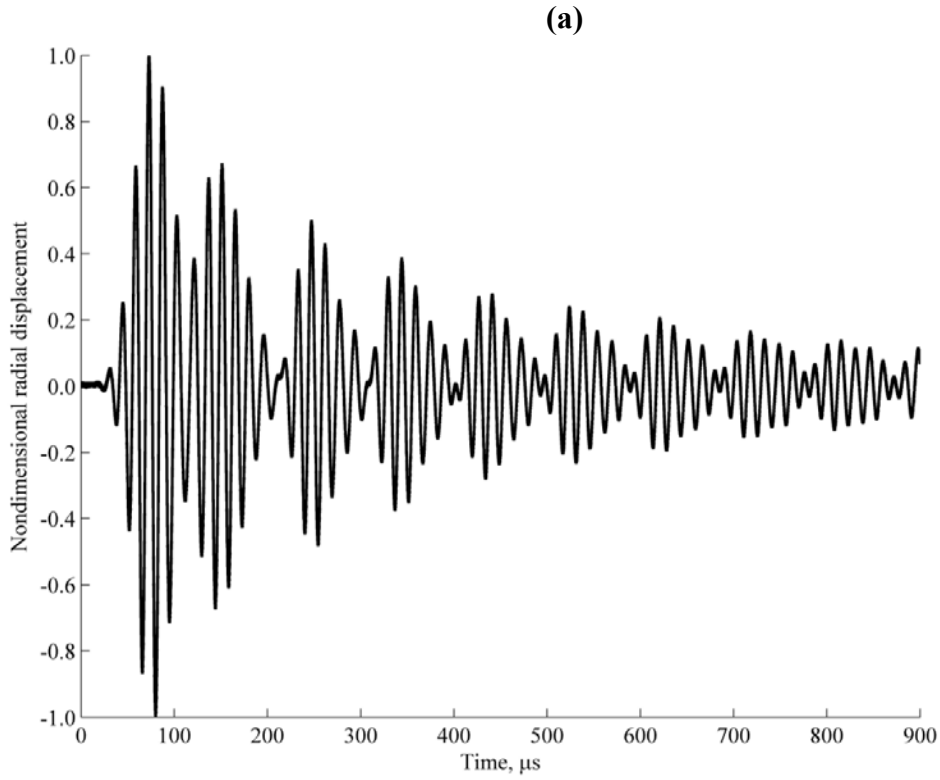


Figure 6.3 (a) Radial displacement time history of unblemished pipe and (b) corresponding spectral density at $z = 5.1H$ and $\theta = 0$.

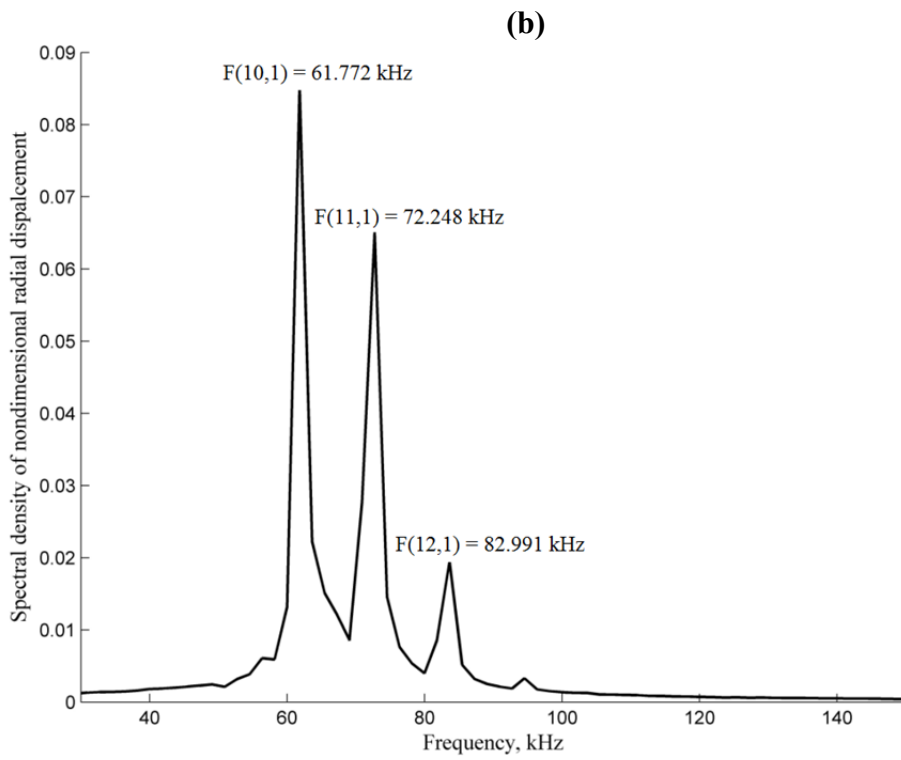
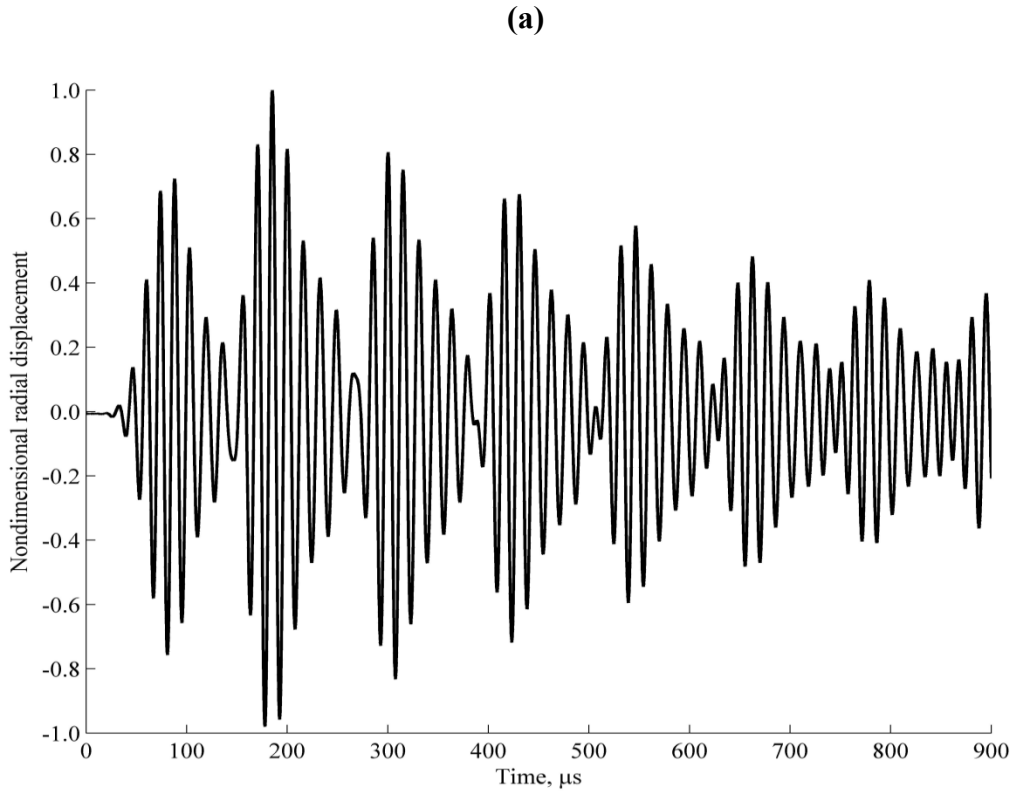


Figure 6.4 (a) Radial displacement's time history measured near the free end and (b) the corresponding spectral density at $z = 5.1H$ and $\theta = 0$.

6.4.2 Second stage test (Phase II)

After carefully measuring the reflection from a free end (as shown in Figure 6.2 and outlined in section 2.12.2), and it was affirmed that frequency shifts from an unblemished pipe's cut-off frequencies were measurable. A blemishless pipe which was different from the one employed earlier, was used to investigate the reliability of the previous experiment. The dimensions of this steel pipe are presented in Table 6.2. Experiments were performed as outlined in section 2.12.2. The pipe was 3.0m long and had a notch machined by hand using a 3.2mm diameter drill. Measurements were taken at 5.1H close to the notch at an axial separation of 5.1H and a circumferential offset of 0° (i.e., a purely axial offset) between the two transducers. See Figure 6.5 for a photographic overview. This experimental set-up was identical to that shown in Figure 2.4 (a) except that a given “notch” was machined into the pipe up to a maximum 80% circumferential extent but with a constant depth 50% of the thickness and 6.4mm axial length. The open notches were made on the pipe at progressively increasing circumferential extents of 11%, 20%, 40%, 60% and 80% of the circumference of the pipe. The depth and axial length of these notches were always approximately 3.5mm (50% of the thickness) and 6.4mm, respectively. Each time history was measured, recorded and post processed to extract the frequencies of the singularities for three modes having frequencies closest to the excitation centre frequency of 70 kHz. i.e., the F(10,1), F(11,1) and F(12,1) modes. The frequency differences, Δf , from the closest cut-off frequencies of these modes are presented in Table 6.3 for different circumferential extents. The representative time history and corresponding spectral density produced by the 80% circumferential notch are shown in Figure 6.6. These data were processed, as discussed in section 6.4.1, to

extract the frequencies of the singularities. Their values are presented in Table 6.3 for the F(10,1), F(11,1) and F(12,1) modes.

Table 6.2 Measured dimensions of the second steel pipe.

Property	Measured value
Thickness, H (mm)	7 ± 1
Mean Radius, R (mm)	54 ± 1
Outer Diameter, D_0 (mm)	115 ± 2
Thickness to Mean Radius Ratio, H/R	0.130 ± 0.004
Pipe's outer circumference ($2\pi R$) (mm)	339.3 ± 0.5
Total length of the pipe (cm)	287 ± 2
Axial length of the pipe, l (mm)	6.4 ± 0.1
Depth of the notch, d (mm)	3.5 ± 0.1

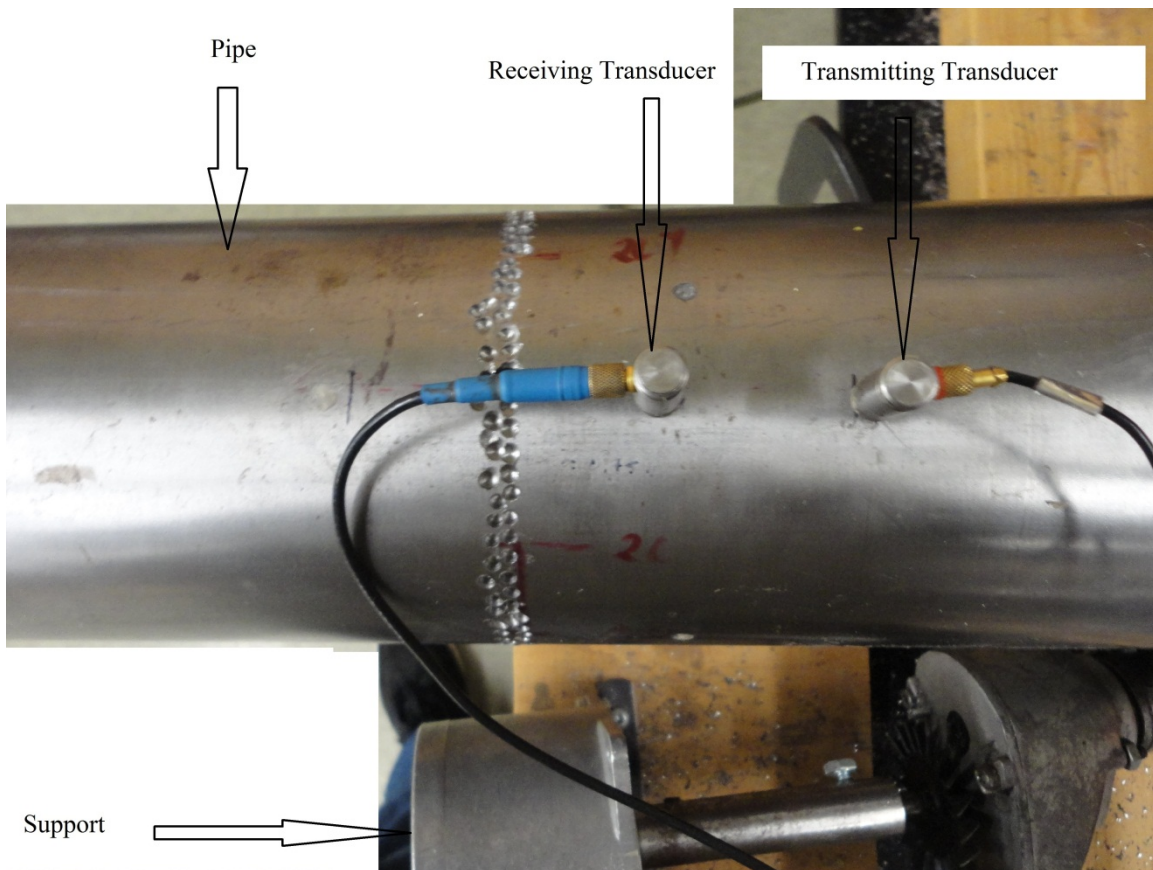


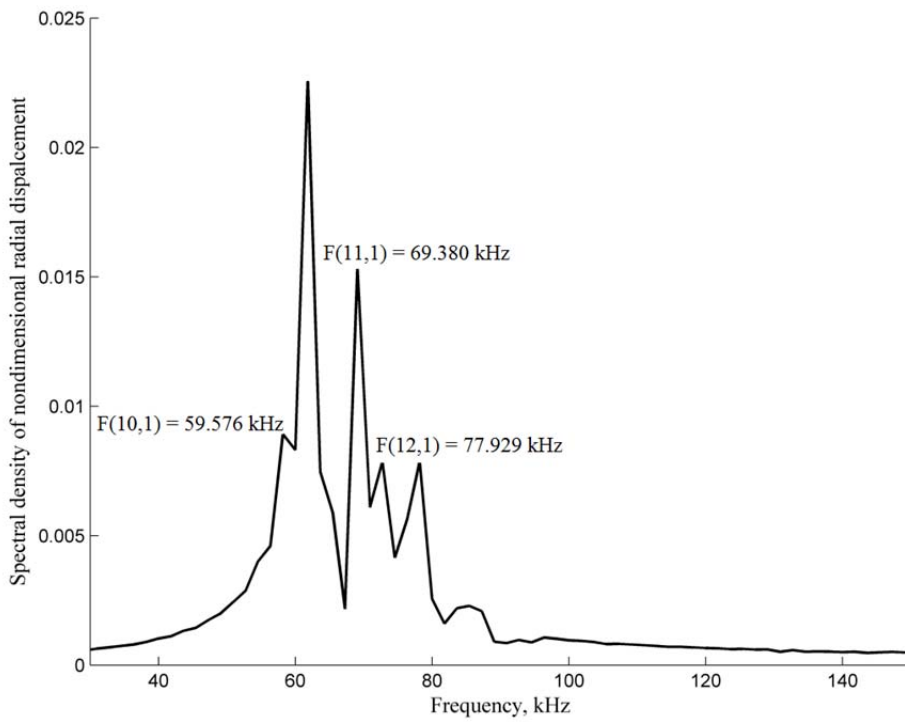
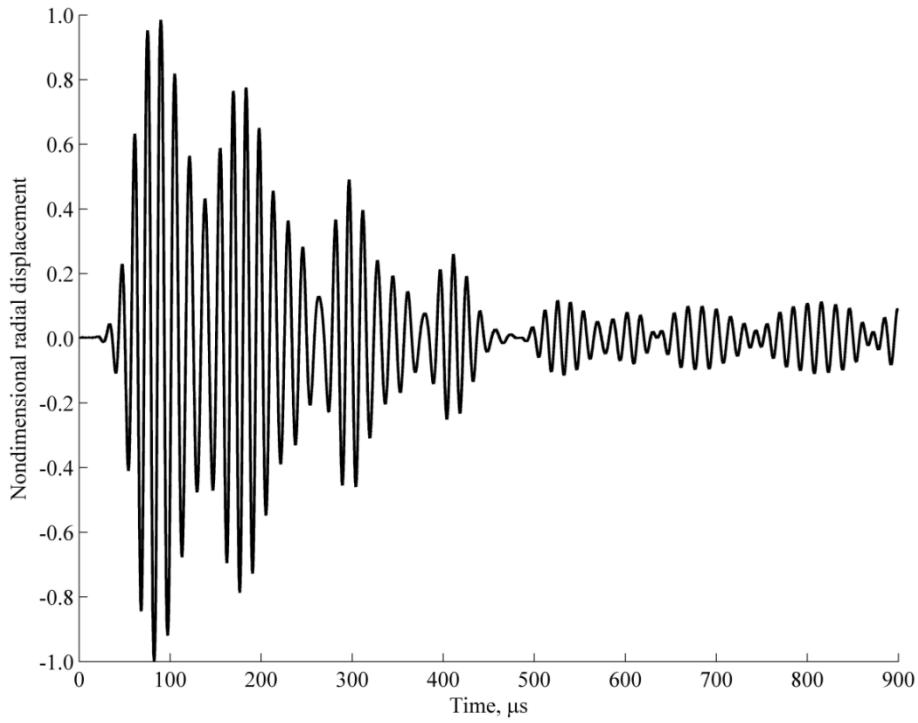
Figure 6.5. Open notch having an 80% circumferential extent at an axial separation of $5.1H$ between the two transducers.

Table 6.3 Showing the frequency difference, Δf , for open notches having different percentage circumferential extents.

	F(10,1) kHz	Δf, kHz	F(11,1) kHz	Δf, kHz	F(12,1) kHz	Δf, kHz
COF of unblemished pipe, kHz	60.896		69.411		78.008	
11% of the pipe's outer circumference	60.780	-0.116	69.195	-0.216	78.471	0.463
20% of the pipe's outer circumference	60.627	-0.269	68.971	-0.440	77.298	-0.710
40% of the pipe's outer circumference	60.465	-0.431	69.067	-0.344	76.575	-1.433
60% of the pipe's outer circumference	60.338	-0.558	69.240	-0.171	77.808	-0.200
80% of the pipe's outer circumference	59.576	-1.320	69.380	-0.061	77.929	-0.079

A Gaussian modulated sine wave was used invariably to generate a pulse signal within a frequency bandwidth of 35 to 107 KHz. The Fourier transform was used to analyse peak frequency differences of the received signal. Results are shown in Figure 6.6 and outlined in Table 6.3. There were indeed some shifts in the peak frequencies to the left with an increase in a notch's circumferential extent (i.e., from 11% to 80%).

(a)



(b)

Figure 6.6. (a) Radial displacement's history for the 80% circumferential notch and (b) the corresponding spectral density.

To assess the likely variation of the measurement at a given circumferential extent of a notch, ten different measurements were taken for the 80% circumferential notch without removing the two transducers. This approach was chosen purposely as a measure of the repeatability. Each measured time history was post processed to extract the predominant frequencies. A time window between 300 and 900 μs was chosen that produced the highest cross-correlation coefficient of 0.950 to 0.999. This time window remained the same throughout. In addition, the axial and circumferential offsets between the two transducers were kept 5.1H and 0° , respectively. The results from the preliminary investigation of the free end reflection are given in Table 6.4 (a). The confirmation of the frequency differences, Δf , between the frequency of a singularity, f_s , and corresponding cut off frequency, f_c , clearly shows that singularities were truly introduced. The Δf , when an 80% circumferential extent of the notch was introduced, is also presented in Table 6.4 (b) for the F(10,1), F(11,1) and F(12,1) modes. The standard deviation and corresponding uncertainty were also evaluated for each mode. For example, the frequency of singularity, f_s , of the free reflection for F(10,1) is 60.470 ± 0.020 kHz. It is important to note that the extraction of accurate cut-off frequencies (using the cross-correlation procedure discussed in Chapter 5) looks very promising and serves as the basis for this study. The results obtained from Figure 6.6 are summarised, after post processing, in Tables 6.4 (a) and (b).

Table 6.4 (a) Measured frequency differences, Δf , for different, higher order flexural modes in the free end case.

	F(10,1) kHz	Δf kHz	F(11,1) kHz	Δf kHz	F(12,1) kHz	Δf kHz	r_{xy}
COF of unblemished Pipe, kHz	60.896		69.411		78.008		0.998
DFT, kHz	60.000		68.889		77.778		
Reflection from free end of the pipe							
1	60.508	-0.388	68.896	-0.515	77.815	-0.193	0.989
2	60.484	-0.412	68.910	-0.501	77.820	-0.188	0.989
3	60.470	-0.426	68.945	-0.466	77.822	-0.186	0.981
4	60.470	-0.426	68.913	-0.498	77.821	-0.188	0.987
5	60.473	-0.423	68.921	-0.490	77.822	-0.186	0.988
6	60.438	-0.458	68.969	-0.442	77.818	-0.190	0.963
7	60.466	-0.430	68.936	-0.475	77.824	-0.185	0.984
8	60.444	-0.452	68.965	-0.446	77.819	-0.189	0.969
9	60.463	-0.433	68.957	-0.454	77.822	-0.186	0.980
10	60.480	-0.416	68.920	-0.492	77.821	-0.187	0.988
Mean, kHz	60.470	-0.426	68.933	-0.478	77.820	-0.188	0.982
Standard deviation, kHz	0.020	0.020	0.025	0.025	0.002	0.002	0.009

Table 6.4 (b) The Δf for the higher order flexural modes F(10,1), F(11,1) and F(12,1) measured for a notch having an 80% circumferential extent.

	F(10,1) kHz	Δf kHz	F(11,1) kHz	Δf kHz	F(12,1) kHz	Δf kHz	r_{xy}
COF of unblemished Pipe, kHz	60.896		69.411		78.008		0.998
DFT, kHz	60.000		68.889		77.778		
Frequency of Singularity							
1	59.583	-1.313	69.380	-0.061	77.947	-0.061	0.991
2	59.569	-1.327	69.380	-0.061	77.889	-0.119	0.989
3	59.588	-1.308	69.384	-0.057	78.020	0.012	0.989
4	59.563	-1.333	69.380	-0.061	77.892	-0.116	0.989
5	59.591	-1.305	69.381	-0.060	77.938	-0.069	0.992
6	59.579	-1.318	69.380	-0.062	77.935	-0.073	0.987
7	59.563	-1.333	69.378	-0.063	77.887	-0.122	0.991
8	59.572	-1.324	69.380	-0.061	77.922	-0.086	0.991
Mean, kHz	59.576	-1.320	69.380	-0.061	77.929	-0.079	0.990
Standard deviation, kHz	0.011	0.011	0.002	0.002	0.044	0.044	0.002

The peak¹⁰ frequency will shift to the left as the circumferential extent increases for different mode. This relates circumferential extents and frequency difference together. Different modes have different sensitivity to circumferential extent. For Table 6.4 (a) at the free end and Table 6.4 (b) when notches were introduced for higher flexural modes, the shifting becomes apparent and is larger for F(10,1) modes when notches were introduced, the magnitude of the frequency difference is larger at F(11,1) at the free end. Therefore, the behaviour of the modes is different for a specify notch geometry. The figures show that a frequency difference shifts to the left as Δf is negative for all the mode considered.

6.5 Statistical analysis of the estimated frequency differences

Statistical tests assume that certain conditions are met. The primary assumptions for the *t*-test involve a population data from which the sample data are drawn are distributed normally. For the two-sample tests, the variances of the populations to be compared are equal, each score (or difference score for the paired *t*-test) must be independent of all other scores [74]. However, if the sample size, *n*, is small (i.e., $n < 30$), the assumption that the population standard deviation can be represented by the sample's standard deviation may not be accurate. In this case, a Student's *t* test is preferable because the assumption of a Gaussian distribution has been shown to be somewhat unreliable [63, 74]. This is confirmed from Figures 6.7 through 6.12, with little or no outliers. Therefore, the *t* distribution is used to determine the uncertainty. Tables 6.4 (a) and (b) show the frequencies of the various modes' singularities and corresponding frequency differences both at the free end and that caused by an open notch having an 80% circumferential

¹⁰ A peak frequency will occur when the excitation line intersects with phase velocity dispersion curve. The frequency at this peak is called the peak frequency.

extent. The illustrative example is considered in sections 6.5.1 and 6.5.2 for both the free end and when a notch was introduced, respectively.

6.5.1 Illustrative example

An error analysis using a t “test” distribution for the measurable frequency shift for the F(10,1) mode is chosen as an illustration. It is summarised in Tables 6.5 (a) and (b) for both the free end reflection and the 80% circumferential notch cases. This same procedure was followed for the F(11,1) and F(12,1) modes to give the data presented in Tables 6.5 (a) and (b).

6.5.1.1 Case A: Frequencies of the singularities for the free end of a pipe.

The procedure has the following sequential steps.

1. Compute the mean of the number of observations, n

$$\bar{f}_{s_{(10,1)}} = \text{Mean frequency value of singularity closest to F(10,1) mode} = \frac{\sum_{i=1}^n f_{s_{(10,1)_i}}}{n} \quad (6.2)$$

$$n, \text{ number of observations} = 10 \quad (6.3)$$

By substituting equation (6.3) and data from Table 6.4 (a) into equation (6.2), it can be found straightforwardly that

$$\bar{f}_{s_{(10,1)}} = 60.470 \text{ kHz} \quad (6.4)$$

2. Compute the sample standard deviation

$\sigma_{s_{(10,1)}}$ = Standard deviation of the estimated frequency value of the singularity closest to

the cut-off frequency of the unblemished pipe's F(10,1) mode

$$\sigma_{s_{(10,1)}} = \left[\frac{\sum (f_{s_{(10,1)_i}} - \bar{f}_{s_{(10,1)}})^2}{n-1} \right]^{0.5} \quad (6.5)$$

By substituting data from Table 6.4 (a) for F(10,1) into equation (6.5),

$$\sigma_{s_{(10,1)}} = 0.020 \text{ kHz} \quad (6.6)$$

3. Compute the standard deviation of the mean

$$\sigma_{m_{(10,1)}} = \text{standard deviation of the mean} = \frac{\sigma_{s_{(10,1)}}}{\sqrt{n}} = 0.006 \text{ kHz} \quad (6.7)$$

4. Compute the confidence deviation

According to [ASME (1998) and ISO 1993], confidence level of 95% is commonly used to determine the random uncertainty interval [63]. Therefore, using t -distribution at 95% confidence interval and degree of freedom equal to 9, the value of $t_{95} = 2.262$ [63, 74].

For a given confidence limit, a value of t can be obtained from [63, 74] for the degree of freedom ν ,

$$\nu = \text{Degrees of freedom} = n - 1 = 9$$

$$\Delta, \text{ confidence deviation} = \frac{t_{95} \sigma_{s_{(10,1)}}}{\sqrt{n}} = t \sigma_{m_{(10,1)}} = 2.262 \times 0.006 = 0.014 \text{ kHz} \quad (6.8)$$

Therefore,

$$f_{s_{(10,1)}} = 60.470 \pm 0.014 \text{ kHz} \quad (6.9)$$

Similarly, for the corresponding frequency difference,

$$\Delta f_{(10,1)} = 0.426 \pm 0.014 \text{ kHz} \quad (6.10)$$

6.5.1.2 Case B: Frequencies of singularities after introducing a notch with an 80% circumferential extent.

The procedure has the following sequential steps

1. Compute the mean of number of observations

$$\bar{f}_{s_{(10,1)}} = \text{Mean frequency value of singularity closest to F(10,1) mode} = \frac{\sum_{i=1}^n f_{s_{(10,1)}_i}}{n} \quad (6.11)$$

$$n, \text{ number of observations} = 8 \quad (6.12)$$

By substituting equation (6.12) and data from Table 6.4(b) into equation (6.11), it can be found straightforwardly that

$$\bar{f}_{s_{(10,1)}} = 59.576 \text{ kHz} \quad (6.13)$$

2. Compute the sample standard deviation

$\sigma_{s_{(10,1)}}$ = Standard deviation of frequency value of singularity closest to F(10,1) mode

$$\sigma_{s_{(10,1)}} = \left[\frac{\sum (f_{s_{(10,1)}_i} - \bar{f}_{s_{(10,1)}})^2}{n-1} \right]^{0.5} \quad (6.14)$$

By substituting data from Table 6.4 (b) for F(10,1) into equation (6.14),

$$\sigma_{s_{(10,1)}} = 0.011 \text{ kHz} \quad (6.15)$$

3. Compute the standard deviation of the mean

$$\sigma_{m_{(10,1)}} = \text{standard deviation of the mean} = \frac{\sigma_{s_{(10,1)}}}{\sqrt{n}} = 0.004 \text{ kHz} \quad (6.16)$$

4. Compute the confidence deviation

Using t -distribution at 95% confidence interval and degree of freedom equal to 7, the value of $t_{95} = 2.365$ [63, 74]. For a given confidence limit, a value of t can be obtained from [63, 74] for the degree of freedom ν ,

$$\nu = \text{Degree of freedom} = n - 1 = 7$$

$$\Delta = \text{confidence deviation} = \frac{t_{95}\sigma_{s(10,1)}}{\sqrt{n}} = t\sigma_{m(10,1)} = 2.365 \times 0.004 = 0.010 \text{ kHz} \quad (6.17)$$

Therefore,

$$f_{s(10,1)} = 59.576 \pm 0.010 \text{ kHz} \quad (6.18)$$

Similarly, for the corresponding frequency difference,

$$\Delta f_{(10,1)} = 1.320 \pm 0.010 \text{ kHz} \quad (6.19)$$

This approach is also applicable to the F (11,1) and F(12,1) modes. The resulting data are summarised more conveniently in Table 6.5 (a) and (b). Despite uncertainty, Δf is measurable at a 95% confidence level. However, no trend is noticed for Δf for an increasing flexural mode number.

Table 6.5 (a) Uncertainty analysis of frequency differences, Δf , for free end reflection relative to F(10,1), F(11,1) and F(12,1) cut-off frequencies.

Mode	F(10,1)	Δf , kHz	F(11,1)	Δf , kHz	F(12,1)	Δf , kHz
Mean frequency of singularity, Mean, kHz	60.470	-0.426	68.933	-0.478	77.820	-0.188
Sample's standard deviation, kHz	0.020	0.020	0.025	0.025	0.0024	0.0024
Sample size (degrees of freedom)	10 (9)	10 (9)	10 (9)	10 (9)	10 (9)	10 (9)
Standard uncertainty, kHz	0.006	0.006	0.007	0.007	0.0008	0.0008
<i>t</i> value @ 95% confidence level	2.262	2.262	2.262	2.262	2.262	2.262
95% confidence level of deviation in sample	0.014	0.014	0.018	0.018	0.002	0.002
95% confidence interval for minimum sample value, kHz	60.456	-0.440	68.915	-0.496	77.819	-0.189
95% confidence interval maximum sample value, kHz	60.484	-0.412	68.951	-0.460	77.822	-0.186

Table 6.5 (b) Uncertainty analysis of frequency differences, Δf , for 80% circumferential notch relative to F(10,1), F(11,1) and F(12,1) cut-off frequencies.

Mode	F(10,1)	Δf , kHz	F(11,1)	Δf , kHz	F(12,1)	Δf , kHz
Mean frequency of singularity, Mean, kHz	59.576	-1.320	69.380	-0.061	77.929	-0.079
Sample's standard deviation, kHz	0.011	0.011	0.0018	0.0018	0.044	0.044
Sample size (degrees of freedom)	8 (7)	8 (7)	8 (7)	8 (7)	8 (7)	8 (7)
Standard uncertainty, kHz	0.0038	0.0038	0.00063	0.00063	0.0155	0.0155
<i>t</i> value @ 95% confidence level	2.365	2.365	2.365	2.365	2.365	2.365
95% confidence level of deviation in sample	0.010	0.010	0.001	0.001	0.037	0.037
95% confidence interval for minimum sample value, kHz	59.566	-1.330	69.379	-0.062	77.892	-0.116
95% confidence interval maximum sample value, kHz	59.586	-1.310	69.381	-0.060	77.966	-0.043

A *t* “test” distribution of the experimental data presented in Tables 6.5 (a) and (b) reveal that the maximum frequency difference, Δf , for the F(10,1) mode is 1320 ± 10 Hz with a singularity frequency of 59.576 kHz and an uncertainty of 0.010 kHz. In summary, at the level of 95% confidence level, the frequencies of the singularities corresponding to the F(10,1), F(11,1) and F(12,1) modes occur at 59.576 ± 0.010 kHz, 69.380 ± 0.001 kHz, 77.929 ± 0.037 kHz. Also the cut off frequencies are 60.896 ± 0.090 kHz, 69.411 ± 0.074 kHz and 78.008 ± 0.032 kHz respectively, For these particular modes and a 95% confidence interval, the 80% notch can be detected at frequency difference of 1320 ± 10 Hz, 60.6 ± 1.5 Hz, 79.2 ± 36.7 Hz for the F(10,1), F(11,1) and F(12,1) modes respectively with the presently available equipment. However, the maximum errors obtained are 30 Hz, 6 Hz and 140 Hz for the F(10,1), F(11,1) and F(12,1) modes, respectively. Even one detectable difference is sufficient for a further investigation. In this situation, F(10,1) is the “best” mode to use to discern the notch because reasonable error is obtained with corresponding permissible frequency difference.

6.6 Discussion of results and statistical justification

A Fourier transform worked quite well for the peak frequency difference method but the limitation of this method is the requirement of recognising the signal modes. Sometimes the mode recognition is difficult. However, this method is still useful provided the degradation is not very large or signals modes are recognisable at the starting points. The frequency difference, Δf , has paramount importance as well as the cut-off frequency of unblemished pipe or frequency of singularity of the defective pipe. The frequency difference, Δf , between the cut off frequency and frequency of singularities were calculated with uncertainty. It has been established in section 5.3.2 that the extraction of cut-off frequency is very sensitive to the chosen time window. The cross-correlation has shown to be an excellent candidate for the selection of time window for accurate extraction of cut-off frequency. Also, it shows that the experimental data is repeatable within a 95% confidence level. From the statistical and error analysis of the previously considered higher order mode considered, For example, the frequency shift for F(11,1) is 60.6 ± 1.5 Hz with a maximum error of 6 Hz is confirmed to be measurable.

CHAPTER 7

CONCLUSIONS AND RECOMMENDATIONS

7.1 Conclusions

The objective of this thesis was to develop an ultrasonic, Non-Destructive Testing (NDT) procedure to reliably extract frequencies corresponding to the discontinuities in the spectral densities of radial displacement-measured, time histories. Transmitting, receiving transducers and their ancillary electronic equipment have been characterized in order to obtain the frequency responses. This procedure is important for ensuring that measurements are repeatable. Experimental results show that it is unnecessary for instrumentation to have a perfectly flat frequency response because imperfection can be removed by post processing. Therefore, a procedure was developed to take out the effect of an instrumentation chain's behaviour from the experiment. Furthermore, it became clear that the assumption that the experimental data was periodic was erroneous. This observation was confirmed from the non-periodicity and non-causality of the radial displacement history. Consequently efforts were made to correct these discrepancies. The application of an exponential window clearly shown to the effect of minimizing the leakages although subject cannot be eliminated totally. A cross-correlation concept has been implemented and found to be effective with a damping around 0.25.

The computed response of an idealized cylinder and a response which incorporates and subsequently eliminates the measurement chain's effect has been compared and found to agree reasonably. A value of Etta max greater than 0.01 and higher separation distances such as 10.2H and 25.5H, when neglected from the data, gave better results for the mean and standard deviation of a given data set. This shows that Etta max and separation

distance can be used as a guide but not a good indicator when extracting the cut-off frequencies. The temporal curve fit must converged reasonably well as both the value of residual and Etta max solely depend on this idea. Carefully looking at residuals shows whether the assumptions are reasonable and the choice of model is appropriate. However, using Etta max to select a time window does not give the most accurate cut-off frequencies although it can be used as quick guide. The cross-correlation coefficient procedure gave a better measure of the closeness of the predicted and corresponding curve fitted data.

A straightforward curve fitting of the resulting truncated displacement history, in conjunction with a cross-correlation procedure between 0.995 and 0.999, have been demonstrated to provide reasonable information. A time window of about 600 μs with a cross-correlation coefficient between 0.950 and 0.999 is needed to extract quite accurate cut-off frequencies. This situation occurred when a single and modal superimposed time histories were considered. However, there appeared to be no universal rule for selecting the properties of a time window. If an appropriate time window was chosen carefully, the ensuing cut-off frequencies were close to the values predicted by SAFE. The cross-correlation coefficient has been demonstrated to be a reasonable guide. The finally extracted cut-off frequencies have been compared with those of the idealized cylinder and found to agree very well.

The difference between the frequency of the singularity and the closest cut-off frequency of the unblemished pipe has been found to be a promising alternative to a more tediously found reflection coefficient [3]. The accuracy and repeatability of the frequency shift from the cut-off frequency of a selected mode that is introduced by a notch can be

measured within calculable error bounds. It is confirmed experimentally that singularity are truly introduced by a notch and differences are measurable at a 95% confidence level.

7.2 Recommendations

The following recommendations are suggested for future work.

- 1 Accuracies of the inverse procedure should be investigated at greater transducer separations to assess the effect of wave diffusivity.
- 2 Experiments should be conducted to show the effect of different dimensioned and shaped notches on the spectral density of the corresponding unblemished pipe and determine if singularity frequencies can be used to reliably find these notch's properties.

REFERENCES

- [1] W. Zhu, J. Rose, J. Barshinger, and V. Agarwala, "Ultrasonic guided wave NDT for hidden corrosion detection," *Research in Non-destructive Evaluation*, vol. 10, no. 4, pp. 205–225, 1998.
- [2] J. Rose and J. Barshinger, "Using ultrasonic guided wave mode cut-off for corrosion detection and classification," *Proceedings of the IEEE Ultrasonic Symposium*, vol. 1, pp. 851–854, 1998.
- [3] D. K. Stoyko, "Determining the properties of a pipe defect using guided waves," Ph.D. Thesis, University of Manitoba, 2012.
- [4] M. G. Silk and K. F. Bainton, "The propagation in metal tubing of ultrasonic wave modes equivalent to Lamb waves," *Ultrasonic*, vol. 17, pp. 11-19, 1979.
- [5] J. L. Rose and J. Dittri, "Pulse-echo and through transmission Lamb wave techniques for adhesive bond inspection," *British Journal of NDT*, vol. 34(12), 1992.
- [6] J. L. Rose, K. Rajama and M. Hansch, "Ultrasonic guided waves for NDE of adhesive bonded structures," *Journal of Adhesion*, vol. 50, pp. 71-82. 1995.
- [7] International Atomic Energy Agency, "Non-destructive testing for plant life assessment", IAEA, Training Course Series No. 26, VIENNA, 2005.
- [8] A. Raghavan, "Guided-waves structural health monitoring" Ph.D. dissertation, The University of Michigan, 2004.
- [9] D. K. Stoyko, "Interpreting Wave Propagation in a Homogeneous, Isotropic, Steel Cylinder", M.Sc. Thesis, University of Manitoba, 2004.
- [10] D. N. Alleyne and P. Cawley, "Optimization of Lamb wave inspection techniques," *NDT and E International*, vol. 25, pp. 11-22, 1992.
- [11] L. W. Schmerr, A. Lopez-Sanchez and R. Huang, "Complete ultrasonic transducer characterizations and its use for models and measurements" *Ultrasonic*, vol. 44, pp. 753-757, 2006.
- [12] C. J. Dang and L. W. Schmerr, "Modeling and measuring all the elements of an ultrasonic non-destructive evaluation system. I: Modeling foundations" *Research in Non-destructive Evaluation*, vol. 14, pp. 177-201, 2002.
- [13] J. Krautkramer and H. Krautkramer, "Ultrasonic Testing of Material," 4th edition, Springer-Verlag, New York, 1990.

- [14] K. P. Soldatos. "Review of three dimensional dynamic analyses of circular cylinders and cylindrical shell," *ASME Journal. Applied Mechanics. Revision*, vol. 47(10). pp. 501-516. 1994.
- [15] W. Zhuang, "Numerical modeling for elastodynamic problems in laminated composite cylinders," Ph.D. dissertation, University of Manitoba, Winnipeg, Manitoba, Canada, 1998.
- [16] D. C. Gazis, "Three-dimensional investigation of the propagation of waves in hollow circular cylinders, I. Analytical Foundation," *Journal of the Acoustical Society of America*, vol. 31, pp. 568–573. 1959.
- [17] D. C. Gazis, "Three-Dimensional Investigation of the Propagation of waves in hollow circular cylinders, II. Numerical Results," *Journal of the Acoustical Society of America*, vol. 31, pp. 573–578. 1959.
- [18] D. Alleyne, M. Lowe, and P. Cawley, "Reflection of guided waves from circumferential notches in pipes," *Journal of Applied Mechanics*, vol. 65, no. 3, pp. 635–641, 1998.
- [19] M. Lowe, D. N. Alleyne, and P. Cawley, "Mode conversion of a guided wave by a part-circumferential notch in a pipe," *Journal of Applied Mechanics*, vol. 65, no. 3, pp. 649–656, 1998.
- [20] P. D. Wilcox, R. P. Dalton, M. J. S. Lowe and P. Cawley. "Mode and transducer selection for long range Lamb wave inspection," *Key Eng Material*, vol. 16-68, pp. 152-161, 1999.
- [21] L. Pochhammer, "Ueber die fortpflanzungsgeshwindigkieten schwingungen in einem unbegremten isotropen kreiscylinder," *Zeitschrift fur Mathematik*, vol. 81. Pp. 324-336, 1876.
- [22] C. Chree, "The equations of an isotropic elastic solid in polar and cylindrical coordinates, their solutions and applications" *Transaction of the Cambridge Philosophical Society, Mathematical and Physical Sciences*, vol. 14, pp. 250-369, 1889.
- [23] M. Onoe, H. D. McNiven and R.H. Mindlin, "Dispersion of axially symmetric waves in elastic rods," *ASME Journal Applied. Mechanics*, vol. 29, pp. 729-731, 1962.
- [24] A. E. Armenàkas, D. C. Grazis and G. Herrmann, "Free vibration of circular cylindrical shells," Pergamon Press, *Oxford*, 1969.
- [25] A. E. Armenàkas, "Propagation of harmonic waves in composite cylindrical shells. Part-I Theoretical investigation," *AIA A Journal*, vol. 5, pp. 740-744, 1967.

- [26] A. E. Armenàkas, "Propagation of harmonic waves in composite cylindrical shells. Part-II Numerical analysis," *AIA A Journal*, vol. 9, pp. 599-605, 1971.
- [27] H. D. McNiven, Sackman, J. L., and Shah. A.H., "Dispersion of axially symmetric waves in composite, elastic rods," *Journal of the Acoustical Society of America*, vol. 35, pp. 1602-1609, 1963.
- [28] R. D. Mindlin and H. D. McNiven, "Axially symmetric waves in elastic rod" *AMSE Journal Applied Mechanics*," vol. 1, pp. 15- 151, 1960.
- [29] W. A. Green, "Dispersion relations for elastic waves in bars", *Progress in Solid Mechanics*," vol. 1, pp. 225-261, 1964.
- [30] J. L. Lai, "Propagation of harmonic waves in composite elastic cylindrical," *Journal of the Acoustical Society of America*, vol. 49, pp. 220-228, 1971.
- [31] N. Rattanawangcharoen and A. H. Shah, "Guided waves in laminated isotropic circular cylinder," *Computer Mechanics*, vol. 10, pp. 97- 105, 1992.
- [32] N. Rattanawangcharoen, "Propagation and scattering of elastic waves in laminated circular cylinders," Ph. D. dissertation, The University of Manitoba, Winnipeg, Manitoba Canada, 1993
- [33] D. E. Muller, "A method for solving algebraic equations using an automatic computer," *Mathematical Tables and Aids to Computation*, vol. 10, pp. 208-215, 1956
- [34] I. Mirsky, "Axisymmetric vibrations of orthotropic cylinders" *Journal of the Acoustical Society of America*, vol. 36(11), pp. 2106-2112, 1964.
- [35] I. Mirsky, "Wave propagation in transversely isotropic circular cylinders Part I: Theory" *Journal of the Acoustical Society of America*. Vol. 37(6), pp. 1016-1021. 1965a.
- [36] I. Mirsky, "Wave propagation in transversely isotropic circular cylinders Part II: Numerical results" *Journal of the Acoustical Society of America*, vol. 37(6), pp. 1022- 1026, 1965b.
- [37] N. Rattanawangcharoen, A.H. Shah, and Datta, S.K. "Wave propagation in laminated composite cylinders," *International Journal of Solids and Structures*, vol. 29(6), pp. 767-78 1, 1992.
- [38] N. Rattanawangcharoen, S. B. Datta, and. A.H. Shah, "Non-axisymrnetric guided waves in a composite cylinder with transversely isotropic core" *Geophysics. Journal International*, vol. 118, pp. 317-324, 1994a.

- [39] R. B. Nelson, S.B. Dong, and R.D. Kalra "Vibrations and waves in laminated orthotropic circular cylinders". *Journal of Sound and Vibration*, vol. 18(3), pp. 429-444, 1971.
- [40] K. H. Huang and S.B. Dong, "Propagating waves and edge vibrations in anisotropic cylinders" *Journal of Sound and Vibration*, vol. 96(3), pp. 363-379, 1984.
- [41] J. Oliver "Elastic wave dispersion in a cylindrical rod by a wideband short duration pulse technique" *Journal of the Acoustical Society of America*, vol. 29, pp. 189-194. 1957.
- [42] H. D. McNiven, "Extensional waves in a semi-infinite elastic rod," *Journal of the Acoustical Society of America*, ol. 33, pp. 23-27. 1961.
- [43] H. D. McNiven and A. H. Shah, "The influence of the end mode on the resonant frequencies of finite, hollow, elastic rods" *Journal of Sound and Vibration*. vol.6, pp. 8-19, 1967.
- [44] J. A. Zemanek, "Experimental and theoretical investigation of elastic wave propagation in a cylinder" *Journal of the Acoustical Society of America*, vol. 51(1). pp. 265-283. 1972.
- [45] J. Song, "Reflection and transmission of waves in circular cylindrical bar," Ph.D. dissertation," University of California, Los Angeles. California, USA. 1992.
- [46] Y. Y. Kim, and C. R. Steele. "End effects and time-harmonic longitudinal wave propagation in a semi-infinite solid cylinder," *ASME Journal of Applied Mechanics*. 56. 334346. 1989.
- [47] R. D. Gregory, and I. Gladwell, "Axisymmetric waves in a semi-infinite elastic rod," *Applied Mathematics*, vol. 42, pp. 327-337, 1989.
- [48] Rattanawangcharoen. N, A. H. Shah, and S. K. Datta, "Reflection of waves at the free edge of a laminated circular cylinder," *ASME Journal of Applied Mechanics*., vol. 61, pp. 323-329. 1994b.
- [49] D. K. Stoyko, N. Popplewell and A. H. Shah. "Finding a pipe's elastic and dimensional properties using ultrasonic guided wave cut-off frequency" *NDT&E International*, 2010.
- [50] P. Wilcox, M. Lowe, and P. Cawley, "The effect of dispersion on long-range inspection using ultrasonic guided waves," *NDT&E International*, vol. 34, pp. 1-9, 2001

- [51] D. K. Stoyko, N. Popplewell, A. H. Shah, "Modal Analysis of Transient Ultrasonic Guided Waves in a cylinder," *Computational Mechanics*, Beijing, China. 2007.
- [52] Y. B. Gandole, "Development of signal processing techniques for ultrasonic measurements" *Indian Journal of Science and Technology*, vol. 4, pp. 10, 2011.
- [53] K. Adeogun, "Eliminating the extraneous behaviour of an ultrasonic transducer in Non-Destructive Testing," University of Manitoba, Project report, 2011.
- [54] P. Lacoursiere, "Characterization of transducer coupling," B.Sc. Thesis, University of Manitoba, Winnipeg, Manitoba, Canada, 2011.
- [55] L.W. Schmerr, A. Lopez-Sanchez and R. Huang, "Complete ultrasonic transducer characterization and its use for models and measurements," *Ultrasonic*, vol. 44, pp. e753-e757, 2006.
- [56] S. Colombo, A. Giannopoulos, M.C. Forde, R. Hasson and J. Mulholland, "Frequency response of different couplant materials for mounting transducers," *NDT&E International*, vol. 38, pp. 187-193, 2005.
- [57] K. Dugmore, D. Jonson and M. Walker, "A comparison of signal consistency of common ultrasonic couplants used in the inspection of composite structures," *Composite structures*, vol. 58, pp. 601-603, 2002.
- [58] D. K. Stoyko, K. Adeogun, N. Popplewell, and H. Bai, "Principal challenges in predicting guided wave behaviour in NDT," in *Review of progress in quantitative non-destructive evaluation: proceedings of the 38th annual review of progress in quantitative non-destructive evaluation*, D. Thompson and D. Chimenti, Eds. Melville, New York: American Institute of Physics, p. In press. 2011.
- [59] W. Fladung, R. Rost, "Application and correction of the exponential window for frequency response functions," *Mechanical System and Signal Processing*, vol. 11(1), pp. 23-36, 1997.
- [60] D. E. Newland, "An introduction to Random Vibrations and Spectral Analysis," second edition, Longman House, Burnt Mill Harlow, England, Longman Group Limited, 1984.
- [61] K. Shin and J. K. Hammond, "Fundamentals of Signal Processing for Sound and Vibration Engineers", Southern Gate, Chichester, England, John Wiley & Son, 2008.
- [62] L. Li, G.E. Caldwell, "Coefficient of cross correlation and the time domain correspondence," *Journal of Electromyography and Kinesiology*, vol. 9, pp. 385-389, 1999.

- [63] A. J. Wheeler and A.R. Ganji, "Introduction to Engineering Experimentation", 2nd edition, Upper Saddle River, New Jersey, Pearson Education Inc, 2004.
- [64] D. J. Reaume, H. Eromeijn and R. L. Smith, "Implementing pure adaptive search for global optimization using Markov chain sampling," *Journal of Global Optimization*, vol. 20, pp. 33–47, 2001.
- [65] P. P. Wang and D. S. Chen "Continuous optimization by a variant of simulated annealing," *Computational Optimization and Applications*," vol. 6, pp. 59–71, 1996.
- [66] B. Sharif, "Mode Pursuing sampling method for discrete variable optimization on expensive black box function," *Journal of Mechanical Design*, vol. 130, pp. 1-11, 2008.
- [67] B. Sharif, G. G. Wang and T. Y. ElMenkkawy, "Mode Pursuing Sampling method for discrete Variable Optimization on Expensive Black-Box function" *Engineering optimization*, vol. 36(4), pp. 419-438, 2004.
- [68] L. He, "Time-frequency analysis of ultrasound signal in non-destructive testing using reassignment method," University of Manitoba, Project report, 2011.
- [69] B. Lundin and P. Martensson, "Finding general guidelines for choosing appropriate cut-off frequencies for modal analyses of railway bridges trafficked by high-speed train", Master's Dissertation, Lund University, Lund, Sweden, 2006.
- [70] D. Stoyko, A. Shah, and N. Popplewell, "Detection of a pipe's localized wall thinning using ultrasonic guided waves," in *Proceedings of the 10th International Conference on Recent Advances in Structural Dynamics (RASD 2010)*, M. Brennan, Ed. Southampton: Institute Sound and Vibration Research, 2010, accepted for inclusion.
- [71] T. Hayashi and M. Murase, "Defect imaging with guided waves in a pipe," *Acoustical Society of America*, vol. 117, pp. 2134-2140, 2005.
- [72] L. Satyarnarayan, J. Chandrasekaran, B. Maxfield and K. Balasubramanian. "Circumferential higher order guided wav modes for the detection and sizing of cracks and pinholes in pipe support regions," *NDT&E International*, vol. 41, pp. 32-43, 2008.
- [73] J. Mu, L. Zhang, and J. Rose, "Defect circumferential sizing by using long range ultrasonic guided wave focusing techniques in pipe," *Non-destructive Testing And Evaluation*, vol. 22, no. 4, pp. 239–253, 2007.

- [74] J. Holman, "Experimental methods for engineers", 2nd, New York, United States of America: McGraw-Hill, 1971.
- [75] J. M. Boiano, M. E. Wallace, W. K. Sieber, J. H. Groff, J. Wang and K. Ashley, "Comparison of three sampling and analytical methods for the determination of airborne hexavalent chromium", *Journal of Environmental monitoring*, vol. 2, pp. 329-333, 2000.

APPENDICES

APPENDIX A

APPROXIMATE EQUATIONS OF MOTION USING SAFE

The strain and displacement vectors are related by the standard differential equation. In anticipation of a separation of variables solution strategy, the differential operators that relate the components of $\boldsymbol{\varepsilon}$ to \mathbf{u} are written in split form

$$\boldsymbol{\varepsilon} = (\mathbf{L}_r + \mathbf{L}_\theta + \mathbf{L}_z)\mathbf{u} \quad (\text{A.1})$$

$$\mathbf{L}_r = \begin{bmatrix} \frac{\partial}{\partial r} & \dots & \dots \\ \frac{1}{r} & \dots & \dots \\ \dots & \dots & \dots \\ \dots & \dots & \dots \\ \dots & \dots & \frac{\partial}{\partial r} \\ \dots & \frac{\partial}{\partial r} - \frac{1}{r} & \dots \end{bmatrix}; \quad \mathbf{L}_\theta = \begin{bmatrix} \dots & \dots & \dots \\ \dots & \frac{1}{r} \frac{\partial}{\partial \theta} & \dots \\ \dots & \dots & \dots \\ \dots & \dots & \frac{1}{r} \frac{\partial}{\partial \theta} \\ \dots & \dots & \dots \\ \frac{1}{r} \frac{\partial}{\partial \theta} & \dots & \dots \end{bmatrix}; \quad \mathbf{L}_z = \begin{bmatrix} \dots & \dots & \dots \\ \dots & \dots & \dots \\ \dots & \dots & \frac{\partial}{\partial z} \\ \dots & \frac{\partial}{\partial z} & \dots \\ \frac{\partial}{\partial z} & \dots & \dots \\ \dots & \dots & \dots \end{bmatrix} \quad (\text{A.2})$$

The (differential) equations of wave motion, expressed in the cylindrical coordinate system, are given by

$$\sigma_{rr,r} \frac{1}{r} \sigma_{r\theta,0} + \sigma_{rz,z} \frac{1}{r} (\sigma_{rr} - \sigma_{\theta\theta}) + b_r = \rho \ddot{u} \quad (\text{A.3})$$

$$\sigma_{\theta r} + \frac{1}{r} \sigma_{\theta\theta,0} + \sigma_{\theta z,z} + \frac{2}{r} \sigma_{\theta r} + b_\theta = \rho \ddot{v} \quad (\text{A.4})$$

$$\sigma_{zr,r} + \frac{1}{r} \sigma_{z\theta,0} + \sigma_{zz,z} + \frac{1}{r} \sigma_{zr} + b_z = \rho \ddot{w} \quad (\text{A.5})$$

where b is a body force and ρ is the cylinder's mass density. A comma in equation (A.3) denotes differentiation with respect to the spatial variable that follows and an overdot indicates differentiation with respect to time.

Isoparametric finite element methodology is employed in the thickness discretization. The interpolation functions n 's in a typical lamina. Say k -th lamina in terms of local variable ζ ($-1 \leq \zeta \leq +1$) are given by

$$\mathbf{n}(\zeta) = [\eta_b(\zeta), \eta_m(\zeta), \eta_e(\zeta)] = \left[\frac{1}{2}\zeta(\zeta-1), (1-\zeta^2), \frac{1}{2}\zeta(\zeta+1) \right] \quad (\text{A.6})$$

and

$$\zeta = \frac{2(r - r_{km})}{h_k} \quad (\text{A.7})$$

where subscripts b, m, f denote the back (inner), middle, and front (outer) nodal surfaces. And r_k , h_k represent mid-surface radius and thickness of the k -th lamina respectively. Accordingly, interpolations of the coordinate variable, r and any field variable. Say, s , over the isoparametric element appears as

$$r = \eta_b(\zeta)r_b + \eta_m(\zeta)r_m + \eta_e(\zeta)r_e; \quad x = \eta_b(\zeta)x_b + \eta_m(\zeta)x_m + \eta_e(\zeta)x_e \quad (\text{A.8})$$

where subscripts b, m, f denote the back (inner), middle, and front (outer) nodal surfaces. And r_k , h_k represent mid-surface radius and thickness of the k -th lamina respectively. Accordingly, interpolations of the coordinate variable, r and any field variable. Say, s , over the isoparametric element appears as

$$\mathbf{n}(\zeta) = [\eta_b(\zeta), \eta_m(\zeta), \eta_e(\zeta)] = \left[\frac{1}{2}\zeta(\zeta-1), (1-\zeta^2), \frac{1}{2}\zeta(\zeta+1) \right] \quad (\text{A.9})$$

$$\zeta = \frac{2(r - r_{km})}{h_k} \quad (\text{A.10})$$

Casting u as an assembled displacement interpolation field over the complete thickness profile of the cylinder gives

$$\begin{bmatrix} u(r, \theta, z, t) \\ v(r, \theta, z, t) \\ w(r, \theta, z, t) \end{bmatrix} = \begin{bmatrix} N(r\{\zeta\}) & \cdot & \cdot \\ \cdot & N(r\{\zeta\}) & \cdot \\ \cdot & \cdot & N(r\{\zeta\}) \end{bmatrix} \begin{bmatrix} U(\theta, z, t) \\ V(\theta, z, t) \\ W(\theta, z, t) \end{bmatrix} \quad (\text{A.11})$$

The strain and stress tensor can be written in vector form as

$$\boldsymbol{\varepsilon} = \mathbf{B}_1 \mathbf{U} + \mathbf{B}_2 \mathbf{U}_{,0} + \mathbf{B}_3 \mathbf{U}_{,z} \quad (\text{A.12})$$

and

$$\boldsymbol{\sigma} = \mathbf{D} \mathbf{B}_1 \mathbf{U} + \mathbf{D} \mathbf{B}_2 \mathbf{U}_{,0} + \mathbf{D} \mathbf{B}_3 \mathbf{U}_{,z}, \quad (\text{A.13})$$

\mathbf{D} is a matrix of cylindrical orthotropic elastic moduli with the orthotropy axis coinciding with the z -axis

$$\mathbf{D} = \begin{bmatrix} D_{11} & D_{12} & D_{13} & 0 & 0 & 0 \\ D_{12} & D_{22} & D_{23} & 0 & 0 & 0 \\ D_{13} & D_{23} & D_{33} & 0 & 0 & 0 \\ 0 & 0 & 0 & D_{44} & 0 & 0 \\ 0 & 0 & 0 & 0 & D_{55} & 0 \\ 0 & 0 & 0 & 0 & 0 & D_{66} \end{bmatrix} = \begin{bmatrix} \lambda + 2\mu & \lambda & \lambda & 0 & 0 & 0 \\ \lambda & \lambda + 2\mu & \lambda & 0 & 0 & 0 \\ \lambda & \lambda & \lambda + 2\mu & 0 & 0 & 0 \\ 0 & 0 & 0 & \mu & 0 & 0 \\ 0 & 0 & 0 & 0 & \mu & 0 \\ 0 & 0 & 0 & 0 & 0 & \mu \end{bmatrix} \quad (\text{A.14})$$

Where λ and μ are Lamé's constants. Note that Lamé's constants can be related to the more familiar Young's modulus, E , and Poisson's ratio, ν , through:

$$\lambda = \frac{E\nu}{(1+\nu)(1-2\nu)} \quad (\text{A.15})$$

and

$$\mu = \frac{E}{2(1+\nu)} \quad (\text{A.16})$$

where μ is identical to the shear modulus, G . All the material properties are taken to coincide with the values used in [49]. Consequently, the value of λ and μ for the average of value measured ultrasonically and conventionally are summarized in Table 2.1.

Where the components of strain-transformation matrices $\mathbf{B}_i (i = 1, 2, 3)$ are given by and a comma denotes partial differentiation with respect to the variable that follows

$$\mathbf{B}_1 = \begin{bmatrix} N_{,r} & \dots & \dots \\ N/r & \dots & \dots \\ \dots & \dots & \dots \\ \dots & \dots & \dots \\ \dots & \dots & N_{,r} \\ \dots & N_{,r} - N/r & \dots \end{bmatrix}; \mathbf{B}_2 = \begin{bmatrix} \dots & \dots & \dots \\ \dots & N/r & \dots \\ \dots & \dots & \dots \\ \dots & \dots & N/r \\ \dots & \dots & \dots \\ N/r & \dots & \dots \end{bmatrix}; \mathbf{B}_3 = \begin{bmatrix} \dots & \dots & \dots \\ \dots & \dots & \dots \\ \dots & \dots & N \\ \dots & N & \dots \\ N & \dots & \dots \\ \dots & \dots & \dots \end{bmatrix} \quad (\text{A.17})$$

The system stiffness matrices, \mathbf{K}_i 's, mass \mathbf{M} and consistent load vector \mathbf{F} are defined by

$$\mathbf{K}_1 = 2\pi \int \mathbf{B}_1^T \mathbf{D} \mathbf{B}_1 r dr; \quad \mathbf{K}_2 = 2\pi \int (\mathbf{B}_1^T \mathbf{D} \mathbf{B}_2 - \mathbf{B}_2^T \mathbf{D} \mathbf{B}_1) r dr \quad (\text{A.18})$$

$$\mathbf{K}_4 = 2\pi \int \mathbf{B}_2^T \mathbf{D} \mathbf{B}_2 r dr; \quad \mathbf{K}_3 = 2\pi \int (\mathbf{B}_1^T \mathbf{D} \mathbf{B}_3 - \mathbf{B}_3^T \mathbf{D} \mathbf{B}_1) r dr \quad (\text{A.19})$$

$$\mathbf{K}_6 = 2\pi \int \mathbf{B}_3^T \mathbf{D} \mathbf{B}_3 r dr; \quad \mathbf{K}_5 = 2\pi \int (\mathbf{B}_2^T \mathbf{D} \mathbf{B}_3 - \mathbf{B}_3^T \mathbf{D} \mathbf{B}_2) r dr \quad (\text{A.20})$$

For the concentrated load, \mathbf{F}_0 contain zero entries everywhere except at the nodal surfaces $r = r_0$, where the (r, θ, z) components are $(\alpha_{Fr}, \alpha_{F\theta}, \alpha_{Fz})$, i.e.,

$$\mathbf{F}_0^T = \langle \mathbf{F}_{0r}^T; \mathbf{F}_{0\theta}^T; \mathbf{F}_{0z}^T \rangle = \langle 0, 0, \dots, \alpha_{Fr}, \dots, 0; 0, 0, \dots, \alpha_{F\theta}, \dots, 0; 0, 0, \dots, \alpha_{Fz}, \dots, 0 \rangle \quad (\text{A.21})$$

Since the loads magnitudes is unity, $(\alpha_{Fr}, \alpha_{F\theta}, \alpha_{Fz})$ are also the direction cosines of the unit vector \mathbf{e}_F defining the direction of the load. i.e.,

$$\mathbf{e}_F = \alpha_{Fr} \mathbf{e}_r + \alpha_{F\theta} \mathbf{e}_\theta + \alpha_{Fz} \mathbf{e}_z \quad (\text{A.22})$$

With $(\mathbf{e}_r, \mathbf{e}_\theta, \mathbf{e}_z)$ as the base vectors of the cylindrical coordinates. Applying the Fourier transform to the Fourier series expansion of equation (2.51) transforms the n th term of the load's approximation from the spatial to the wavenumber domain. Substituting the result

into equation (2.3.12) leads to the n th circumferential harmonic of the Green's function in the spatial domain to be

$$\int_{-\theta_0}^{+\theta_0} q_0 r_0 d\theta = 1 \quad \text{or} \quad q_0 = \frac{1}{2r_0\theta_0}. \quad (\text{A.23})$$

APPENDIX B
ERROR ANALYSIS

1. Standard deviation of the mean

It is necessary to repeat the set of measurements. The mean value of a large number of sets is presumably the true value. Consequently obtain the standard deviation of the mean of a single set of data from this true value [63, 74].

Thus

$$\sigma_m = \frac{\sigma}{\sqrt{n}} \quad (\text{B.1})$$

where

σ_m = standard deviation of the mean value

σ = standard deviation of the set of measurements

n = number of measurements in the set

2. Student's t-Distributions

To determine the standard deviation of the mean in terms of the standard deviation of the population. For small sample ($n < 10$) this relation has been shown to be somewhat unreliable. A better method for estimating confidence interval was developed by Student by introducing the variable t such that

$$\Delta = \frac{t\sigma}{\sqrt{n}} \quad (\text{B.2})$$

where

$$t = \frac{\bar{x} - X}{\sqrt{\sigma}} \sqrt{n} \quad (\text{B.3})$$

where

Δ = confidence deviation

n = number of observations

\bar{x} = mean of n observations

X = mean of normal population which the samples are taken from

Student then develop a distribution function $f(t)$ such that

$$f(t) = \frac{K_0}{\left(1 + \frac{t^2}{n-i}\right)^{\frac{n}{2}}} \quad (\text{B.4})$$

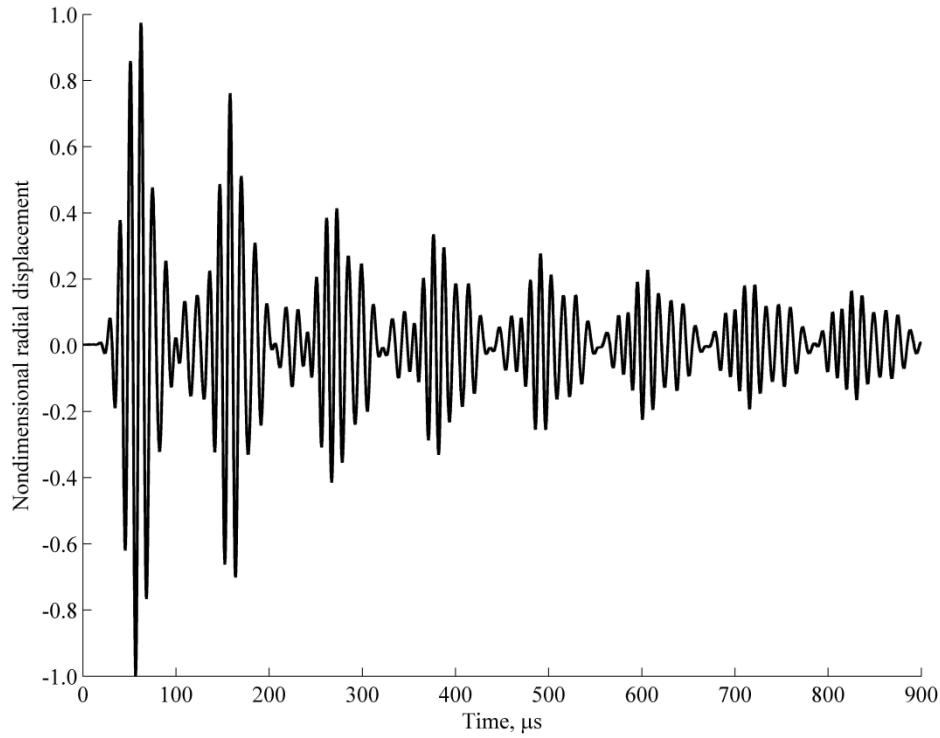
$$f(t) = K_0 \left(1 + \frac{t^2}{v}\right)^{(v+1)/2} \quad (\text{B.5})$$

where K_0 is a constant which depends on n and v is $(n - 1)$ degree of freedom [74]

APPENDIX C

TIME HISTORY AND CORRESPONDING SPECTRAL DENSITY FOR HIGHER FLEXURAL MODES

(a)



(b)

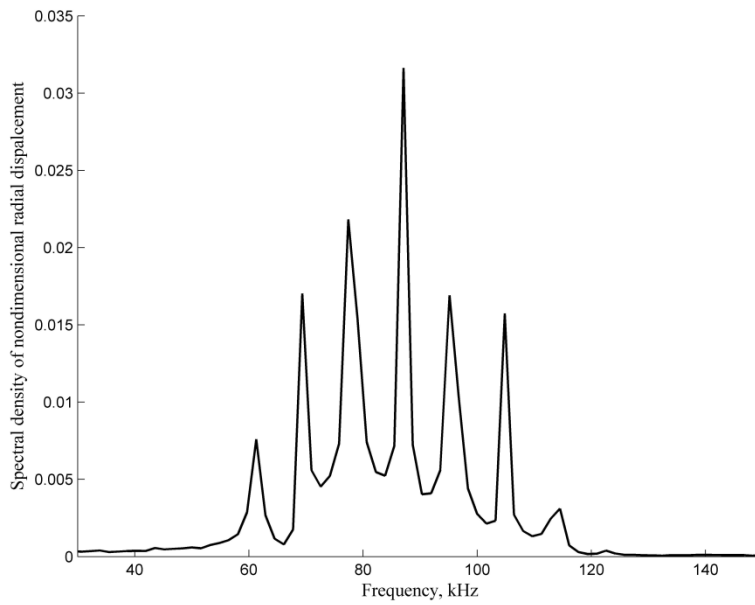


Figure C1 (a) Response history for the 80% circumferential notch and (b) corresponding spectral density.

APPENDIX D

Matlab Codes

MATLAB M-FILE for plotting frequency response function of the instrumentation chain using beeswax for repeatability.

Amplitude

```
load BeeswaxN1.mat A1 B1 C1 D1
figure
plot(A1,B1/abs(max(B1)), 'k','LineWidth',1.5);
hold on
load BeeswaxN2.mat A1 B1 C1 D1
plot(A1,B1/abs(max(B1)), 'r','LineWidth',1.5);
hold on
load BeeswaxN3.mat A1 B1 C1 D1
plot(A1,B1/abs(max(B1)), 'g','LineWidth',1.5);
hold on
load BeeswaxN4.mat A1 B1 C1 D1
plot(A1,B1/abs(max(B1)), 'b','LineWidth',1.5);
hold on
load BeeswaxN5.mat A1 B1 C1 D1
plot(A1,B1/abs(max(B1)), '--g','LineWidth',1.5);
hold on
load BeeswaxN6.mat A1 B1 C1 D1
plot(A1,B1/abs(max(B1)), 'y','LineWidth',1.5);
hold on
load BeeswaxN7.mat A1 B1 C1 D1
plot(A1,B1/abs(max(B1)), '--k','LineWidth',1.5);
hold on
load BeeswaxN8.mat A1 B1 C1 D1
plot(A1,B1/abs(max(B1)), '--r','LineWidth',1.5);
hold on
load BeeswaxN9.mat A1 B1 C1 D1
plot(A1,B1/abs(max(B1)), '--b','LineWidth',1.5);
hold on
load BeeswaxN10.mat A1 B1 C1 D1

plot(A1,B1/abs(max(B1)), '--y','LineWidth',1.5);
ylabel('Normalized Amplitude','FontName','Times New Roman','FontSize',12);
xlabel('Frequency, kHz','FontName','Times New Roman','FontSize',12);
set(gca,'FontName','Times New Roman','FontSize',12,'Layer','top');
set(gca,'FontName','Times New Roman','FontSize',12,'Layer','top');
set(gca,'YTick',[-1.0:0.2:1.0]);
xt=get(gca, 'YTick');
fmt=3.1;
```

```
x1=fortick(xt, fmt);
set(gca, 'YTickLabel', x1, 'YTick', xt)
```

```
hold on
```

```
plot([20 120],[1 1], 'k--','LineWidth',1.5);
text(89,0.98,'Ideal','FontName','Times New Roman','FontSize',12)
text(86,0.23,'Actual','FontName','Times New Roman','FontSize',12)
set(gca,'FontName','Times New Roman','FontSize',12,'Layer','top');
set(gca,'FontName','Times New Roman','FontSize',12,'Layer','top');
box off
hold off
legend('Test 1','Test 2','Test 3','Test 4','Test 5','Test 6','Test 7','Test
8','location','Northwest');
```

```
% legend('N1','N2','N3','N4','N5','N6','N7','N8','N9','N10'); % plot the legend
```

For Phase

```
load BeeswaxN1.mat A1 B1 C1 D1
figure
plot(A1,180/pi*unwrap(pi/180*D1), 'k','LineWidth',1.5);
hold on
load BeeswaxN2.mat A1 B1 C1 D1
plot(A1,180/pi*unwrap(pi/180*D1), 'r','LineWidth',1.5);
hold on
load BeeswaxN3.mat A1 B1 C1 D1
plot(A1,180/pi*unwrap(pi/180*D1), 'g','LineWidth',1.5);
hold on
load BeeswaxN4.mat A1 B1 C1 D1
plot(A1,180/pi*unwrap(pi/180*D1), 'b','LineWidth',1.5);
hold on
load BeeswaxN5.mat A1 B1 C1 D1
plot(A1,180/pi*unwrap(pi/180*D1), '--g','LineWidth',1.5);
hold on
load BeeswaxN6.mat A1 B1 C1 D1
plot(A1,180/pi*unwrap(pi/180*D1), 'y','LineWidth',1.5);
hold on
load BeeswaxN7.mat A1 B1 C1 D1
plot(A1,180/pi*unwrap(pi/180*D1), '--k','LineWidth',1.5);
hold on
load BeeswaxN8.mat A1 B1 C1 D1
plot(A1,180/pi*unwrap(pi/180*D1), '--r','LineWidth',1.5);
hold on
load BeeswaxN9.mat A1 B1 C1 D1
plot(A1,180/pi*unwrap(pi/180*D1), '--b','LineWidth',1.5);
```

```

load BeeswaxN10.mat A1 B1 C1 D1
plot(A1,180/pi*unwrap(pi/180*D1), '--y','LineWidth',1.5);
ylabel('Relative Phase, Degree','FontName','Times New Roman','FontSize',12);
xlabel('Frequency, kHz','FontName','Times New Roman','FontSize',12);
hold on
plot([20 120],[0 0], 'k--','LineWidth',1.5);
text(40,7,'Ideal','FontName','Times New Roman','FontSize',12)
text(50,232,'Actual','FontName','Times New Roman','FontSize',12)
set(gca,'FontName','Times New Roman','FontSize',12,'Layer','top');
set(gca,'FontName','Times New Roman','FontSize',12,'Layer','top');
hold off
box off

% legend('N1','N2','N3','N4','N5','N6','N7','N8','N9','N10'); % plot the legend

```

APPENDIX E

MATLAB M-FILE FOR PLOTTING THE HISTOGRAM FOR THE CUT-OFF FREQUENCIES

```
M= xlsread ('C:\Documents and Settings\Adeogun Kazeem\Desktop\Final 100
MECG_7780\Post Data Rev405.1h.xls');
f10d=M(:,1); % cut off frequency obtained from DFT for mode 10
f10c=M(:,2); % cut off frequency obtained from curve - fit for mode 10
f11d=M(:,3); % cut off frequency obtained from DFT for mode 11
f11c=M(:,4); % cut off frequency obtained from curve - fit for mode 11
f12d=M(:,5); % cut off frequency obtained from DFT for mode 12
f12c=M(:,6); % cut off frequency obtained from curve - fit for mode 12
% plot the histogram for the cut off frequency obtained from curve - fitting for mode 10
figure
[nb,b]=hist(f10c,50);
bar(b,nb);
hist(f10c,50)
box off
xlabel('Frequency, kHz','fontname','Times New Roman','fontsize',12);
ylabel('Number of occurrences','fontname','Times New Roman','fontsize',12);
set(gca,'fontname','Times New
Roman','fontsize',12,'xtick',[60.7:0.1:61.8],'ytick',[1:1:10]);
print('-djpeg','-r600','Fig a5.jpg')
% plot the histogram for the cut off frequency obtained from curve-fit for mode 11
figure
[c,d]=hist(f11c,50);
bar(d,c);
hist(f11c,50)
box off
xlabel('Frequency, kHz','fontname','Times New Roman','fontsize',12);
ylabel('Number of occurrences','fontname','Times New Roman','fontsize',12);
set(gca,'fontname','Times New
Roman','fontsize',12,'xtick',[71.3:0.1:72.1],'ytick',[1:1:10]);
print('-djpeg','-r600','Fig b5.jpg')
% plot the histogram for the cut off frequency obtained from curve - fit for mode 12
figure
[e,f]=hist(f12c,50);
bar(f,e);
hist(f12c,50)
box off
xlabel('Frequency, kHz','fontname','Times New Roman','fontsize',12);
ylabel('Number of occurrences','fontname','Times New Roman','fontsize',12);
set(gca,'fontname','Times New Roman','fontsize',12,'xtick',[82:0.2:83.4],'ytick',[1:1:10]);
print('-djpeg','-r600','Fig c5.jpg')
mul=mean(f10c);
```

```

sigma1=std(f10c);

% Normal cummulative probabily plot for the cut off frequency obtained

% from curve - fit for mode 10
Figure
normplot(f10c);
xlabel('Frequency, kHz','fontname','Times New Roman','fontsize',12);
ylabel('Probability','fontname','Times New Roman','fontsize',12);
box off
print('-djpeg','-r600','Fig d5.jpg')
mu2=mean(f11c);
sigma2=std(f11c);
% Normal cummulative probabily plot for the cut off frequency obtained
% from curve - fit for mode 11
figure
normplot(f11c);
xlabel('Frequency, kHz','fontname','Times New Roman','fontsize',12);
ylabel('Probability','fontname','Times New Roman','fontsize',12);
box off
print('-djpeg','-r600','Fig e5.jpg')
mu3=mean(f12c);
sigma3=std(f12c);
% Normal cummulative probabily plot for the cut off frequency obtained
% from curve - fit for mode 12
figure
normplot(f12c);
xlabel('Frequency, kHz','fontname','Times New Roman','fontsize',12);
ylabel('Probability','fontname','Times New Roman','fontsize',12);
box off
print('-djpeg','-r600','Fig f5.jpg')
figure
histfit(f10c,50);
box off
xlabel('Frequency, kHz','fontname','Times New Roman','fontsize',12);
ylabel('Number of occurrences','fontname','Times New Roman','fontsize',12);
set(gca,'fontname','Times New
Roman','fontsize',12,'xtick',[60.7:0.2:61.8],'ytick',[1:1:10]);
print('-djpeg','-r600','Fig g5.jpg')
figure
histfit(f11c,50)
xlabel('Frequency, kHz','fontname','Times New Roman','fontsize',12);
ylabel('Number of occurrences','fontname','Times New Roman','fontsize',12);
set(gca,'fontname','Times New
Roman','fontsize',12,'xtick',[71.3:0.1:72.1],'ytick',[1:1:10]);
print('-djpeg','-r600','Fig h5.jpg')

```

```
figure
histfit(f12c,50)
box off
xlabel('Frequency, kHz','fontname','Times New Roman','fontsize',12);
ylabel('Number of occurrences','fontname','Times New Roman','fontsize',12);
set(gca,'fontname','Times New Roman','fontsize',12,'xtick',[82:0.2:83.4],'ytick',[1:1:10]);
print('-djpeg','-r600','Fig i5.jpg')
```

```
B=[b' nb' d' c' f' e']
```

```
A=[mu1 sigma1 mu2 sigma2 mu3 sigma3]
```

APPENDIX F

MATLAB M-FILE for eliminating the extraneous behaviours of transducer chain

```
load R500Res.mat Kfreq Kamp Kphase
```

```
Kfreq=1E3*Kfreq;
```

```
load Summed1.mat t xtot
```

```
xtot1=xtot;
```

```
figure
```

```
plot(t*1e6,xtot1/max(abs(xtot1)),'LineWidth',1.5);
```

```
xlabel('Time, \mus', 'fontname','Times New roman','fontsize',12');
```

```
ylabel('Non-dimensional Radial displacement','FontName','Times New Roman','FontSize',12);
```

```
set(gca,'FontName','Times New Roman','FontSize',12,'Layer','top');
```

```
set(gca,'FontName','Times New Roman','FontSize',12,'Layer','top');
```

```
set(gca,'YTick',[-1.0:0.2:1.0]);
```

```
xt=get(gca, 'YTick');
```

```
fnt=3.1;
```

```
xtl=fortick(xt, fnt);
```

```
set(gca, 'YTickLabel', xtl, 'YTick', xt)
```

```
box off
```

```
box off
```

```
npts2=length(xtot);
```

```
dt=t(3)-t(2);
```

```
df=1./(dt*(npts2-1));
```

```
Y=fft(xtot);
```

```
NumUniquePts1=ceil((npts2+1)/2);
```

```
fs2=1/(t(4)-t(3));
```

```
% This is an evenly spaced frequency vector with NumUniquePts points.
```

```
freqfft2=(0:NumUniquePts1-1)*fs2/npts2;
```

```
if ~rem(npts2,2)
```

```
    % Here NFFT is even; therefore, Nyquist point is included.
```

```
    Ny=true;
```

```
else
```

```
    Ny=false;
```

```
end
```

```
if Ny
```

```

fall3=[freqfft2 -fliplr(freqfft2(2:end-1))]; % even, flip the freqfft, negate it and arrange
them together up to the penultimate frequency point.
else
    fall3=[freqfft2 -fliplr(freqfft2(2:end))]; % odd, flip the freqfft, negate it and arrange
them together up to the end frequency point.
end

figure
plot(fall3,abs(Y));
box off

TF=Kamp/max(abs(Kamp)).*exp(1i*pi/180*Kphase);

IFRF3=1./TF;

Fy=zeros(size(Y));

for i=1:length(Y)
    if abs(fall3(i))<min(Kfreq)||abs(fall3(i))>max(Kfreq) % ignore fall below Kfreq and
above Kfreq
        %Do nothing...
    elseif fall3(i)>0
        Fy(i)=Y(i)*interp1(Kfreq,IFRF3,fall3(i));
    else
        Fy(i)=Y(i)*conj(interp1(Kfreq,IFRF3,-fall3(i))); %conj(Z) returns the complex
conjugate of the elements of Z.
    end
end

fz=ifft(Fy);
fza=real(fz);

e=exp(-t.*4279.62);
xtot2=xtot.*e;
Y1=fft(xtot2);
NumUniquePts1=ceil((npts2+1)/2);
fs2=1/(t(4)-t(3));

% This is an evenly spaced frequency vector with NumUniquePts points.
freqfft3=(0:NumUniquePts1-1)*fs2/npts2;

if ~rem(npts2,2)
    % Here NFFT is even; therefore, Nyquist point is included.
    Ny=true;
else
    Ny=false;
end

```

```

end
if Ny
fall4=[freqfft3 -fliplr(freqfft3(2:end-1))]; % even, flip the freqfft, negate it and arrange
them together up to the penultimate frequency point.
else
fall4=[freqfft3 -fliplr(freqfft3(2:end))]; % odd, flip the freqfft, negate it and arrange
them together up to the end frequency point.
end

figure
plot(fall4,abs(Y));
box off

TF2=Kamp/max(abs(Kamp)).*exp(1i*pi/180*Kphase);

IFRF4=1./TF;

Fy1=zeros(size(Y1));

for i=1:length(Y1)
if abs(fall4(i)<min(Kfreq)||abs(fall3(i))>max(Kfreq) % ignore fall below Kfreq and
above Kfreq
%Do nothing...
elseif fall3(i)>0
Fy1(i)=Y1(i)*interp1(Kfreq,IFRF3,fall3(i));
else
Fy1(i)=Y1(i)*conj(interp1(Kfreq,IFRF3,-fall3(i))); %conj(Z) returns the complex
conjugate of the elements of Z.
end
end

fz1=ifft(Fy1);
fz3=fz1./e;

% save windo5H.mat t fz3

load Summed1.mat t xtot
xtot8=xtot;
figure
subplot(1,2,1)
plot(1E6*t,xtot8/max(abs(xtot8)), 'k', 'LineWidth', 1.5)
xlabel('Time, \mus', 'fontname', 'Times New roman', 'fontSize', 12);
ylabel('Non-dimensional Radial displacement', 'FontName', 'Times New
Roman', 'FontSize', 12);
set(gca, 'FontName', 'Times New Roman', 'FontSize', 12, 'Layer', 'top');
set(gca, 'FontName', 'Times New Roman', 'FontSize', 12, 'Layer', 'top');

```

```

set(gca,'YTick',[-1.0:0.2:1.0]);
xt=get(gca, 'YTick');
fmt=3.1;
xtl=fortick(xt, fmt);
set(gca, 'YTickLabel', xtl, 'YTick', xt)
% xlim([0 700])
box off
subplot(1,2,2)
plot(1E6*t,fz3/max(abs(fz3)), 'k', 'LineWidth', 1.5)
box off
xlabel('Time, \mus', 'fontname', 'Times New roman', 'fontsize', 12);
ylabel('Non-dimensional Radial displacement', 'FontName', 'Times New
Roman', 'FontSize', 12);
set(gca, 'FontName', 'Times New Roman', 'FontSize', 12, 'Layer', 'top');
set(gca, 'FontName', 'Times New Roman', 'FontSize', 12, 'Layer', 'top');
set(gca, 'YTick', [-1.0:0.2:1.0]);
xt=get(gca, 'YTick');
fmt=3.1;
xtl=fortick(xt, fmt);
set(gca, 'YTickLabel', xtl, 'YTick', xt)
% xlim([0 700])
box off

load Summed1.mat t xtot
xtot7=xtot;
figure
subplot(1,2,1)
plot(1E6*t,xtot7/max(abs(xtot7)), 'k', 'LineWidth', 1.5)
xlabel('Time, \mus', 'fontname', 'Times New roman', 'fontsize', 12);
ylabel('Non-dimensional Radial displacement', 'FontName', 'Times New
Roman', 'FontSize', 12);
set(gca, 'FontName', 'Times New Roman', 'FontSize', 12, 'Layer', 'top');
set(gca, 'FontName', 'Times New Roman', 'FontSize', 12, 'Layer', 'top');
set(gca, 'YTick', [-1.0:0.2:1.0]);
xt=get(gca, 'YTick');
fmt=3.1;
xtl=fortick(xt, fmt);
set(gca, 'YTickLabel', xtl, 'YTick', xt)
xlim([0 700])
box off
subplot(1,2,2)
plot(1E6*t,fza/max(abs(fza)), 'k', 'LineWidth', 1.5)
box off
xlabel('Time, \mus', 'fontname', 'Times New roman', 'fontsize', 12);
ylabel('Non-dimensional Radial displacement', 'FontName', 'Times New
Roman', 'FontSize', 12);

```

```
set(gca,'FontName','Times New Roman','FontSize',12,'Layer','top');
set(gca,'FontName','Times New Roman','FontSize',12,'Layer','top');
set(gca,'YTick',[-1.0:0.2:1.0]);
xt=get(gca, 'YTick');
fmt=3.1;
xtl=fortick(xt, fmt);
set(gca, 'YTickLabel', xtl, 'YTick', xt)
xlim([0 700])
box off
```

APPENDIX G

MATLAB M-FILE for Extracting the cut-off frequency using curve-fit procedure

```
close all
clear
clc

load Summed5.1H0c.mat t xtot

plot(t*1e6,xtot/max(abs(xtot)),'k','LineWidth',1.2);
xlabel('Time, \mus', 'fontname','Times New roman','fontsize',12');
ylabel('Nondimensional radial displacement','FontName','Times New Roman','FontSize',12);
set(gca,'FontName','Times New Roman','FontSize',12,'Layer','top');
set(gca,'FontName','Times New Roman','FontSize',12,'Layer','top');
set(gca,'YTick',[-1.0:0.2:1.0]);
xt=get(gca,'YTick');
fmt=3.1;
xtl=fortick(xt,fmt);
set(gca,'YTickLabel',xtl,'YTick',xt)
box off

tf=t(>=290E-6&t<=700E-6);
xf=fz3(t>=290E-6&t<=700E-6);

Dt=tf(3)-tf(2);

[MX,f,phi]=dksfft(xf,Dt);

fguess=f(dkspeak(MX));
Aguess=MX(dkspeak(MX));
phiguess=pi/180*phi(dkspeak(MX));
[Aguess,IX]=sort(Aguess,'descend');
fguess=fguess(IX);
phiguess=phiguess(IX);
fguess(5:end)=[];
Aguess(5:end)=[];
phiguess(5:end)=[];

PG=zeros(1,5*length(Aguess));
lb=zeros(1,5*length(Aguess));
ub=zeros(1,5*length(Aguess));
PG(1:5:end)=Aguess;
PG(2:5:end)=fguess;
PG(3:5:end)=phiguess;
PG(5:5:end)=200E-6;
lb(3:5:end)=-pi;
lb(5:5:end)=100E-6;
```

```

ub(1:5:end)=inf;
ub(2:5:end)=inf;
ub(3:5:end)=pi;
ub(4:5:end)=inf;
ub(5:5:end)=1E-3;

```

```

options=optimset('Display','final','MaxFunEvals',1500,'MaxIter',1500,'TolFun',1E-10,'TolX',1E-10,'FunValCheck','off',... 'OutputFcn',[],'PlotFcns',{@optimplotx
@optimplotfunccount@optimplotfval},'ActiveConstrTol',[],'BranchStrategy',[],'DerivativeCheck','on','Diagnostics','off',... 'DiffMaxChange',1E1,'DiffMinChange',1E10,'GoalsExactAchieve',[],'GradConstr',[],'GradObj',[],'Hessian',[],'HessMult',[],... 'HessPattern',[],'HessUpdate',[],'InitialHessType',[],'InitialHessMatrix',[],'Jacobian','on','JacobMult',[],... 'JacobPatten','sparse(ones(jrows,jcols))','LargeScale','on','LevenbergMarquardt','on','LineSearchType','quadcubic','MaxNodes',[],... 'MaxPCGIter','max(1,floor(numberofvariables/2))','MaxRPLIter',[],'MaxSQPIter',[],'MaxTime',[],'MeritFunction',[],'MinAbsMax',[],... 'NodeDisplayInterval',[],'NodeSearchStrategy',[],'NonlEqnAlgorithm',[],'NoStopIfFlatInfeas',[],'PhaseOneTotalScaling',[],... 'Preconditioner',[],'PrecondBandWidth',0,'RelLineSrchBnd',[],'RelLineSrchBndDuration',[],'Simplex',[],... 'TolCon',[],'TolPCG',1E1,'TolRPLPFun',[],'TolXInteger',[],'TypicalX','ones(numberofvariables,1)');

```

```

[P,resnorm,residual,exitflag,output,lambda,jacobian]=lsqcurvefit(@EXCO4,PG,tf,xf,lb,ub,options);

```

figure

```

subplot(2,1,1)
plot(1E6*tf,EXCO4(P,tf))
box off
set(gca,'FontName','Times New Roman','FontSize',12,'Layer','top');
hold on
plot(1E6*tf,xf,'r')
box off
legend('Fit','Measured');

```

```

subplot(2,1,2)
plot(1E6*tf,residual)
box off
set(gca,'FontName','Times New Roman','FontSize',12,'Layer','top');

```

```

A=[1E-3*PG(1:5:end).' 1E-3*P(1:5:end).' 1E-3*PG(2:5:end).' 1E-3*P(2:5:end).' 1E-3*PG(3:5:end).' 1E-3*P(3:5:end)'];

```

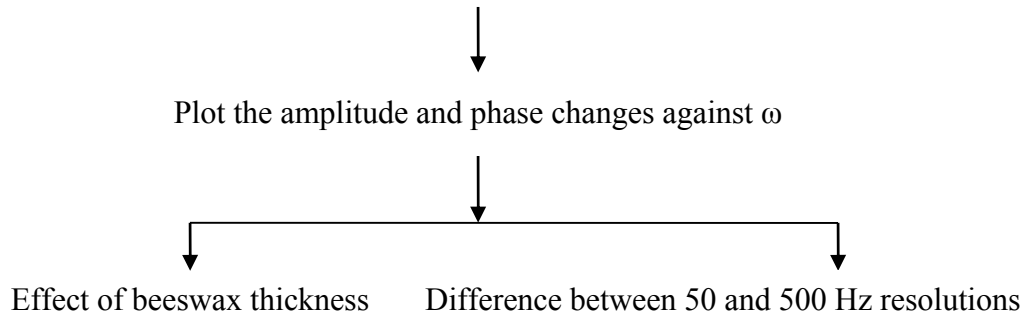
APPENDIX H

Flow chart diagram illustrating the inverse procedure.

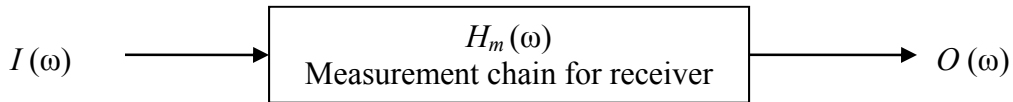
[A] Pre-processing

Measure directly the amplitude and phase changes over frequency, ω , of the output transducer's chain from experimental data, $H_m(\omega)$.

[B] Post-process data from [A].



[C] Find the output response, $O(\omega)$, from a known input, $I(\omega)$, and the frequency response determined in step A above, $H_m(\omega)$, of output measurement chain alone (i.e. the receiving transducer, amplifier and beeswax coupling). Then take the inverse Fourier transform, $F^{-1}\{O(\omega)\}$, to calculate the corresponding temporal response, $o(t)$. These steps are summarized below by assuming linearity.



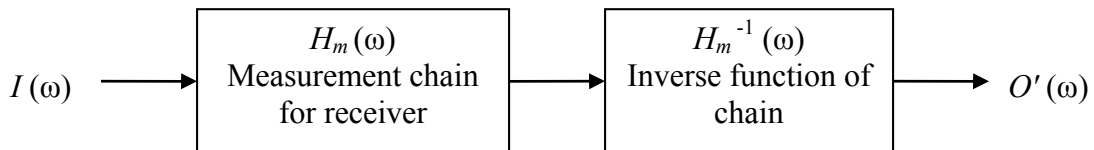
Mathematical operations:

Given $I(\omega) H_m(\omega) = O(\omega)$

Find

$$F^{-1}\{O(\omega)\} = o(t).$$

[D] Compute and verify the accuracy of the inverse function $H_m^{-1}(\omega)$.



Mathematical operations:

Given $I(\omega) H_m(\omega) H_m^{-1}(\omega) = O'(\omega)$

find

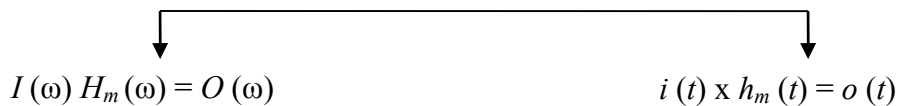
$$F^{-1}\{I(\omega)\} = F^{-1}\{O'(\omega)\}$$

or if

$$o(t) = o'(t)$$

The root mean square difference between $o(t)$ and $o'(t)$ should not exceed 0.02% over the complete time history.

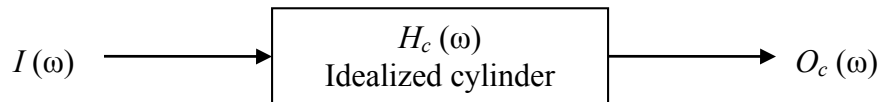
[E] Compare generic response time histories computed directly in time and indirectly from the corresponding frequency information.



where x denotes the convolution operator.

The root mean square difference between $F^{-1}\{O(\omega)\}$ and $o(t)$ should not exceed 2.26% over the complete time history.

[F] Predict temporal response of idealized cylinder, $o_c(t)$, from known input and idealized cylinder's frequency response function, $I(\omega)$ and $H_c(\omega)$, respectively.



Mathematical operations

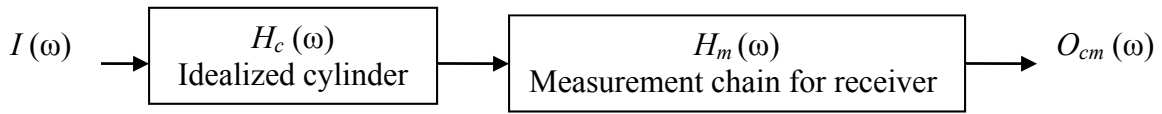
Given $I(\omega) H_c(\omega) = O_c(\omega)$

find

$$F^{-1}\{O_c(\omega)\} = o_c(t).$$

Extract COF_c, the idealized cylinder's cut-off frequencies for the F (10, 1), F (11, 1) and F (12, 1) modes.

G Include the practical effect of measurement chain, $H_m(\omega)$, on idealized cylinder's frequency response function, $H_c(\omega)$, to simulate the measured frequency response, $O_{cm}(\omega)$.



Mathematical operations:

Given
$$I(\omega) H_c(\omega) H_m(\omega) = O_{cm}(\omega)$$

find

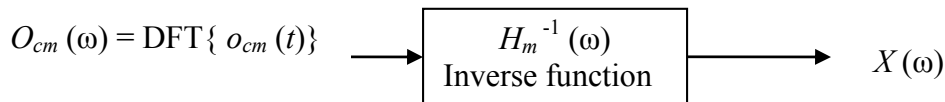
$$F^{-1}\{O_{cm}(\omega)\} = o_{cm}(t)$$

Extract COF_{cm}, the idealized cylinder's cut-off frequencies for the F (10, 1), F (11, 1) and F (12, 1) modes that incorporate modifications by the experimental measurement chain, $H_m(\omega)$.

[H] Determine the effect of thickness of beeswax coupling on time histories.



[I] Inverse procedure to remove the effect of output measurement chain, $H_m(\omega)$, from measured cylinder's time response, $o_{cm}(t)$.



Mathematical operations:

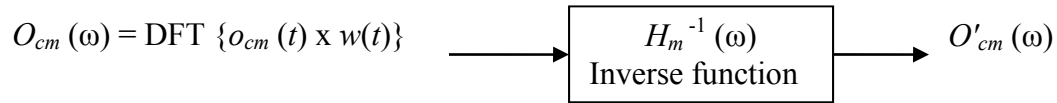
Given
$$\text{DFT}\{o_{cm}(t)\} H_m^{-1}(\omega) = X(\omega)$$

find

$$F^{-1}\{X(\omega)\} = x(t).$$

If $x(t) \neq o_c(t)$, investigate the possible causes of the difference, for example data leakage or an insufficient frequency resolution.

[J] Update idealized cylinder's response to incorporate the effect of measurement chain, $o_{cm}(t)$, by including an exponential window, $w(t)$, to eliminate data leakage.



Mathematical operations:

$$\text{Given } \text{DFT} \{o_{cm}(t) \times w(t)\} H_m^{-1}(\omega) = O'_{cm}(\omega)$$

find

$$F^{-1}\{O'_{cm}(\omega)\} = o'_{cm}(t).$$

where $w(t)$ is an exponential window function.

[K] Confirm agreement between the responses of idealized cylinder and that found by incorporating and eliminating the effect of measurement chain

Find the autocorrelation of the cylinder's predicted response, $o_c(t)$, without incorporating the effect of the measurement chain. Compare this autocorrelation with the cross correlation of the predicted response without measurement chain and the predicted response incorporating the effect of measurement chain and subsequently removing the chain.

[L] Comparison of cut-off frequencies.

Compare COF_c , the idealized cylinder's cut-off frequencies for the F (10, 1), F (11, 1) and F (12, 1) modes, with the refined COF_{cm} , the cylinder's cut-off frequencies of the same modes and those obtained experimentally when the effect of the experimental measurement chain, $H_m(\omega)$, is eliminated.